REACTION OF HYDROGEN WITH CRYSTALLINE AND AMORPHOUS ALLOYS — CRYSTAL TO AMORPHOUS TRANSFORMATION INDUCED BY HYDROGEN

Thesis by
Xian-Li Yeh

In Partial Fulfillment of the Requirements
for the degree of
Doctor of Philosophy

California Institute of Technology
Pasadena, California

1987

Submitted September 18, 1986

To my parents and my wife

ACKNOWLEGEMENT

I would like to express my greatest appreciation to Professor William L. Johnson for providing me the opportunity to study in his group. Bill's intelligence, imagination and creativity in science always amazed me and gave me invaluable help throughout my graduate study. His constant inspiration encouraged me to overcome the difficulties and to fufill this work. I thank Bill for all of this.

I received numerous help from Drs. Art Wiiliams and Konrad Samwer in the early days of my study in the group. I have learned a great deal from both of them. I would like to thank Drs. Eric Cotts, Mike Tenhover, Lowell Hazelton and Ricardo Schwarz for various valuable comments and advice. I would also like to thank Dr. Sten Samson for his help in realigning the X-ray diffractometor. Friendship and support from my fellow graduate students made my stay at Caltech very pleasant. Special thanks go to Phil Askenazy for critically proof-reading this manuscript. I must thank Concetto Geremia not only for his valuable technical assistance, but also for his help beyond his duty.

The hydrogen depth profiling experiments were performed by Drs. J.Y. Tang, C.R. Shi and Z.Y. Zhou in Prof. T.A. Tombrello's laboratory, and the back scattering experiments were performed by Y.T. Cheng in Prof. M.-A. Nicolet's laboratory. Their collaborations are deeply appreciated.

I am grateful to my uncle and aunt Dr. and Mrs. D.S. Li. for their financial support for my undergrduate study in the United States. Finally, I want to thank my parents and my wife Dorothy–their emotional support and encouragement provided

me with much strength in finishing this work. I dedicate this thesis to them.

ABSTRACT

Metastable polycrystalline $A_{1-x}B_x$ (A=Zr, Hf, B=Pd, Rh, $0.15 \leq x \leq 0.25$) alloys having a fcc structure are reacted with hydrogen gas at temperatures ranging from 25°C to 250°C. It is demonstrated for the first time that an amorphous phase can be formed during such a solid state reaction when the temperature lies below 220°C. Such a reaction is possible only if the following requirements are satisfied: The existence of a thermodynamic driving force (i.e., the amorphous phase must have a lower free energy than the free hydrogen and the crystalline phase from which it forms) and the existence of a kinetic constraint (i.e., the formation of thermodynamically preferred equilibrium phases or phase mixtures must be kinetically suppressed).

X-ray diffraction and TEM studies show that the amorphous phase grows at the expense of the crystalline phase during hydrogen absorption by these metastable fcc alloys. The formation of the amorphous hydride phase is observed by TEM to begin at grain boundaries of the polycrystalline alloys much in the same manner that "melting" nucleates at grain boundaries. X-ray analysis indicates that the Zr-Zr distance increases as hydrogen is absorbed, suggesting that hydrogen atoms prefer to stay in tetrahedral sites surrounded by four Zr atoms. This provides evidence as to why the amorphous hydride phase is more stable than the fcc hydride phase. The thermal behavior of amorphous hydrides obtained by hydriding metallic glasses and that obtained by hydriding metastable crystalline alloys are compared and found to be similar. The hydrogen distribution and surface effects are investigated using hydrogen depth profiling, SEM and Rutherford backscattering. Hydrogen permeation through the sample surface has been found to be the rate limiting step in the hydriding reaction.

Based on the present experiments and an analysis of the relevant free energy curves, we discuss the thermodynamic and kinetic aspects of this phase transformation to explain why an amorphous phase is formed. The mechanism for this can be viewed as melting in the solid state. A simple "chemical frustration" model is proposed to explain the kinetics of amorphization via hydriding.

TABLE OF CONTENTS

LIST OF FIGURES

Fig.4.5 The phase diagram of Zr–Rh system. (From W.G. Mofatt, *Handbook of Binary Phase Diagrams*, General Electric, 1978). The T_o curve (the solid curve) is calculated based on the regular solution approximation.

Fig.4.6 X-ray diffraction patterns of $Zr_{0.82}Pd_{0.18}$ before (a) and after (b) hydrogen absorption. The original sample has a single phase fcc structure.

Fig.4.7 X-ray diffraction patterns of $Hf_{0.75}Rh_{0.25}$ before (a) and after (b) hydrogen absorption.

Fig.4.8 The X-ray diffraction patterns for $(Zr_{0.80}Rh_{0.20})H_y$ at various hydriding times. The top pattern is the X-ray diffraction pattern of $(Zr_{0.80}Rh_{0.20})H_{1.0}$.

Fig.4.9 Lattice parameters of polycrystalline fcc $Zr_{0.80}Rh_{0.20}$ versus the fraction of amorphization transformation.

Fig.4.10 Hydrogen to metal ratio (filled circles) and fraction of amorphization (open circles) in $Zr_{0.80}Rh_{0.20}$ plotted as a function of hydriding reaction time.

Fig.4.11 TEM micrograph and selected area electron diffraction patterns of partially amorphized $(Zr_{0.80}Rh_{0.20})H_{0.5}$.

Fig.4.12 Dark field image of partially amorphized $(Zr_{0.85}Rh_{0.15})H_{0.8}$.

Fig.4.13 TEM micrograph and SAED pattern of fully amorphized $(Zr_{0.80}Rh_{0.20})H_{1.0}$.

Fig.4.14 The reduced radial distribution functions $G(r) = 4\pi r(\rho(r) - \rho_o)$ for as-quenched amorphous $Zr_{0.75}Rh_{0.25}$, hydrided originally amorphous $(Zr_{0.75}Rh_{0.25})H_{1.38}$ and hydrided originally crystalline $(Zr_{0.75}Rh_{0.25})H_{1.38}$.

Fig.4.15 X-ray diffraction patterns of (a) as-quenched glassy $Zr_{0.75}Rh_{0.25}$ and (b) dehydrided $Zr_{0.75}Rh_{0.25}$. The arrows indicate the fcc-ZrH_2 phase.

solution. τ_H and τ_{Zr-Rh} represent diffusion fluxes. B is the boundary with the hydrogen gas.

LIST OF TABLES

PRELUDE

It was December 24, 1981. I still remember that frustrating day when Prof. Johnson and I were trying to rapidly quench $Zr_{0.75}Rh_{0.25}$ in order to obtain the amorphous phase for the study of hydrogen absorption in the glassy alloy. We went home disappointed with the result that all of the as-quenched foils contained a substantial amount of crystalline materials. Having nothing else to do during the lonely winter break, I decided to hydride these crystalline samples to see what phase they would transform to upon hydriding. To my surprise, I discovered that the crystalline phase disappeared after hydriding. This experiment turned out to be the first demonstration of amorphous phase formation in the solid state. It opened the new field of synthesizing bulk amorphous alloys by solid state reaction.

Subsequently, Ricardo Schwarz, Konrad Samwer, Michael Atzmon and Prof. Johnson established that amorphization during solid state reaction also occurs during the interdiffusion of binary metal layers or elemental composites.

As a graduate student of Prof. Johnson, I continued to pursue this project of amorphization by hydriding, and wrote this thesis as a record of this discovery.

I. INTRODUCTION

The discovery of metallic glasses by Professor Pol Duwez and his students at Caltech in 1959 was one of the most exciting events in the annals of materials science and engineering [1.1]. This discovery was fascinating because it not only generated new ground for scientists to explore, but also provided a class of exotic new materials with promising engineering applications. Metallic glass, which is often used as a synonym for amorphous alloys (but refers specifically to materials obtained by the rapid quenching of metallic melts) may be regarded as a solid with a configurationally frozen-in liquid structure. Metallic glasses are macroscopically isotropic in the size domain $\geq 20Å$, as are silicate glasses. Because the constituent atoms are bound together by long-range metallic bonding, metallic glasses are malleable and are good electrical conductors as opposed to silicate glasses which are good insulators and are covalently bonded. Metallic glasses are strong and ductile, propagate acoustic waves with small losses, have lower electrical and thermal conductivities compared to pure metals, and often have remarkably good corrosion resistance [1.2].

Metallic glasses are traditionally formed by rapid cooling of liquid metals [1.3] or deposition of metallic vapors [1.4] at rates sufficient to bypass crystallization. For the formation of a metallic glass, cooling rates in the range of $10^4 - 10^{12}$ K/sec are required to suppress nucleation and growth of more stable crystalline phases in undercooled alloy melts [1.5]. These facts lead to severe restrictions in the synthesis of glassy metals. For example, simple heat transfer considerations require at least one of the specimen dimensions to be rather small, typically 10–100 μm. For this reason, it is of considerable interest to explore alternate means of forming bulk metallic glasses.

A way to achieve this goal is to transform the crystalline phase into the amorphous phase utilizing chemical energy available in the initial sample configuration. Fig.1.1 illustrates how such a process can be accomplished. The system is originally in a crystalline phase configuration α (see Fig.1.1a). If one can destabilize the configuration α by raising its free energy above the phase configuration β (suppose this is an amorphous phase), the spontaneous transformation from α to β can be expected (see Fig.1.1b). Although the phase configuration γ is more stable, the system is trapped in β because it cannot summon enough energy to overcome the activation energy barrier in order to reach γ (see Fig.1.1c).

The key issue here is under what condition a crystalline phase can be destabilized. Gibbs was the first to point out the criteria for the instability of a single phase system [1.6]. According to these criteria, a spinodal decomposition must occur if one of the following criteria is violated:

$$\frac{\partial^2 G}{\partial P^2}|_{T,C_i} = G_{PP} < 0$$

$$\frac{\partial^2 G}{\partial T^2}|_{P,C_j} = G_{TT} < 0$$

$$\frac{\partial^2 G}{\partial C_i^2}|_{P,T} = G_{C_i,C_i} > 0$$

$$G_{TT}G_{PP} - G_{TP}^2 > 0$$

Gibbs criteria can be extended to determine the sign of shear or bulk modulus. That is to say that the vanishing of these physical observables characterizes the mechanical collapse of a solid. Such a vanishing of the shear or bulk modulus would occur as temperature increases.

Recently, attempts have been made to simulate the instability of a crystal. Thorpe [1.7, 1.8] studied an fcc lattice with all atoms connected by springs with

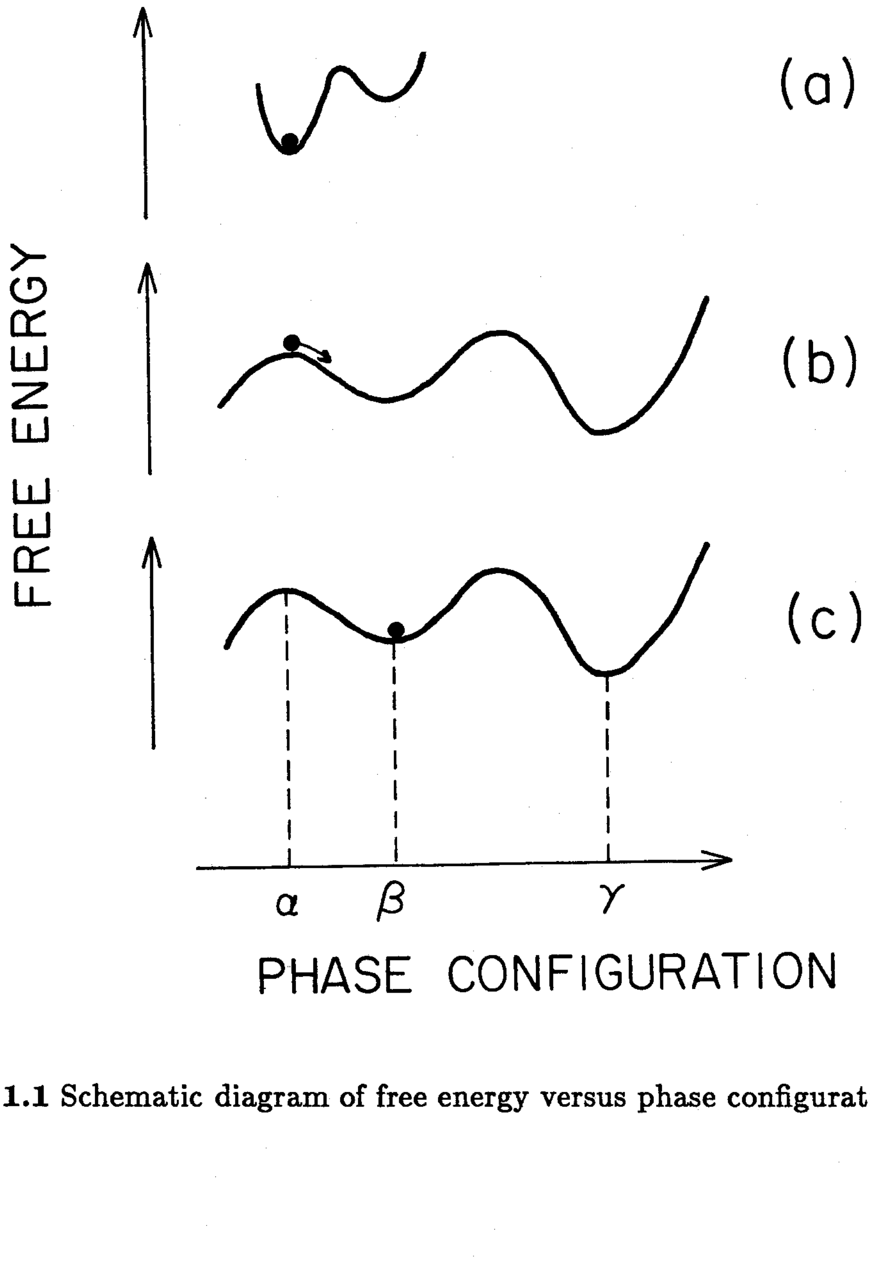

Fig.1.1 Schematic diagram of free energy versus phase configuration. (See text.)

force constant K. As springs are randomly removed, the shear and bulk moduli decrease and vanish at some critical fraction of removed springs. Egami [1.9], on the other hand, studied the strain induced crystal instability. He found that in a binary solid solution containing atoms of two different sizes, a topological instability occurs when the fraction of solute atoms (the smaller atoms) reaches certain critical value. All these works suggested that crystal instability can be induced by various types of disorder, such as defects, chemical disorder etc. (An excellent review on this subject is given by reference 1.10).

The first experiment to destroy the crystalline order and form the amorphous phase from a crystalline solid was done by Block in 1962 [1.11] who reported that U_6Fe was amorphized upon irradiation by large dose fission fragments. Following this experiment, amorphization induced by irradiation has been reported on several intermetallic compounds. It is now understood that irradiation destroys the long range order and chemical order of the crystal [1.12] which may account for the amorphization of a crystal. The composition-induced solid state amorphization had not been studied until very recently. The first example of such kind of reaction was the amorphization of the metastable polycrystalline $Zr_{0.75}Rh_{0.25}$ alloy upon hydrogen absorption reported by this author, Samwer and Johnson in 1983 [1.13]. Subsequently, Schwarz and Johnson found that diffusion couples of two transition elements could react through solid state interdiffusion to form metallic glass [1.14]. More recently, it was found that the amorphous alloys could also be synthesized by high energy ball-milling of crystalline powder mixtures [1.15] or cold-rolling of elemental composites [1.16]. All of these reactions are of a similar nature in that the excess chemical energy of the initial material configuration provides the driving force for the formation of the glassy phase. The reactions proceed under the kinectic condition that the formation of intermetallic compounds is suppressed.

It is noteworthy to point out that the grain boundaries and defect sites have been observed to be preferred heterogeneous sites for nucleation of the glassy phase both in the irradiation- and composition-induced solid state amorphization. This feature is similar to the morphology of the melting process. These heterogeneous sites prevent the superheating of the crystalline phase and trigger the amorphization reaction.

The present work has focussed on the study of the mechanisms of the crystal to amorphous transformation in fcc $Zr_{1-x}Rh_x$, $Zr_{1-x}Pd_x$ and $Hf_{1-x}Rh_x$ ($0.15 \leq x \leq 0.25$) polycrystalline alloys during hydriding—a special example of the solid state amorphization reaction. The thermodynamics and kinetics of amorphization induced by hydrogen absorption are studied via various experimental techniques. Among the experimental techniques used in this study are X-ray diffraction, electron microscopy, differential scanning calorimetry (DSC), Rutherford backscattering and nuclear reaction hydrogen depth profiling.

This thesis is organized as follows. In chapter 2, basic ideas and concepts regarding the formation and the structure of amorphous metallic alloys will be reviewed. This chapter will also provide the reader with some background on the subject of hydrogen in crystalline and amorphous metals. The sample preparation and experimental methods used in this study will be described in chapter 3. Chapter 4 contains the experimental results and some interpretation of the results. This chapter is separated into three parts. The first part includes the study of the structure and morphology of alloys utilizing X-ray diffraction, transmission electron microscopy and energy dispersive spectroscopy. Various properties and characteristics of amorphous hydrides produced both by hydriding polycrystalline alloys and by hydriding metallic glasses, such as superconducting transition temperature, atomic radial distribution function and mass density, will be compared. The second part concerns thermal analysis and contains results of a study on thermal stability and crystallization behavior of metallic alloys at various hydrogen concentrations. The thermal behavior of amorphous hydrides prepared by two distinct methods will be compared. The third part incorporates the results of surface analysis and hydrogen depth profile studies. The kinetics of hydriding under different surface conditions will be analyzed. The details of the thermodynamics and kinetics of solid state amorphization via hydriding will be discussed in chapter 5. A simple "chemical frustration" model will be proposed to explain why the formation of the amorphous phase upon hydriding is kinetically favored.

II. BACKGROUND AND RELATED SUBJECTS

§2.1 AMORPHOUS METALS

2.1.1 Kinetics of Solidification and Glass Formation

A glass can be formed by the continuous undercooling of a liquid until it is configurationally frozen. The glass is distinguished from a crystalline solid formed by discontinuous solidification in which solid crystalline phases appear and grow in the liquid, the solidification process occuring only at the liquid-solid interface [2.1].

To illustrate thermodynamic aspects of the liquid-solid transformation, the temperature dependence of Gibbs free energies of the various states (liquid, crystal and glass) of a glass-forming material at constant pressure is shown in Fig. 2.1. As a liquid is cooled, its free energy rises above the free energy of the crystalline phase below the freezing temperature, T_f (this temperature is also called the melting temperature T_m). Below T_f, there is a thermodynamic driving force for the crystallization reaction . Crystallization generally begins by the formation of nuclei, and followed by the growth of these nuclei at the expense of adjacent liquid. Thus, the freezing process is confined to the liquid-crystal interface. The crystallization reaction is impeded by the free energy barrier to the formation of nuclei. This can be explained by classical nucleation theory [2.2]. According to this theory, the variation of Gibbs free energy due to the formation of a spherical shape embryo is expressed as:

$$\Delta G = -\frac{4}{3}\pi r^3 \frac{L\Delta T}{T_m} + 4\pi r^2 \gamma_{sl}$$

where r is the radius of the embryo, L is the free energy per unit volume, γ_{sl} is

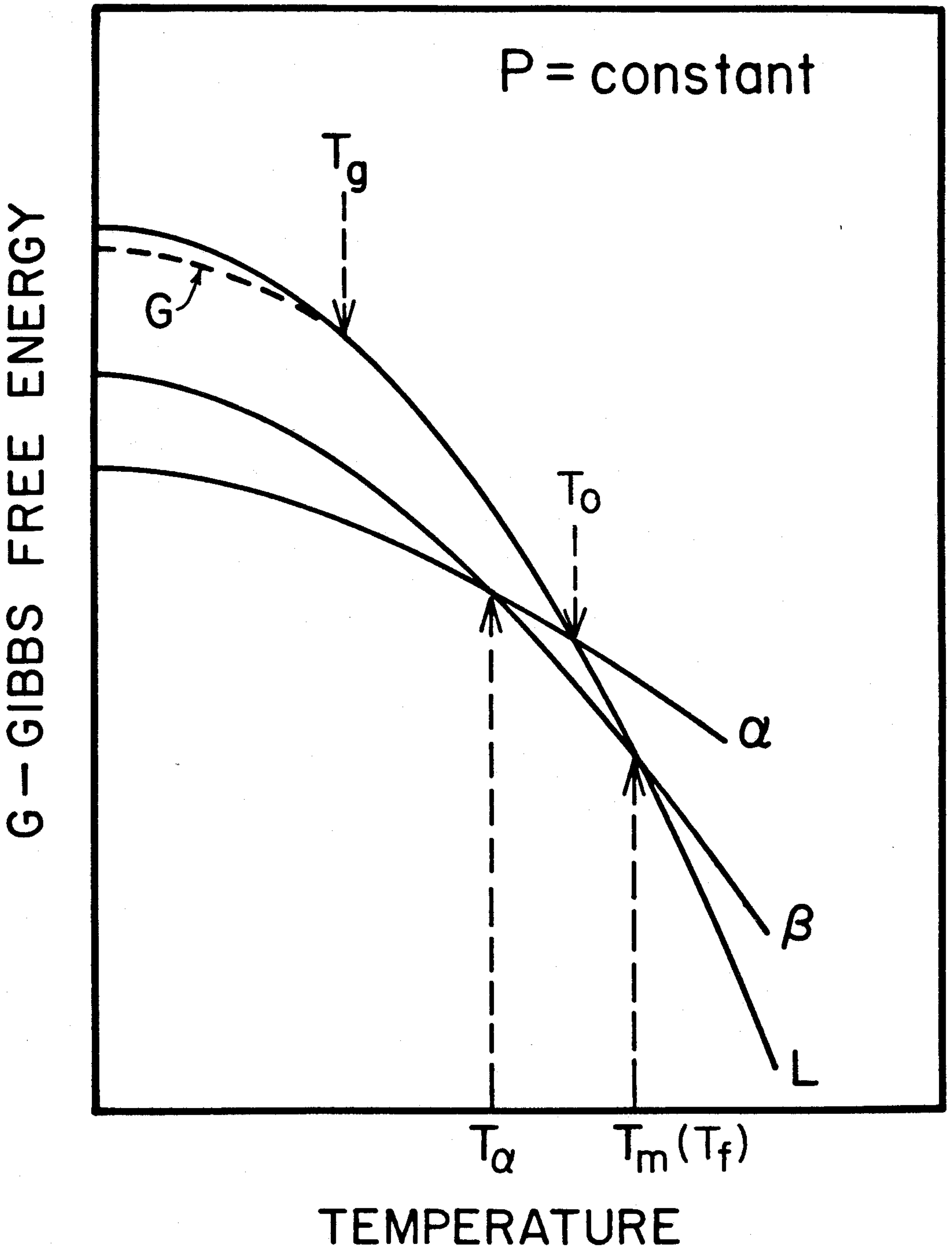

Fig.2.1 Gibbs free energies of liquid (L), crystalline ($\alpha\&\beta$) and glassy (G) phases plotted as a function of temperature at constant pressure. (Taken from ref. 2.4).

the crystal-liquid interfacial free energy, and $\Delta T = T_m - T$ is the undercooling temperature. The nucleation is driven by the decrease in the bulk contribution to the free energy with increasing nucleus (or embryo) size, while the nucleation barrier is the result of the positive contribution of the crystal-liquid interfacial free energy γ_{sl} to the total free energy variation. The balancing of these two contributions, one increasing with the surface area of the embryo and other decreasing with the embryo volume, leads to the condition that only those embryos having volumes larger than some critical volume $\frac{4}{3}\pi(r^*)^3$ can become stable nuclei for crystal growth. The critical radius r^* is defined at the condition $\partial G/\partial r = 0$:

$$r^* = 2\gamma_{sl}\frac{T_m}{L\Delta T}$$

Nuclei with larger r value gain energy by growth. Note also that r^* decreases as the undercooling increases. The larger the undercooling, the greater the driving force for crystallization. In practice as the liquid is cooled below T_m (see Fig. 2.1), it remains as a metastable undercooled liquid for extended time for undercoolings up to some critical value ΔT.

Below the freezing temperature, the viscosity of undercooled liquids η_v is fairly well described by the Fulcher equation:

$$\eta_v = A\exp[a/(T - T_g)]$$

where T_g is known as an ideal glass transition temperature and A and a are constants which depend on the material. One notes that the viscosity increases very rapidly over the temperature range from the freezing temperature to T_g. Below T_g, the diffusive motion of atoms becomes so sluggish that the atoms are confined to vibrate locally about equilibrium positions over a rather long time scale (say, more than

1000 years). At such temperatures,the material can be considered to be solid. It is called a glass.

Turnbull pointed out that the formation of the first nucleus requires a time scale τ_{min}, for all molecules constituting the nucleus to jump from the liquid to the nucleus [2.1]. This time scale is inversely proportional to the undercooling which drives the crystallization, but it is proportional to the viscosity which is actually a measurement of the time scale of atomic rearrangement. The crystallization will thus be bypassed, if the time scale of cooling from T_m to T_g is much less than τ_{min}; when this occurs, the liquid is configurationally frozen and a glass is formed in spite of the fact that it has higher free energy than the crystalline state, as shown in Fig. 2.1.

The kinetics of glass formation described above can further be summarized by using an isothermal temperature–time–transformation (TTT) diagram (Fig. 2.2), which gives the relation between the temperature (plotted linearly) and the time (plotted logarithmically) for a fixed fraction of the sample to crystallize (say, 1% of crystallization to be attained) [2.3]. The nose shape curve indicates that it takes longer time for crystallization to begin (and to reach completion) at both high and low temperatures than at intermediate temperatures. The location of the nose (peak nucleation rate) depends on the rate of the atomic rearrangement as well as the nucleation barrier. In specific cases, the onset of the crystallization of a phase which does not require long range atomic diffusion (e.g., the formation of the fcc $Zr_{0.80}Rh_{0.20}$ phase) should appear to the left of the onset of crystallization of phases (e.g., the formation of a phase mixture $Zr+Zr_2Rh$) requiring some form of chemical segregation and thus atomic diffusion over substantial distances. The

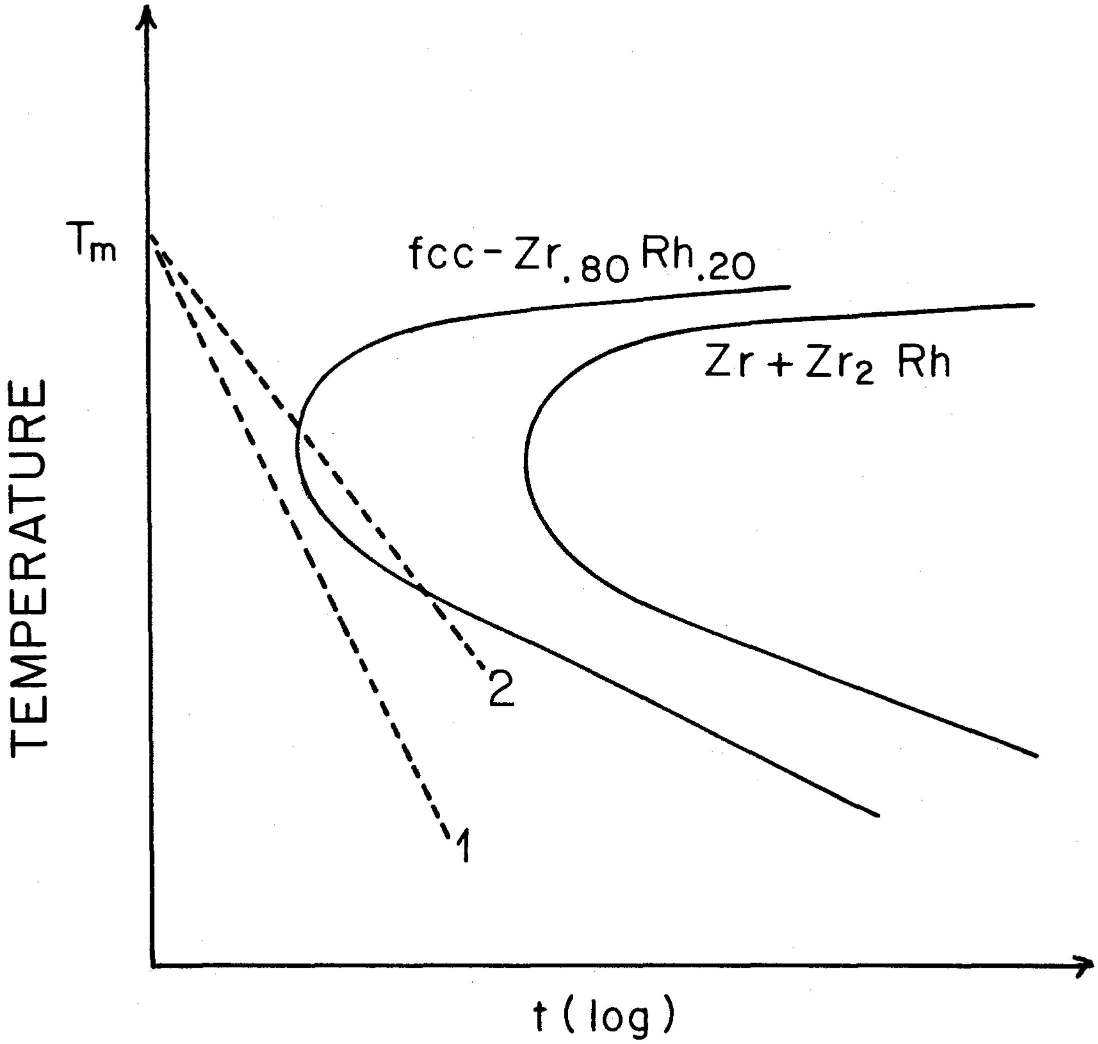

Fig.2.2 Isothermal temperature-time-transformation diagram of (a) the formation of the metastable fcc $Zr_{0.80}Rh_{0.20}$ and (b) the two phase mixture of $Zr+Zr_2Rh$ from the melt of $Zr_{0.80}Rh_{0.20}$. At the cooling rate 2, the nucleation and growth of $Zr+Zr_2Rh$ is bypassed while the polymorphic transformation to the fcc phase is possible. At a higher cooling rate (as indicated by dashed line 1), both the crystallization noses are avoided and only the glassy phase can form.

prime requirement for glass formation is to quench the melt sufficiently fast that all of the crystallization noses in the TTT curve are avoided as indicated by the dotted line "1".

Turnbull's theory explains why an undercooling is required for crystallization. However, the reverse is not true: the superheating of a crystal has been found to be extremely difficult. The primary reason for this is that the crystal surface, defects, and grain boundaries compose potent heterogeneous nucleation sites such that near the melting temperature the nucleation time scale for the formation of liquid phase from the crystalline phase is quite short [2.4]. (Recently, it has been demonstrated by Dages et al [2.5] that by reducing these heterogeneous nucleation sites, one can superheat Ag by as much as 10 K for several minutes). Based on the argument mentioned above, one can conceive the following experiment which can actually transform a crystalline phase into an amorphous phase in the solid state. Suppose the β phase in Fig 2.1 has a complex structure, or it can even be a phase mixture such that the nucleation time scale to form β phase is very large. As one heats the α phase above T_α, although the β phase becomes a thermodynamically stable phase, its formation is kinetically suppressed. Thus, the α phase remains metastable until the temperature (T_o) at which its free energy becomes higher than the liquid phase. Suppose, further, that the glass transition temperature (not shown in Fig.2.1) is higher than T_o; then the α phase can possibly transform into the amorphous phase above T_o. In terms of statistical physics, such a phenomenon occurs because the system does not have the opportunity to probe all the states available in the phase space and to find the minimum energy state, Alternatively, the system probes the nearby surroundings of the point in the phase space and settles down in the local minimum energy state. Although this solid state melting upon increasing temperature has never been observed, we will, however, demonstrate in following chapters that by varying the composition of crystalline alloy (e.g., let an alloy absorb hydrogen), not the temperature, the free energy of a crystal can rise above the amorphous phase, inducing a crystal to amorphous transformation.

2.1.2 Structure of Amorphous Metallic Alloys

The atomic-scale structure of amorphous metallic alloys has been studied intensively using X-ray, electron and neutron diffraction techniques. Although in the following we will be concerned with X-ray diffraction only, most of the results may be applied to electron and neutron diffraction as well.

In an X-ray diffraction pattern of crystalline solids, one observes a set of narrow Bragg peaks, representing a set of well-defined lattice spacings. Lacking long range periodic structure, the atomic positions of amorphous alloys can not be precisely described as in the case of a crystal where one obtains constructive interference from the periodically spaced lattice planes. Only a series of several broad bands can be observed in an X-ray diffraction pattern of amorphous alloys. It is therefore impossible to obtain an exact three dimensional description of the atomic positions for amorphous alloys using a diffraction analysis (as one does for crystalline alloys). The reduced radial distribution function $G(r) = 4\pi r(\rho(r) - \rho_o)$ has been widely used to describe the atomic structure of amorphous metallic alloys. In this expression, $\rho(r)$ is the atomic density at a distance r from a given atom and ρ_o is the mean density. At distances greater than five atomic shells, the atomic pair positions are no longer correlated and the density $\rho(r)$ approaches the mean density ρ_o. Thus, the function G(r) approaches zero. G(r) can be obtained from the Fourier transform of the interference function measured in X-ray diffraction. It is given by the following expression:

$$G(r) = \frac{2}{\pi}\int_0^\infty K(I(K)-1)\sin(Kr)\,dK$$

and the interference function I(K) is given by:

$$I(K) = 1 + \int_0^\infty 4\pi r^2(\rho(r)-\rho_o)\frac{\sin(Kr)}{Kr}\,dr$$

where $K = \frac{4\pi}{\lambda}\sin\theta$ is the absolute value of the scattering vector (for details see ref. 2.6, 2.7). The first nearest neighbor coordination number of a given atom is given by:

$$\eta = \int_0^{r_o} 4\pi r^2\rho(r)\,dr$$

where r_o is the minimum following the primary maximum of $\rho(r)$. Thus, X-ray diffraction studies provide one with information about short range atomic correlation of amorphous alloys.

However, radial distribution functions for amorphous alloys only gives a one-dimensional projection of a complicated three-dimensional arrangement of atoms. An entirely satisfactory description of atomic structure cannot be deduced from diffraction experiments alone, since amorphous alloys have aperiodic, isotropic structures. Structural modeling is an alternative means for the analysis of amorphous structure.

Basically, there have been two competing ways to model the structure of metallic glasses. The earliest attempt describes the metallic glasses as the limiting case of a crystalline solid in which the crystallites are very small and oriented at random. In this so-called microcrystalline model, the absence of long range order is regarded as the result of the small size of the crystallites, their random orientation, strain introduced by mismatch of sublattices at grain boundaries, the presence of a disordered interfacial region and defects such as dislocations, disclination, or stacking faults within the microcrystallites [2.7]. The reconstruction of the X-ray pattern from this model does show broadened bands, similar to that obtained from metallic glasses. However, the radial distribution function constructed from this model does not give overall satisfactory agreements with experimental data.

The second model for metallic glasses is known as dense random packing of hard spheres (DRPHS), was originally proposed by Bernal [2.8] to describe the structure of liquid metals. Turnbull and Cohen [2.9] later suggested the use of the DRPHS model for metallic glasses. In his original work, Bernal packed steel balls with equal diameter in a rubber bladder and kneaded it to obtain maximum density. He then poured in molten wax so that the steel balls could be removed. The coordinates of the steel balls were subsequently measured and analysed. Bernal showed that a large number of possible structures, with nearly the same nearest neighbor distribution could be formed. These structures could be characterized by the nature of interstitial sites. Bernal found that these sites include the five polyhedra which are shown in Fig.2.3. The number of these polyhedra per 100 hard spheres in a DRPHS was determined by Cargill [2.7]. The results are listed in Table 2.1. These polyhedra are important in our study of hydrogen in amorphous metals where hydrogen is found to be situated in sites of similar character.

§2.2 HYDROGEN IN METALS

2.2.1 Heats of Formation for Transition Metal Hydrides

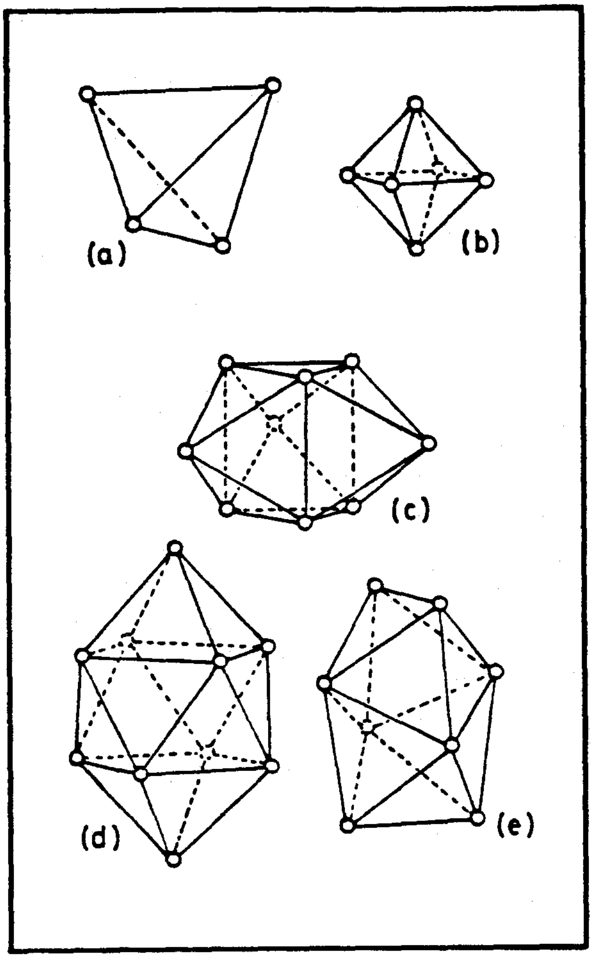

Fig.2.3 The Bernal polyhedra found in a DRPHS model: (a) tetrahedron, (b) octahedron, (c) trigonal prism capped with three half- octahedra, (d) Archimedian antiprism capped with three half-octahedra and (e) tetragonal dodecahedron. (Taken from ref. 2.7).

Type of polyhedron	Minimum distance from central position to vertex in unit of sphere diameter	Occurrence per 100 spheres
(a) Archimedian antiprism	0.82	1.6
(b) Trigonal prism	0.76	12.8
(c) Tetragonal dodecahedron	0.62	12.4
(d) Tetrahedron	0.61	292.0
(e) Octahedra (often present as half octahedra)	0.71	4.0

Table 2.1 Sizes of idealized Bernal holes and the number of each type expected per 100 dense random packed hard spheres. (Taken from ref. 2.7.)

Metal-hydrogen compounds and solutions have a variety of bonding mechanisms, ranging from ionic hydrides, say KH, covalent molecular hydrides, like AlH_3, to transition metal hydrides which are metallic in character and can be formed by the direct absorption of hydrogen into the transition metal lattice. We restrict ourselves here mainly to a discussion of transition metal hydrides, since this is most relevant to the present topic.

In principle, any transition metal should be able to form a metallic hydride. However, many of the possible hydride phases are not generally found because they would be stable only under extremely high pressures of hydrogen. It is well known that the transition metals of groups III, IV and V and palladium react with hydrogen exothermically and form rather stable hydrides while transition metals of groups VI, VII and VIII (except Pd) and noble metals react with hydrogen endothermically, and only form hydrides at very high pressures [2.10]. Many efforts have been made to understand the propensity of hydride phase formation in various transition elements. Miedema et al. were among the first to calculate the variation in the heats of formation (thus the stabilities) of transition metal binary hydrides systematically [2.11]. In their semi-empirical cellular atomic model, Miedema et al. assumed that pure metals retain their Wigner-Seitz cells during the alloy formation (hydrides of transition metals are treated as alloys containing interstitial hydrogen atoms). The heats of formation are then estimated from the change in the boundary conditions caused by the charge transfer when the dissimilar cells are in contact. Miedema et al. were able to obtain estimates of heats of formation for many transition metal hydrides, as shown in Table 2.2. Although lacking a firm microscopic foundation, Miedema's approach gives a remarkably good prediction regarding which metals will form a stable hydride. This model was extended to describe ternary hydrides

IIIA	IVA	VA	VIA	VIIA	VIIIA	IXA	XA
ScH_2	TiH_2	VH_2	CrH	MnH	FeH	$CoH_{0.5}$	$NiH_{0.5}$
−200	−126	−54	−16	−9	+14	0	−6
YH_2	ZrH_2	NbH_2	MoH	TcH	RuH	$RhH_{0.5}$	$PdH_{0.5}$
−225	−165	−60	−12	(+36)	(+42)	(+25)	−40
LaH_2	HfH_2	$TaH_{0.5}$	WH	ReH	OsH	IrH	PtH
−210	−133	−78	(+16)	(+52)	(+48)	(+42)	(+26)
ThH_2	UH_3	PuH_2					
−146	−85	−155					

Table 2.2 The enthalpy of formation of transition metal hydrides at the composition indicated in units kJ/mol. H_2. Values in brackets are estimated from empirical model considerations; others are experimental. (Taken from ref. 2.10).

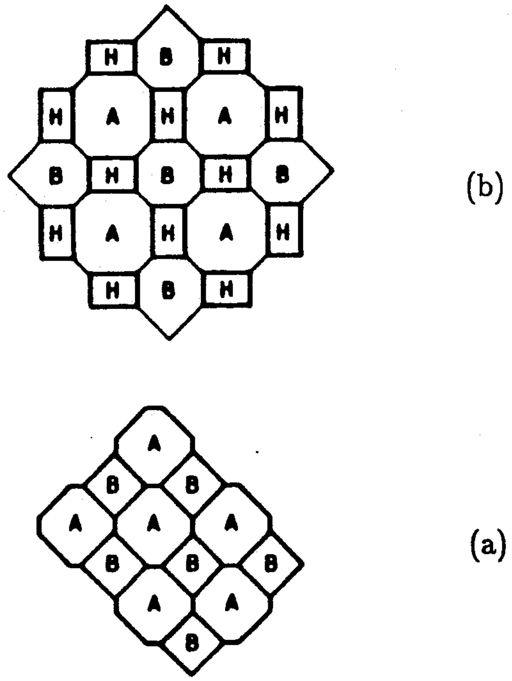

Fig.2.4 A schematic representation of the positions of hydrogen atomic cells in a hydride (b) formed from a transition metal alloy AB (a). Metal A is assumed to form a relatively stable hydride. (Taken from ref. 2.10).

formed from intermetallic Compounds AB_n $(n \geq 1)$, in which A forms a stable binary hydride and B does not. During hydride formation, the hydroden cells will tend to be surrounded by A cells as far as possible. Fig. 2.4 gives a schematic representation of the positions of hydrogen cells and shows that the contact area between metal A and H is larger than that of metal B and H. The heat of formation for ternary hydrides is expressed by the following equation:

$$\Delta H(AB_nH_{x+y}) = \Delta H(AH_x) + \Delta H(B_nH_y) - (1-F)\Delta H(AB_n)$$

where (1-F) is the fraction of AB contacts broken in the process of forming the hydride. Since A forms a more stable hydride than B does, the hydride of an AB_n compound is more stable than BH_y, but less stable than AH_x. AB_nH_x constitutes a class of interesting alloys for the hydrogen storage application, because they can reversibly absorb and desorb hydrogen near one atmosphere.

Switendick [2.12] and Gelatt et al. [2.13] followed a more microscopic line of the development. Switendick calculated the electronic structure of metal hydrides and attempted to determine which hydride phases should be formed for a particular metal based on electronic energy considerations. His result also predicted the minimum H-H distance in metals to be 2.0–2.1Å . Gelatt also derived the heat of formation for binary hydrides based on a band structure calculation. His result gave quantitative agreement with experimental data (see Fig. 2.5). Although Gelatt's method is adequate for binary hydrides, it is too difficult and thus not realistic to apply to the calculation of the heats of formation for ternary hydrides.

2.2.2 Site Occupancy and Phase Transformation

Hydrogen atoms occupy either tetrahedral sites or octahedral sites in the metal

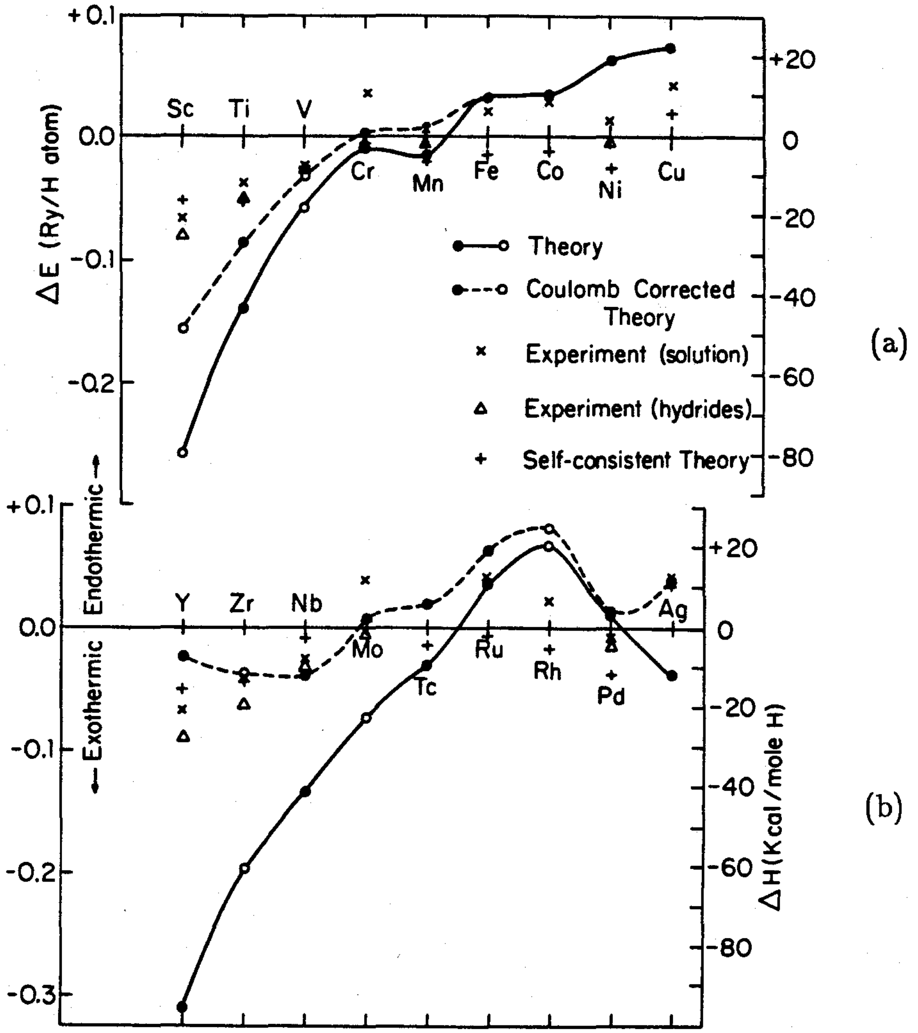

Fig.2.5 The calculated heat of formation of 3d (a) and 4d (b) transition metal hydrides with (dashed curve) and without (full curve) Coulomb energy corrections to the non-self-consistent potential. Open circles indicate the elements for which the calculated value is found by interpolating the components of ΔE between neighboring elements. The pluses are the results of fully self-consistent calculations, the crosses are experimental values of the heat of solution of hydrogen in the metals, and the triangles give the experimental heat of formation of hydride phases. (Taken from ref. 2.13).

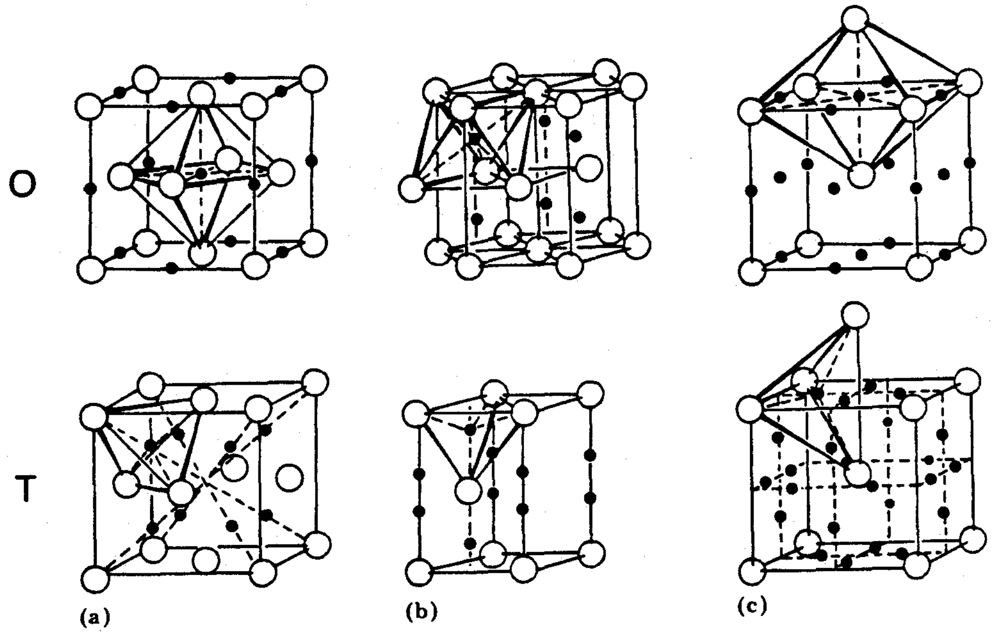

Fig.2.6 Tetrahedral and Octahedral interstitial sites in (a) fcc, (b) hcp and (c) bcc lattices. (Taken from ref. 2.17.)

lattices with fcc, bcc and hcp structures. In the fcc and hcp lattices, there are two tetrahedral sites and one octahedral site per atom; in the bcc lattice, there are either six tetrahedral sites or three octahedral sites depending on how the interstitial volume is divided (Fig. 2.6). The question arises as to what type of interstitial sites are most energetically favorable for hydrogen atoms to reside in for a particular metal lattice? Various experimental techniques, including elastic and inelastic neutron scattering [2.14, 2.15], have been employed to experimentally determine the actual type of insterstitial sites which hydrogen atoms reside in. Somenkov and Shil'stein [2.16] suggested that the octahedral sites are favored by hydrogen atoms if $0.41 \leq R_H/R_M \leq 0.73$, while the tetrahedral sites are favored if $0.22 \leq R_H/R_M \leq 0.41$, where R_H and R_M are the atomic radii of hydrogen and metal atoms respectively. According to this criterion, hydrogen atoms should occupy the tetrahedral sites in most transition metal hydrides; however, several exceptions do exist, notably Pd , Ni and several bcc metals in which octahedral sites are favored. For details of this subject, see also ref. [2.17].

There have also been efforts to determine the site occupancy and maximum concentration of hydrogen atoms in metallic glasses. Samwer and Johnson [2.18] studied the structure of Zr–Pd and Zr–Rh amorphous alloys using X-ray diffraction technique. They found that the larger Bernal polyhedra could be broken down into distorted tetrahedra, and proposed that hydrogen atoms occupied predominantly the tetrahedral sites formed by four zirconium atoms at corners (we will briefly call them 4Zr sites in later text). Williams et al. measured the inelastic neutron scattering spectra of hydrogen vibrations in Zr_2Pd hydrides, and confirmed that hydrogen atoms indeed occupied only the 4Zr tetrahedra [2.15]. Bowman et al. measured proton NMR on Ti–Cu and Zr–Pd hydrides and obtained the same result [2.19]. However, Suzuki [2.14] found that hydrogen atoms in glassy Zr–Ni hydrides preferred to occupy the 4Zr tetrahedral sites up to about 25 atomic percent hydrogen content; with further increase of hydrogen content, hydrogen atoms are gradually located at the tetrahedral sites surrounded on the average by 3Zr and 1Ni atoms. Hydrogen atoms in these sites are weakly bonded in comparison with those composed of four Zr atoms. Hydrogen atoms in the weakly bonded sites can easily escape from the material when the material is either heated or placed in a vacuum of order 10^{-6}torr, (i.e., when the external chemical potential of hydrogen is substantially reduced) [2.20].

With increasing hydrogen concentration in metals, one frequently observes a phase transformation. There are essentially two types of phase transformations induced by hydrogen. In the first type, the symmetry of the crystal lattice is preserved and the effect of the hydrogen is merely to produce a discontinuous lattice expansion. In some cases, the hydrogen absorption is accompanied by a slight distortion of the metal lattice which lowers the symmetry. The above mentioned type of transformation is best viewed as analogous to a "lattice gas" behavior, and the corresponding pressure-concentration isotherms can be described by the Van de Waals equation. As shown in Fig. 2.7, a high concentration hydride phase can coexist with the low concentration phase below a certain critical temperature (298°C in this case) and in a certain hydrogen concentration range [2.21]. The effective interaction between hydrogen atoms in such hydrides can be divided into two parts: the first part is a short range repulsion resulting from the electronic interaction of hydrogen as described by the Switendick's minimum H–H distance criterion (which is obtained from the electronic structure calculation). The second part is a long range attraction caused by the effective elastic interaction through the

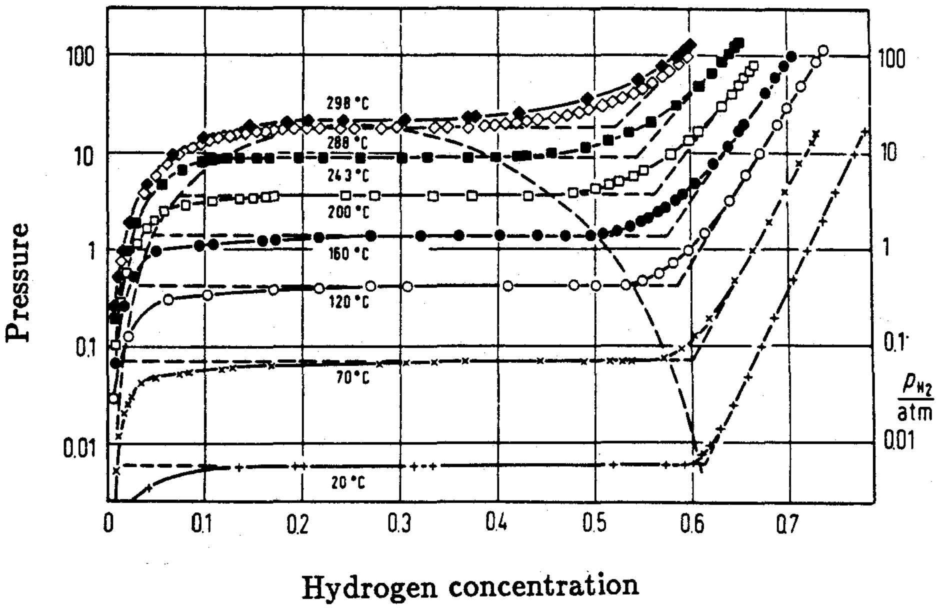

Fig.2.7 Pressure-concentration isotherms of PdH with bulk palladium at various temperatures. (Taken from ref. 2.21.)

overlap of strain fields induced by the hydrogen atoms in the metal lattice [2.22]. In a realistic treatment the metal lattice is therefore not inert, but rather plays a dominant role determining the nature of hydrogen- hydrogen interactions which lead to hydrogen phase separation.

In the second type of phase transformation, a structural change is observed in the host material with increasing hydrogen content. For example, pure Zr has an hcp structure , but ZrH_y with $1.0 \leq y \leq 1.65$ has an fcc structure. The origin of this transformation is the relative change in the free energies of the two hydrogen-containing structures. A tetragonal distortion of the fcc lattice has also been observed when the hydrogen concentration y is greater than 1.75 [2.23]. The phase transformation of metallic alloys upon hydrogen absorption is even more complicated. In the present work, we have observed that fcc $Zr_{0.80}Rh_{0.20}$ decomposes into a two phase mixture of (fcc $ZrH_2 + Zr_2RhH_y$) upon hydriding at temperatures above 220°C. Such kind of decomposition requires a long range diffusion of metal atoms which can sometimes be suppressed kinetically (as will be discussed later). Finally, it is the subject of this thesis to demonstrate another interesting type of transformation—the crystal to amorphous transformation upon hydriding. The details of this will be elucidated in the following chapters.

III. EXPERIMENTAL DETAILS

§3.1 SAMPLE PREPARATION

The alloys used in this study were prepared by rf levitation melting of appropriate constituents on a water cooled silver boat under a titanium gettered argon atmosphere. The purity of starting materials was 99.9% or better. The major impurity in zirconium was hafnium and vice versa. Before the melting, individual elements were weighed to within an accuracy of $\pm 0.1mg$ in order to obtain the desired compositions. Ingots were turned over and remelted, and then broken apart to check for homogeneity visually. The typical weight of ingots ranged from 1 to 3 grams.

Samples, in the form of foils about 30 microns thick, were obtained by piston-anvil quenching [3.1] as illustrated in Fig. 3.1a. Other samples (thin ribbons) were produced using the melt-spinning method [3.2] as illustrated in Fig.3.1b. With these techniques, molten alloys can be quenched to room temperature at rates as high as $\sim 10^7$ K/sec. The quenching rate during melt-spinning can be controlled by varying the operating parameters, such as the wheel speed, the hole size of the quartz nozzle, and the temperature of the molten alloy.

§3.2 HYDRIDING EXPERIMENTS

Hydrogen was introduced into the sample from the gas phase. Fig. 3.2 illustrates the apparatus for hydriding a sample at one atmosphere of hydrogen gas pressure or below. Pre-weighed samples were placed in a pyrex tube which was con-

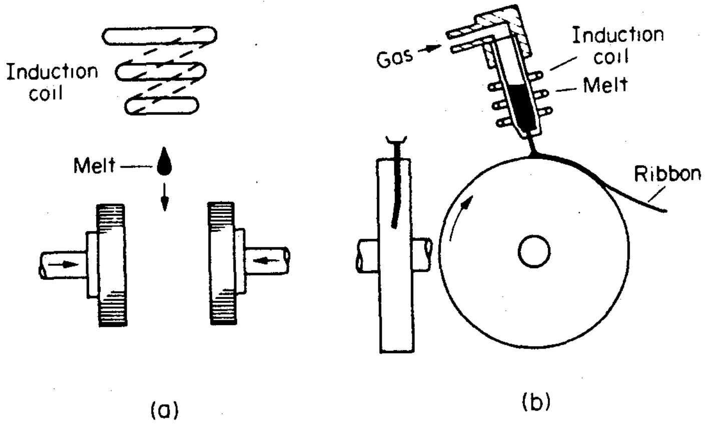

Fig.3.1 Apparatus for rapid quenching: (a) a piston and anvil apparatus and (b) a melt-spinning apparatus. (Taken from ref. 3.5.)

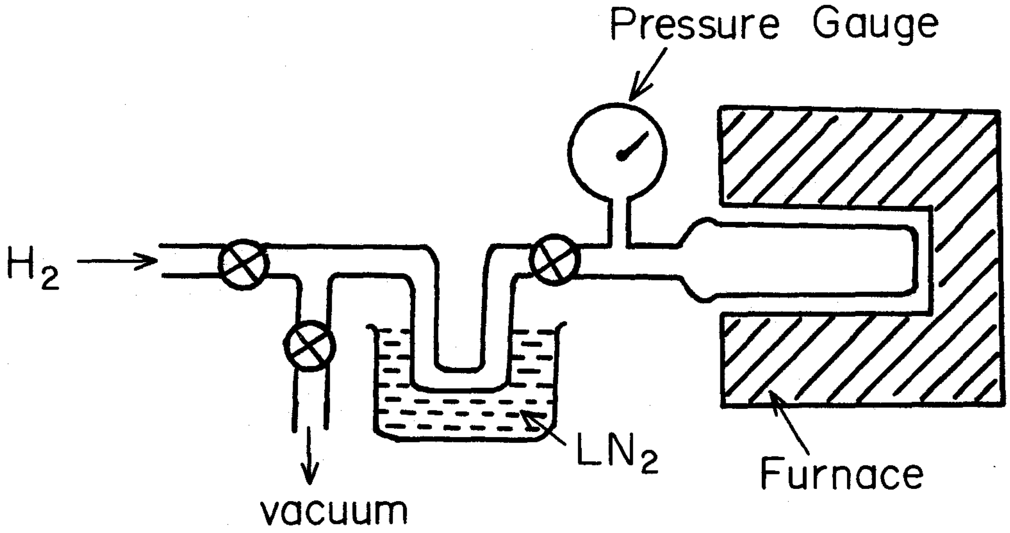

Fig.3.2 The hydriding apparatus.

nected to a Wallace-Tiermann digital pressure gauge, having a sensitivity of 0.001 psi. Stainless steel tubing was used for the plumbing to insure the minimum leakage of hydrogen and outgassing. The system was closed, and impurities removed by alternately evacuating the system and flushing it with hydrogen gas at room temperature. After this process had been repeated several times, hydrogen gas was introduced up to a desired pressure (usually 10 psi). A liquid nitrogen cold trap was also used to help remove impurities from the H_2 gas. The tube was then placed in a microprocessor controlled electrical furnace, having temperature fluctuations less than $\pm 1°C$. After the sample was hydrided, the tube was taken out of the furnace, and allowed to come to thermal equilibrium. The pressure was measured again.

The molar hydrogen absorbed is determined by the following formula :

$$\Delta n_H = \frac{V}{R}\left(\frac{P_1}{T_1} - \frac{P_2}{T_2}\right)$$

where V is the volume of the reaction tube, R is the ideal gas constant, P_1 and T_1 are the pressure and temperature of H_2 gas before hydriding, and P_2 and T_2 are the corresponding parameters after hydriding.

The amount of hydrogen in the sample was also determined by massing samples before and after hydriding on a micro-balance with sensitivity of 0.001 mg.

§3.3 X-RAY DIFFRACTION

X-ray diffraction was performed on a GE XRD-5 scanning diffractometer or a Phillips Norelco vertical diffractometer, using the θ-2θ geometry (i.e., the angle between the X-ray source and the detector was twice of that between the X-ray source and the sample surface). For sample characterization, the copper K_α characteristic radiation ($\lambda = 1.54178\AA$) was used. The angular divergence of the X-ray beam was determined by a 1° incident slit which was placed between the source and the sample. A Soller slit placed before the incident slit was used to eliminate the vertical divergence of the beam from the diffraction plane. A 0.1° receiving slit was placed in front of the detector. A Ni filter was used to reduce the relative intensity of copper K_β radiation.

To obtain the radial distribution function for amorphous metallic alloys, detailed X-ray diffraction measurements were performed on a Phillips Norelco vertical powder diffractometer using Mo K_α radiation ($\lambda = 0.7107\AA$). Higher K values could be accessed by using a radiation with the shorter wavelength; this was essential for the Fourier transformation. A 0.04-inch zirconium filter was used to reduce the Mo K_β radiation. A LiF focusing crystal monochromator tuned for the Mo K_α radiation was placed before the detector to eliminate scattering contributions from radiations other than Mo K_α and to reduce contributions from fluorescence and Compton scattering. A wide 0.2-inch receiving slit was used to get a higher intensity and better statistics, since the angular resolution is not crucial in the X-ray diffraction of amorphous samples. The apparatus for the detailed X-ray diffraction is schematically illustrated in Fig. 3.3.

Samples used for detailed X-ray diffraction were prepared by glueing three or four layers of ribbons or foils onto a pyrex slide using acetone diluted Duco cement. The total thickness of the samples was approximately 150 μm which was much larger than the penetration depth of the X-rays (typically 10μm for Zr-Rh alloys). This eliminates any scattering from the substrate; that is, the sample can be regarded as infinitely thick with respect to the X-ray radiation.

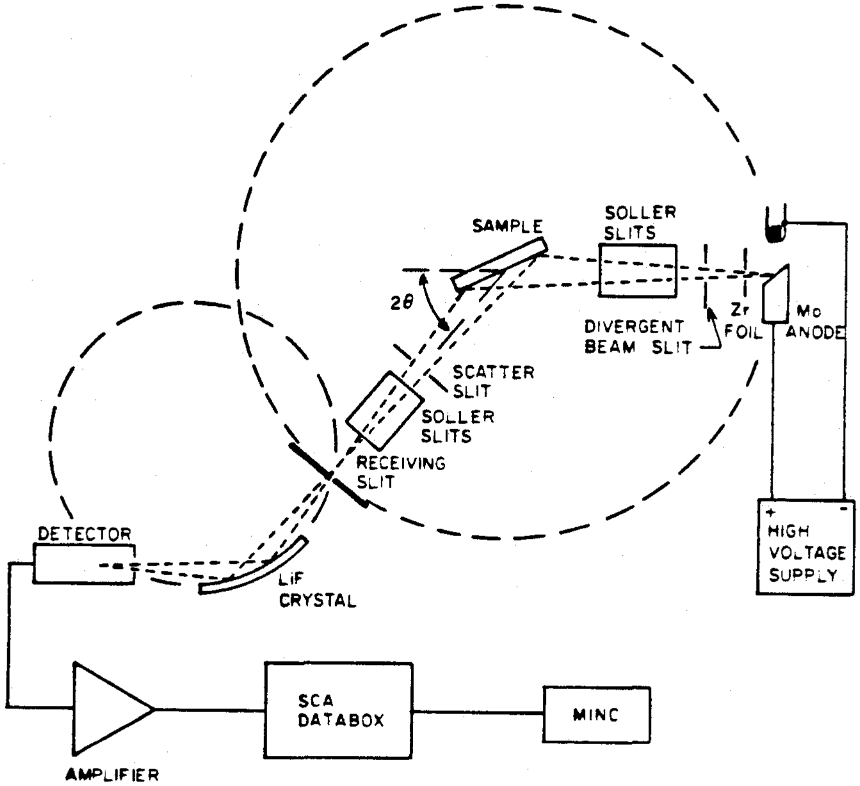

Fig.3.3 A schematic arrangement of X-ray diffractometer used for X-ray analysis. (Taken from ref. 2.6.)

The data points were stored in a microprocessor controlled DATABOX, which also controls the scanning step and counting time of the diffractometer. They were then transfered to a MINC PDP-11/23 microcomputer for further analysis.

§3.4 DIFFERENTIAL SCANNING CALORIMETRY (DSC)

Differential scanning calorimetry is a technique for monitoring the difference in heat capacity of two samples. The difference between heat flows from the sample and an inert reference material is measured, when they are both heated at a constant rate. Whenever a material undergoes a first-order phase transformation, heat absorption or release is always involved, while if there is a second-order phase transformation in the material, a discontinuous change of heat capacity should occur. Therefore, DSC is a very powerful probe to characterize phase transformations in materials. A Perkin–Elmer DSC–4 apparatus used in this study is designed to determine the enthalpy change or the heat capacity change during phase transformations by directly measuring the differential heat flow required to keep the sample and the reference at the same temperature. The apparatus is programmed to scan a temperature range at a constant heating rate.

As illustrated in Fig. 3.4, a DSC–4 set up uses two separate heaters for the sample and the reference [3.3]. Two platinum temperature sensors serve dual purposes. One is used to provide feedback to the temperature controller, so that the temperature T of the sample and reference can be increased at a preprogrammed rate. Second, any temperature difference between the sample and reference detected by the sensors is eliminated by adjusting the power input to the sample and reference. A signal proportional to the difference between the heat input to the sample

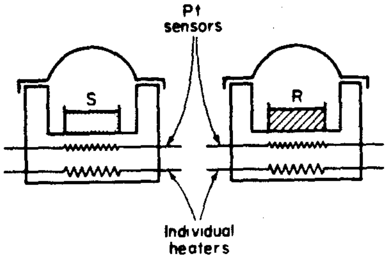

Fig.3.4 A schematic illustration of a DSC apparatus. (Taken from ref. 3.3).

and that to the reference, dH/dt, is recorded as a function of the temperature, T.

DSC samples, typically weighing from 3 to 10 mg, were hermetically sealed in aluminum pans under inert gas atmosphere. Baselines were obtained by running a DSC with empty aluminum pans in the sample and reference pan holders. The actual DSC scans of samples always immediately followed baseline scans in order to obtain greater precision. The data were plotted with the data of the baseline scan subtracted from the actual sample scan data.

§3.5 HYDROGEN DEPTH PROFILING

Leich and Tombrello [3.4] were the first to use the resonant nuclear reaction $^{1}H(^{19}F, \alpha\gamma)^{16}O$ at the resonance energy of 16.44 MeV to study the hydrogen profile in the material. This technique has now become a popular technique for analyzing the hydrogen distribution in materials, because it is non-destructive and relatively accurate for submicron hydrogen profile determination. In present work, resonant nuclear reactions using a tandem van de Graaff accelerator were used to examine the hydrogen concentration profile in some amorphous zirconium rhodium hydrides. Groups of samples and a tourmaline (or zoisite) standard of known water concentration were placed in a sample chamber of the tandem accelerator at Caltech, and evacuated to a pressure of 10^{-6} torr. The experiments were performed either at room temperature or at liquid nitrogen temperature by cooling the samples through a cold finger.

In one set of experiments, the resonant nuclear reaction $^{15}N(^{1}H, \alpha\gamma)^{12}C$ was used as a probe for hydrogen (see Fig. 3.5). The sample was bombarded with ^{15}N

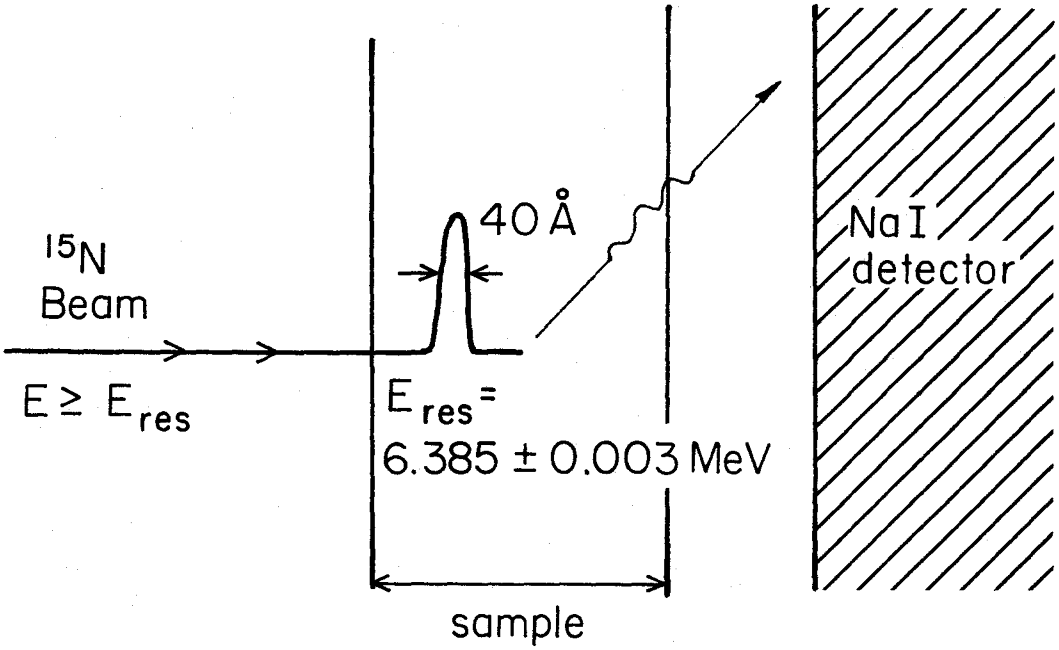

Fig.3.5 A schematic representation of the ^{15}N resonance profiling method.

nuclei and the yield of characteristic 4.43 MeV gamma radiation was measured with a NaI detector. When the sample is bombarded with ^{15}N at the resonance energy $E_{res} = 6.38$ MeV, the yield of gamma radiation is proportional to the number of hydrogen atoms on the surface of the sample. When the energy of the incident ^{15}N nuclei is increased, the surface hydrogen is no longer detected because the energy lies above the resonance . However, as the ^{15}N loses the energy while passing through the solid, it reaches the resonance energy at some characteristic depth. Therefore, the gamma ray yield is proportional to hydrogen at this depth. The hydrogen concentration profile was thus determined by measuring the gamma ray yield versus the energy of the ^{15}N. In this reaction, the depth resolution near the sample surface is about 4.5 nm.

A similar experiment was performed using $^{19}F(^{1}H,\alpha\gamma)^{16}O$ nuclear reaction which has a resonance energy of 6.42 MeV. This reaction has a higher sensitivity, therfore it is suitable for detecting smaller amounts of hydrogen in metals. The depth resolution of this reaction is 15 nm at the surface and 25 nm at a depth of 1.0 μm.

§3.6 TRANSMISSION ELECTRON MICROSCOPY AND ENERGY DISPERSIVE SPECTROSCOPY

Transmission electron microscopy (TEM) was performed on a Phillips EM420 electron microscope located at the USC Electron Microscopy Center. The samples used for examination were 3 mm disks which were thinned to a thickness of several hundred anstroms by either ion-milling or electro-chemical polishing. The solution used for polishing on Zr-based alloys was 10% butanol alcohol, 6% perchloric acid and 84% methanol.

Quantitative analysis of the local chemical composition of materials was carried out by energy dispersive spectroscopy (EDS). The EDS was performed on an EDAX energy dispersive spectrometer attached to the Pillips EM420 electron microscope. Fluorescent X-rays corresponding to characteristic lines of the elements to be analyzed are generated when an electron beam (with a size of 40 Å) hits the surface of the sample. The signal was measured by a Si detector with a 40° take-off angle. The sample tilting angle was 10°. Since the intensity of X-ray emission is, to a first approximation, proportional to the amount of this element present at the spot where the sample surface is hit by the electron beam, the number of X-ray quanta is a measure of composition.

IV. RESULTS AND INTERPRETATIONS

The motivation of the present study is to investigate the crystal instability and the amorphization induced by hydrogen absorption of some early transition metal–late transition metal alloys. The Zr–Rh, Zr–Pd and Hf– Rh systems are chosen for this study with compositions which lie on the early transition metal-rich parts of the phase diagrams. Since Zr and Hf react with hydrogen exothermically and form stable hydrides and Rh and *Pd* are known to be good catalysts for hydrogen (i.e. hydrogen molecules can dissociate easily into atoms and be chemisorbed on the surface of *Rh* and *Pd*), these alloys are expected to take a large amount of hydrogen under one atmosphere. Specimens used for this study were prepared by rapidly quenching the as-cast ingots. Ribbons and foils were produced by splat quenching or melt-spinning, and then hydrided following the procedures described in chapter 3. Several experimental techniques were applied to examine properties of samples as a function of hydrogen concentration. Various properties of hydrides produced by hydriding crystalline alloys and metallic glasses were compared.

§4.1 STRUCTURE AND MORPHOLOGY [4.1]

4.1.1 Structure and Morphology of As-quenched Alloys

The X-ray diffraction patterns indicated that as-quenched $A_{1-x}B_x$ (A=Zr, Hf; B=Rh, Pd) with $0.20 \leq x \leq 0.25$ usually (but not always) contained substantial amounts of the amorphous phase, while samples with $0.15 \leq x \leq 0.20$ contained nearly single phase metastable fcc solid solutions. In general, the smaller the Rh content in the ingot, the more the fcc phase (and less amorphous phase) one obtains from the rapid quenching. Further decrease of x made rapid quenching very difficult because of the high melting temperature of Zr-rich (or Hf-rich) alloys. Such alloys tend to react with the quartz crucibles used in melt-spinning to form Zr (or Hf) oxide which usually blocks the nozzle hole. As-quenched samples with $x > 0.25$ were found to have a A_2B phase with the $CuAl_2$ structure in coexistence with the amorphous phase. Therefore only alloys with $0.15 \leq x \leq 0.25$ were chosen for this study.

The typical X-ray diffraction patterns from both sides of melt-spun $\mathrm{Zr}_{0.80}\mathrm{Rh}_{0.20}$ ribbons are shown in Fig. 4.1. The strong peak at $2\theta = 36.8°$ indicates that the fcc crystals grow with [002] texture normal to the plane of the quenched ribbon. This is the direction of the temperature gradient during rapid cooling. It is noticed that the intensities of Bragg reflections from the wheel side of the ribbon are less than that from the free side of the ribbon, indicating that the size of individual crystalline grains increases with the distance from the wheel. This is expected since solidification far from the wheel occurs at a lower quenching rate than that near the wheel [4.2]. Grain growth is thus more extensive far from the wheel.

The TEM micrographs and selected area diffraction (SAD) patterns of the same as-quenched $Zr_{0.80}Rh_{0.20}$ are shown in Fig. 4.2. The sample, although single phase, consisted of many crystalline phase domains. Traces of amorphous phase were found by TEM and SAD only at grain boundaries. The interface between the crystalline phase and the amorphous phase was very sharp and well-defined. The fringes on the TEM micrograph (seen at higher magnification of a single domain) could represent stacking faults in the deformed crystals. (Fig. 4.3). The energy-dispersive X-ray spectroscopy (EDS) was performed to determine the local atomic

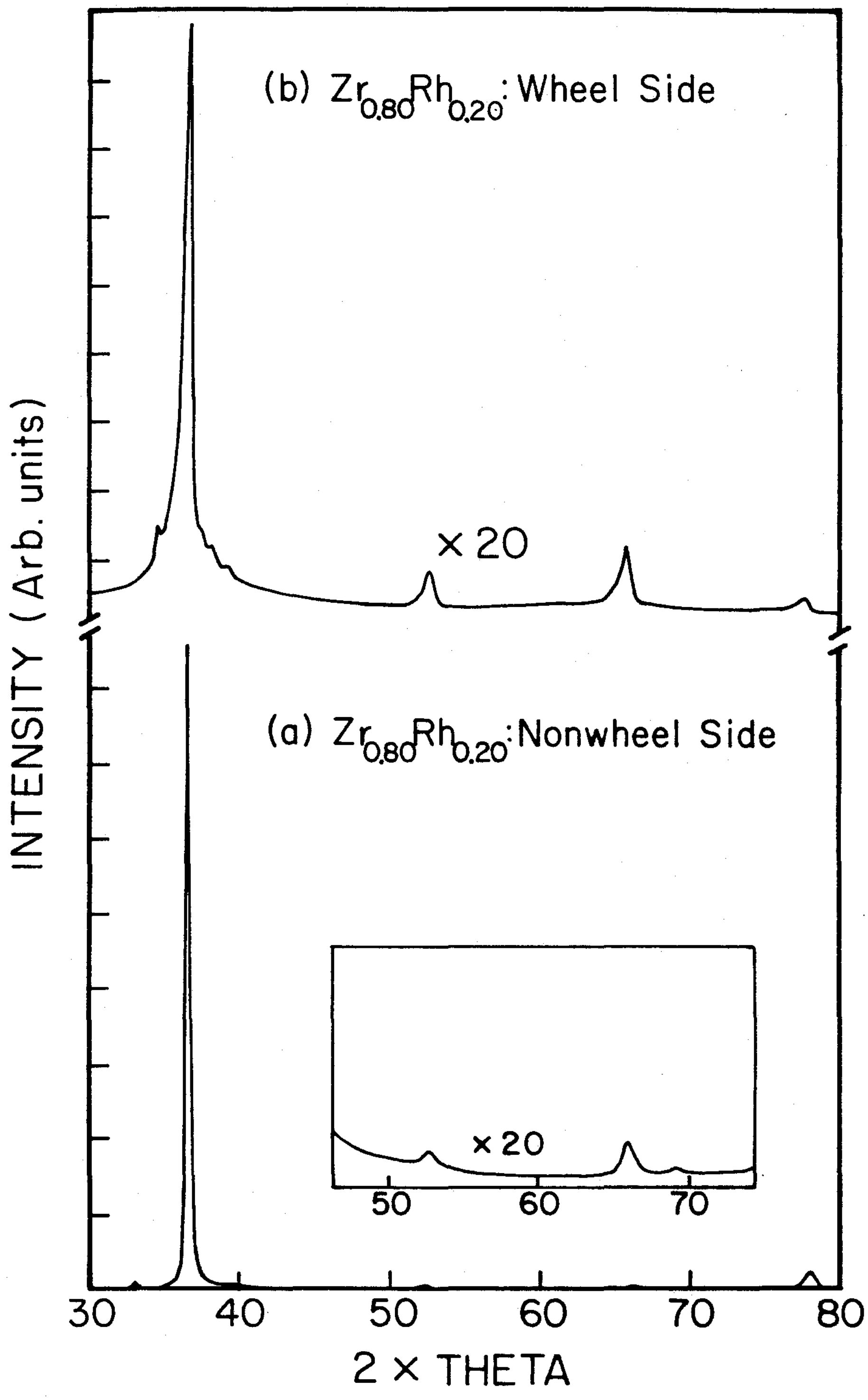

Fig.4.1 Typical X-ray diffraction patterns of the melt-spun $Zr_{0.80}Rh_{0.20}$ ribbons. The top curve is the pattern obtained from the wheel side of the ribbon and the bottom curve is that from the nonwheel side of the ribbon.

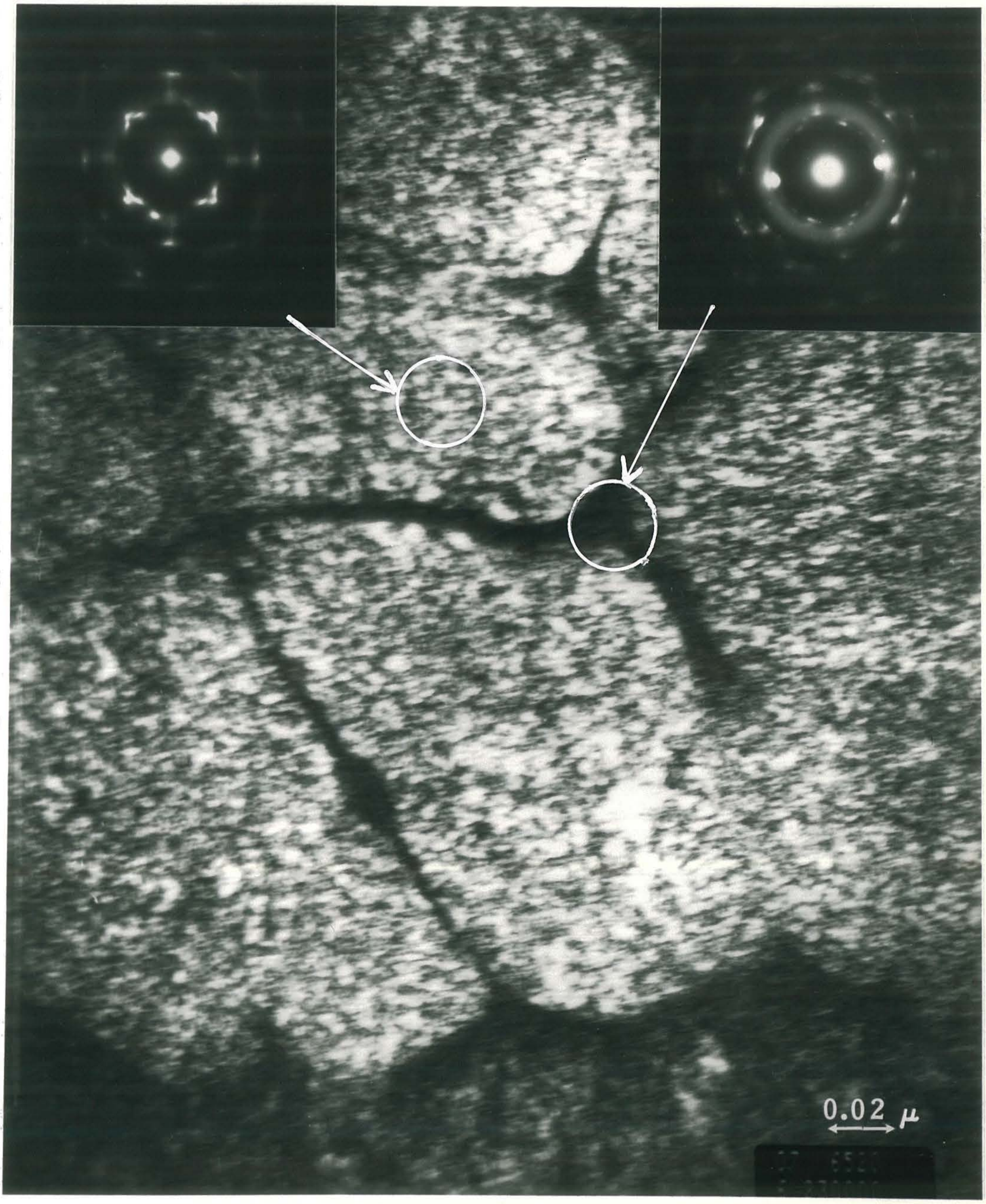

Fig.4.2 TEM micrograph and selected area electron diffraction patterns of the as-quenched $Zr_{0.80}Rh_{0.20}$. The single crystal diffraction pattern is from the interior of a crystalline grain and the partially amorphous pattern is from a grain boundary region.

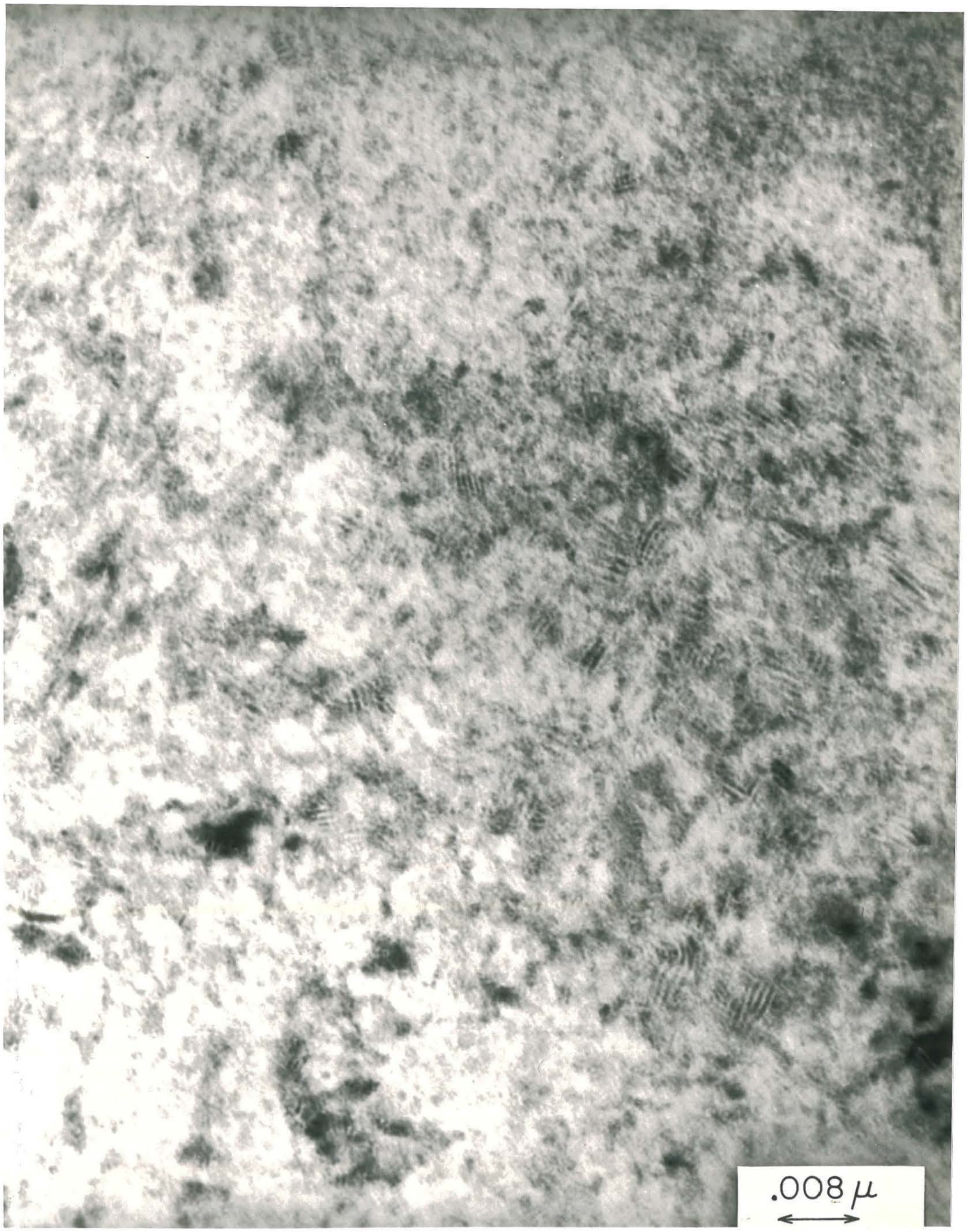

Fig.4.3 A higher magnification TEM micrograph of the as-quenhced $Zr_{0.80}Rh_{0.20}$.

compositions at both interiors and grain boundaries of the crystalline grain (Fig. 4.4). The intergrated intensity of each X-ray characteristic radiation is proportional to the atomic fraction of each elements. The atomic ratio of Zr and Rh as a function of the ratio of the integrated L_α fluorescence intensity is given by [4.25]:

$$\frac{C_{Zr}}{C_{Rh}} = \frac{\kappa_{Zr} \times I(L_\alpha^{Zr})}{\kappa_{Rh} \times I(L_\alpha^{Rh})}$$

where the κ_{Zr} and κ_{Rh} are the L_α X-ray generation constants of Zr and Rh, respectively. The computer intergration shows that the atomic ratio of Zr/Rh was 4.5 at the interior of a grain and is 2.6 at the grain boundary (the nominal atomic ratio of $Zr_{80}Rh_{20}$ is 4.0). This shows that at least a moderate amount of chemical segration occurs during growth of the fcc crystallites. Rhodium is apparently ejected by the growing grains leaving a Rh-rich melt which finally solidified to amorphous phase along grain boundaries so that the atomic fraction of Rh atoms was higher in the amorphous region than it was in the crystalline grains.

4.1.2 Interpretation

To determine whether the metallic glass will easily form during the rapid quenching, one first asks whether there exists a competing crystalline phase at the same composition. One defines T_o to be the maximum temperature at which a partitionless crystallization can proceed [4.3]. One then considers whether there is a constraint to prevent this partitionless crystallization from happening. Another way of addressing this is to ask whether the glass transition temperature T_g is above T_o. If T_g is larger than T_o, then the liquid will configurationally freeze to from glass before it can crystallize partitionlessly. Since T_o for the fcc phase is the temperature at which the free energy of the liquid phase equals the free energy of the fcc phase, one can calculate the T_o curve based on the regular solution approximation formula

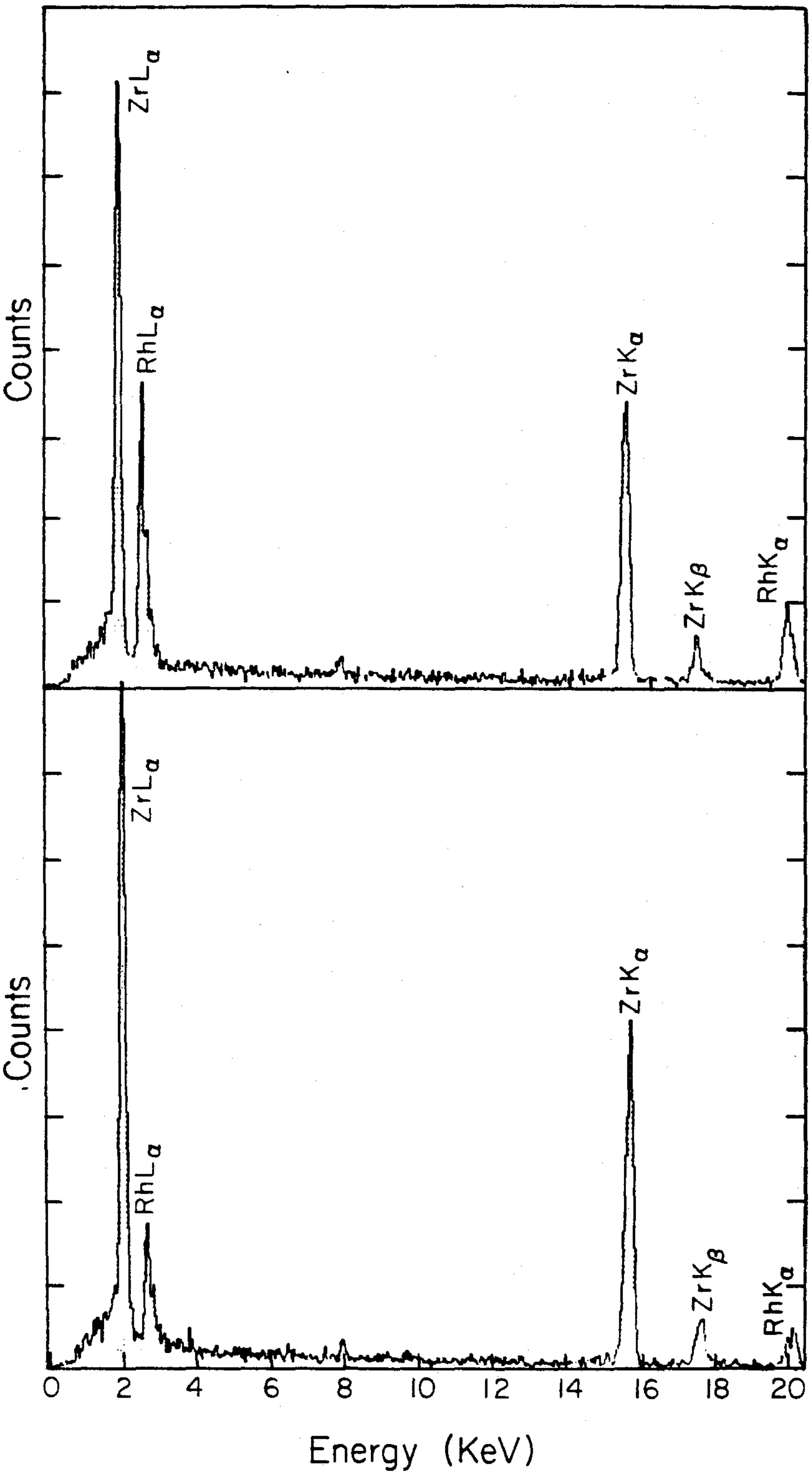

Fig.4.4 Energy dispersive spectra for as-quenched fcc-$Zr_{0.80}Rh_{0.20}$. Top curve: EDS from the interior of a crystalline grain. The atomic ratio of Zr to Rh is 4.5. Bottom curve: EDS from the grain boundary. The atomic ratio of Zr to Rh is 2.6.

for free energies $F_r(x,T)$ [4.4]:

$$F_r(x,T) = (1-x)F_r^{Zr} + xF_r^{Rh} + RT(x\ln(x) + (1-x)\ln(1-x)) - L_r x(1-x)$$

where the subscript r represents the fcc phase or the liquid phase, x is the atomic fraction of Zr, F_r^{Zr} and F_r^{Rh} are the Helmholtz free energies of Zr and Rh, and L_r is the regular solution parameter given by ref. 4.4. The T_o curve is obtained by solving the equation $F_{liquid}(x,T_o) = F_{fcc}(x,T_o)$ at various x. A computer calculated T_o curve for binary Zr–Rh system is superimposed on the phase diagram given in Fig. 4.5. Although the fcc phase exists as a competing phase with the amorphous phase at all compositons, the T_o line drops dramatically near the eutectic region. Since T_g is not as sensitive to the compositon as T_o is, the T_o falls below the T_g near the eutectic composition such that the amorphous phase forms easily near the eutectic region. Similar results have also been observed in the Ti–Cu system by Massalski et al [4.5]. Massalski also pointed out that although the bcc phase is a competing phase with amorphous phase, this structure has never been observed during rapid quenching. The reason may be that the bcc structure is a open structure with a coordination number of 8, and the fcc structure is a close packed structure with a coordination number of 12. Therefore the fcc structure more closely resembles the liquid in short range coordination, as the latter also has a coodination number of ~12.

One must be aware of that a crystallization reaction involving phase separation is kinetically more difficult than partitionless crystallization, owing to the fact that it requires transport of atoms over at least a distance of the order of the critical nuclei size of the product phases. Although phase separation is thermodynamically possible, it may be kinetically forbbiden even if polymorphic crystallization is not kinetically forbiden (see Fig. 2.2).

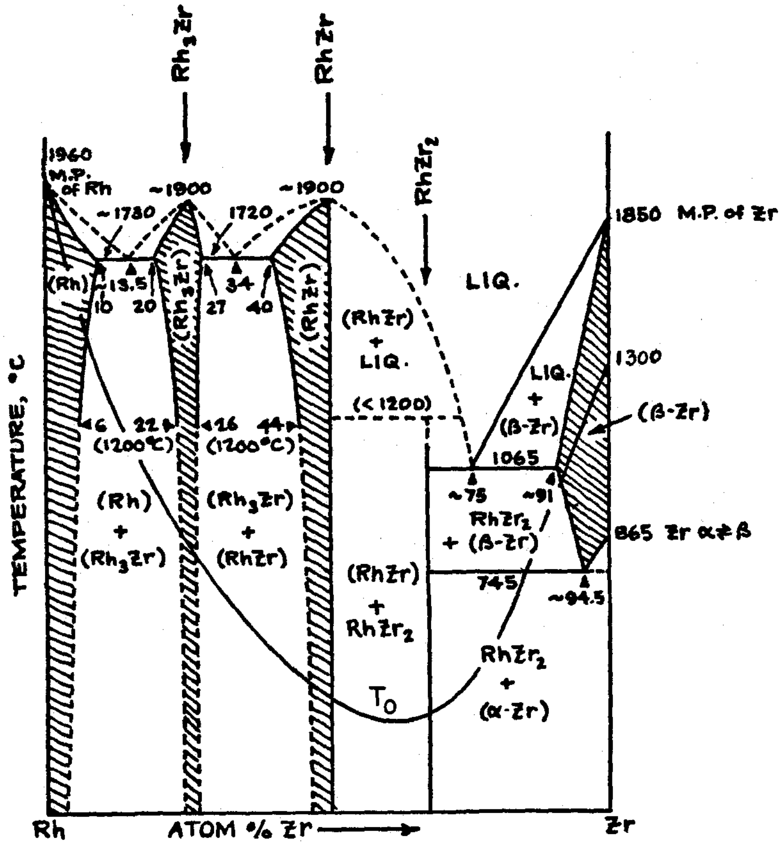

(Schematic only; not to scale)

Fig.4.5 The phase diagram of Zr–Rh system. (From W.G. Mofatt, *Handbook of Binary Phase Diagrams*, General Electric, 1978). The T_o curve (the solid curve) is calculated based on the regular solution approximation.

The incomplete solute trapping mentioned above was the reason why the amorphous regions near the grain boundaries had higher Rh concentration. Rh atoms tended to remain in the melt rather than be retained in solid solution. This phenomenon is due to the fact that the melt can accommodate atoms of different size more easily than the crystal [4.6]. This enrichment of Rh atoms in the unsolidified melt results in a shift of local composition of the undercooled melt toward the eutectic composition. This explains why an amorphous phase is formed in the grain boundaries.

4.1.3 Amorphous Phase Formation During Hydriding

The crystalline to amorphous phase transformation has been observed in fcc solution phases of $Zr_{1-x}Rh_x$, $(0.15 \leq x \leq 0.25)$; $Zr_{1-x}Pd_x$, $(0.17 \leq x \leq 0.21)$; and $Hf_{1-x}Rh_x$, $(0.19 \leq x \leq 0.25)$ during reaction of as-quenched polycrystalline alloys with hydrogen gas at temperatures below $220°C$. In Fig. 4.6, X-ray diffraction (XRD) patterns are shown for the as-quenched fcc $Zr_{0.82}Pd_{0.18}$ and its hydride $(Zr_{0.82}Pd_{0.18})H_{1.3}$ obtained by hydridng the as-quenched ribbons at $210°C$ and 1 atmosphere for 6 days. In the X-ray pattern of the reacted sample, one observes very small and broadened Bragg peaks superimposed on the amorphous band, at angles slightly below the Bragg angles of the unhydrided sample. This indicates that there are still residual microcrystallites in the reacted sample (i.e., the amorphization is not complete), and that the fcc phase can absorb a substantial amount of hydrogen. A similar crystalline to amorphous phase transformation has also been observed during hydrogen absorption of the original fcc $Hf_{1-x}Rh_x$ $(0.19 \leq x \leq 0.25)$. The X-ray patterns of the as-quenched fcc $Hf_{0.75}Rh_{0.25}$ and that of the hydrided amorphous $(Hf_{0.75}Rh_{0.25})H_{1.2}$ are given in Fig.4.7 (the sample was reacted with hydrogen at

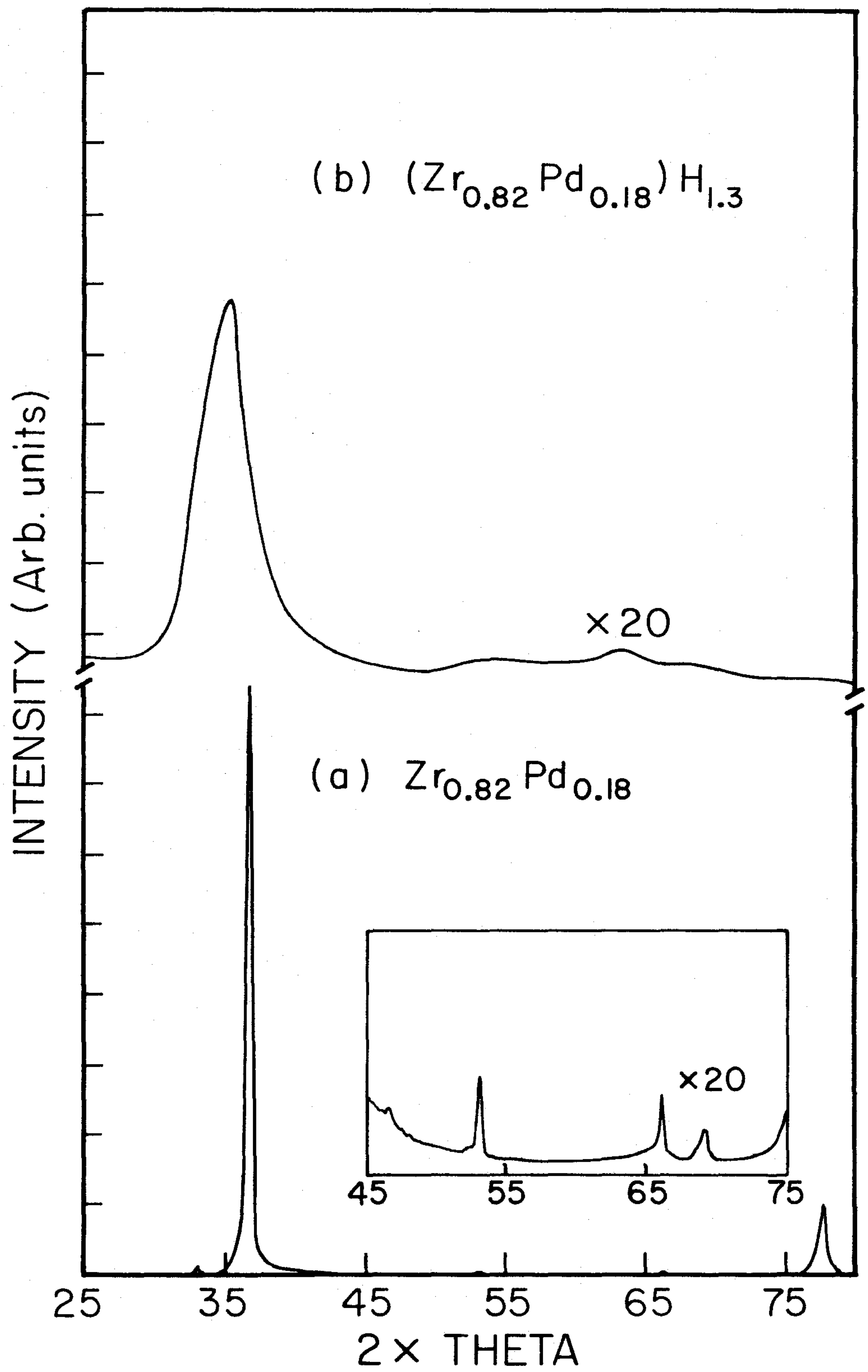

Fig.4.6 X-ray diffraction patterns of $Zr_{0.82}Pd_{0.18}$ before (a) and after (b) hydrogen absorption. The original sample has a single phase fcc structure.

$190°C$ and 1 hydrogen atm. for 6 days).

Note that the crystal to amorphous transformation upon hydrogen absorption has only been observed when the hydriding temperature is below $230°C$. When the reaction is carried out at higher temperatures ($230°C < T < 730°C$), one begins to see the nucleation and growth of fcc-ZrH_y (or fcc-HfH_y) crystals and the final product is a phase mixture of Zr_2AH_z (A=Rh, Pd) and fcc-ZrH_y (or Hf_2RhH_z and HfH_y). (It has been reported [4.17] that the amorphous $(Zr_{0.75}Rh_{0.25})H_{1.3}$ decomposes into a mixture of ZrH_y and Rh metal around a temperature of 730°C. This suggested that equilibrium product at high hydrogen concentration may be ZrH_y and Rh.)

The structure of $Zr_{1-x}Rh_xH_y$ ($0.15 \leq x \leq 0.25$) system at various hydrogen concentrations has been carefully analyzed using X-ray diffraction. Fig. 4.8 shows the XRD of $Zr_{0.80}Rh_{0.20}$ at various hydriding times (reacted at $175°C$ and 1 atm.). The evolution from the crystalline phase to the amorphous phase is vividly depicted in this figure: as the reaction proceeds, an amorphous phase grows at the expense of the original crystalline phase; no other intermediate phases develop throughout the reaction. One notices that the Bragg peaks shift to lower angles, decrease in intensity and broaden as the reaction proceeds.

Lattice parameters of the crystalline phase of $Zr_{0.8}Rh_{0.2}H_y$ are plotted against the fraction of amorphous phase in the materials (A(0)-A(t))/A(0) in Fig. 4.9, where A(0) and A(t) denote the integrated intensities of X-ray diffraction from the crystalline phase initially (as- quenched) and reaction time t. Since A(t) is as a first approximation (assuming no texture change during reaction) proportional to the amount of crystalline material remaining in the sample, (A(0)-A(t))/A(0)

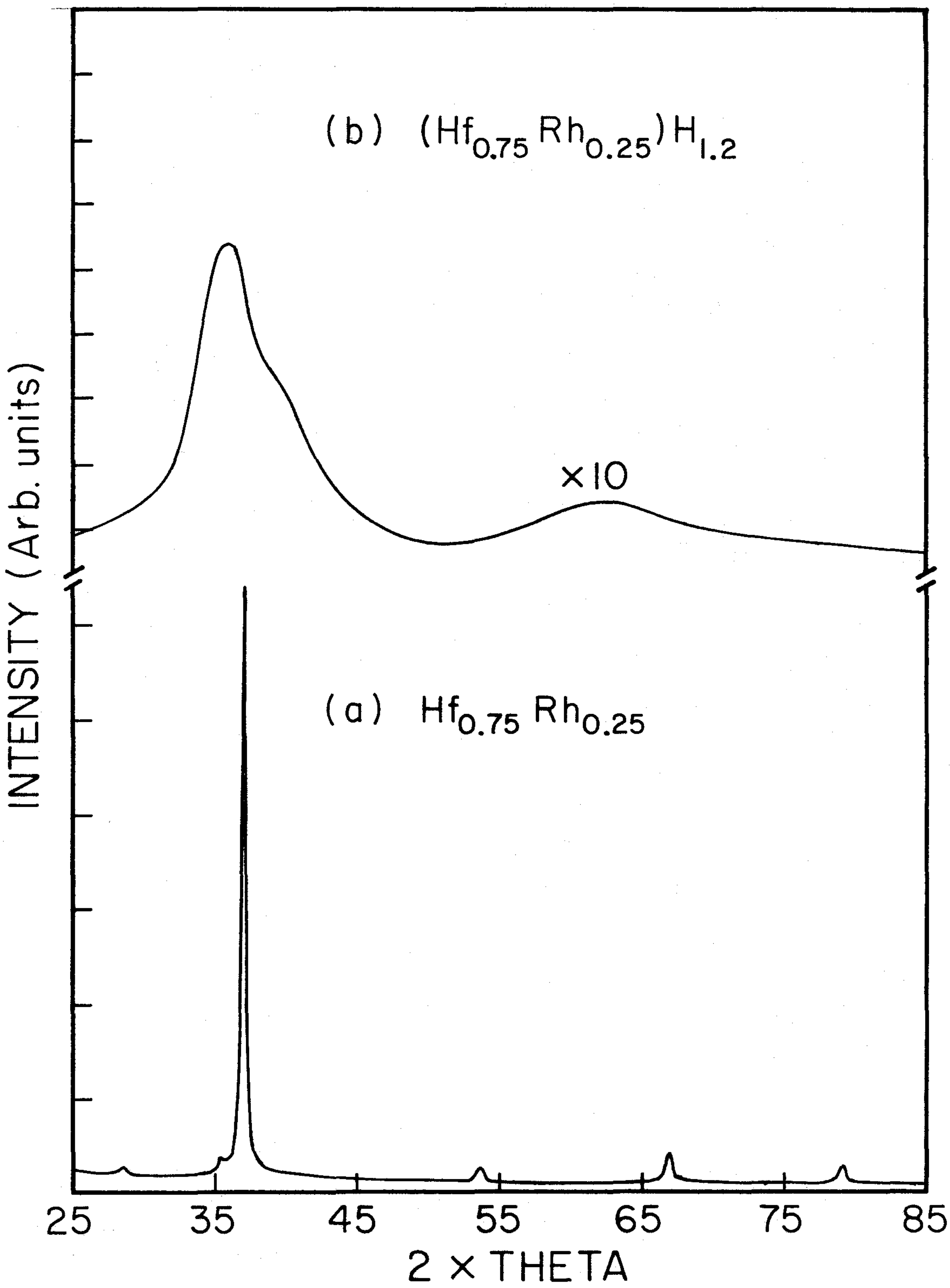

Fig.4.7 X-ray diffraction patterns of $Hf_{0.75}Rh_{0.25}$ before (a) and after (b) hydrogen absorption.

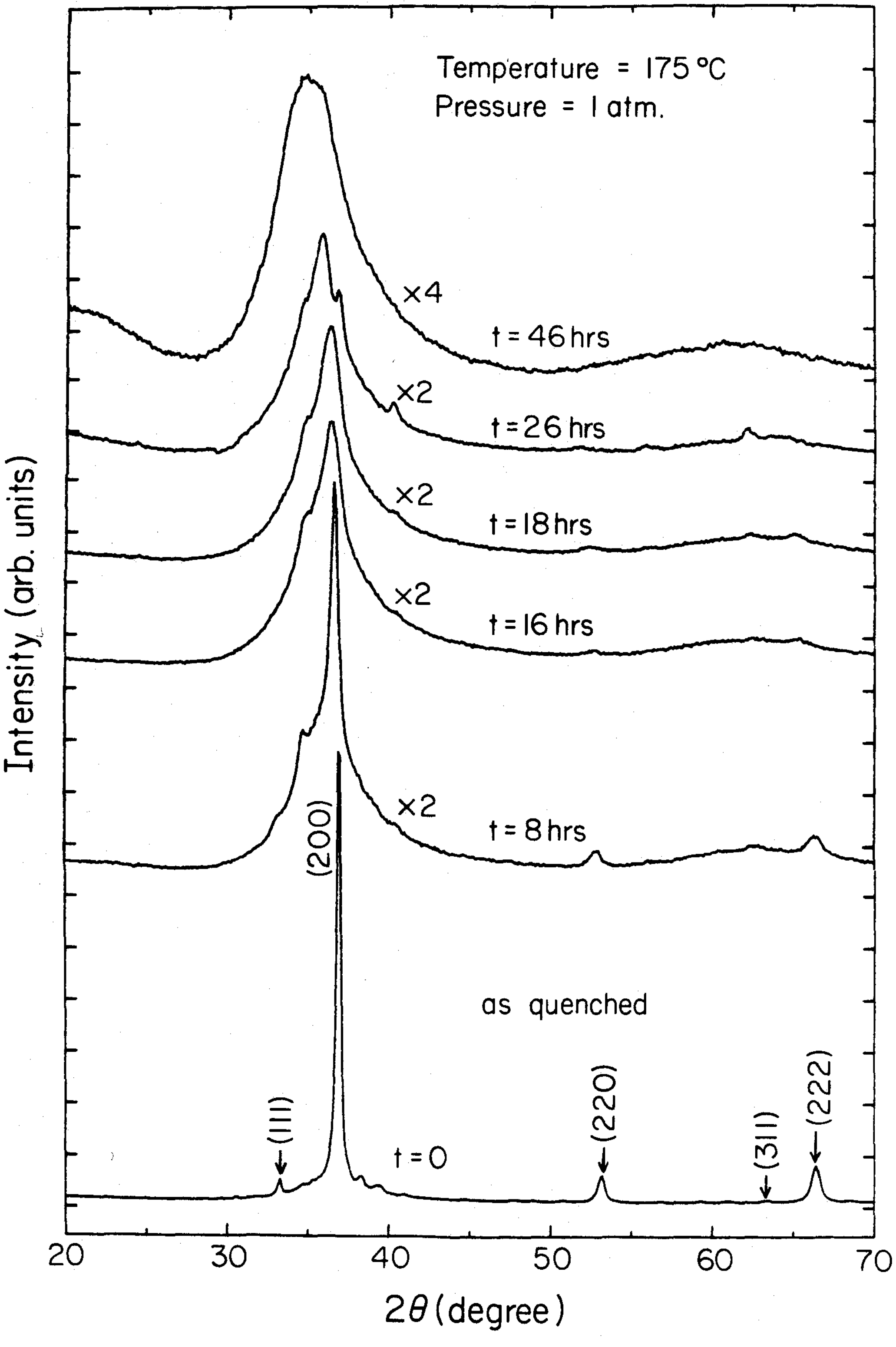

Fig.4.8 The X-ray diffraction patterns for $(Zr_{0.80}Rh_{0.20})H_y$ at various hydriding times. The top pattern is the X-ray diffraction pattern of $(Zr_{0.80}Rh_{0.20})H_{1.0}$.

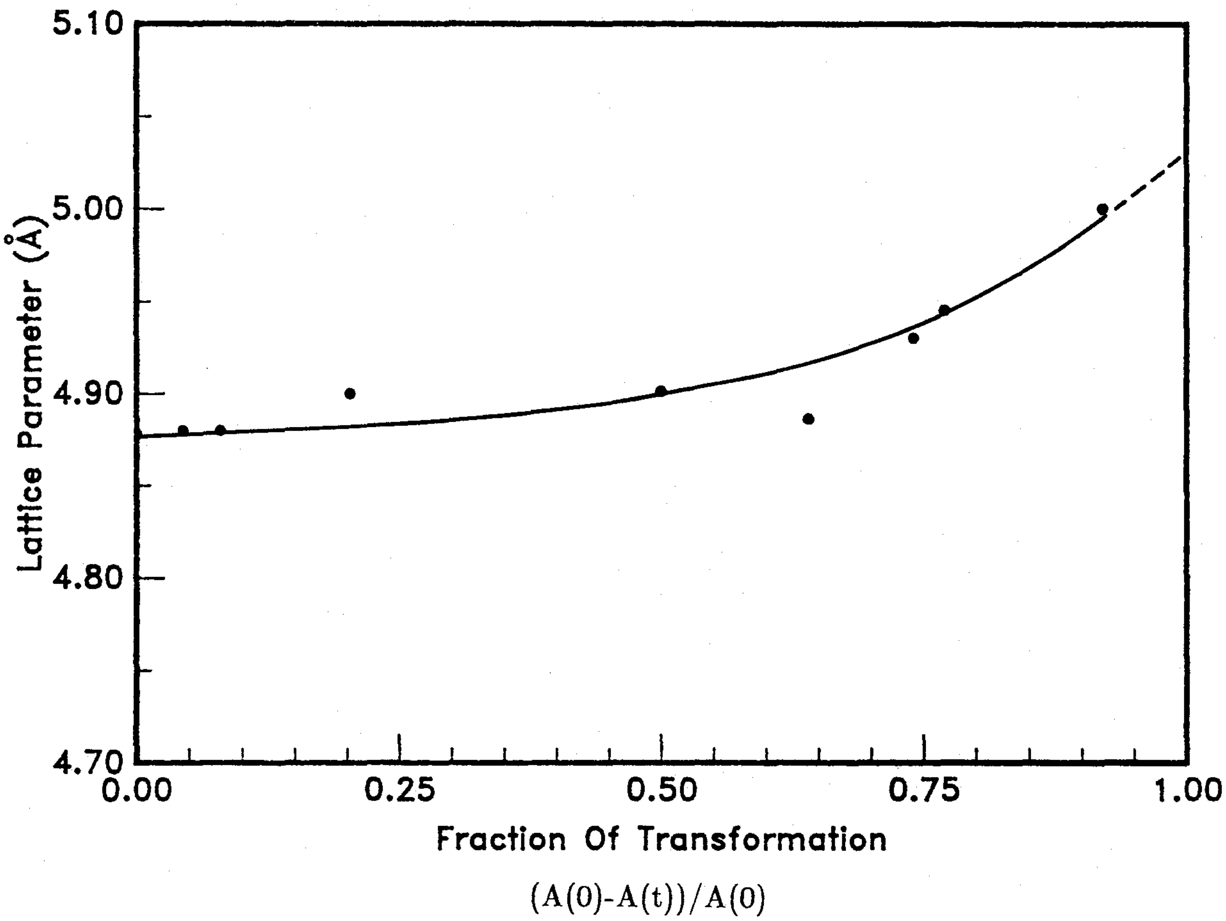

Fig.4.9 Lattice parameters of polycrystalline fcc $Zr_{0.80}Rh_{0.20}$ versus the fraction of amorphization transformation.

represents the fraction of material transformed to the amorphous phase. A 2 % increase of the lattice parameter has been observed through the hydriding reaction. A very small expansion is observed during early stages of reaction, suggesting that the fcc phase does in fact absorb a small amount of hydrogen to form a coherent solid solution. However, this fcc phase becomes thermodynamically unstable with respect to the amorphous phase as the hydrogen concentration increases, inducing a crystal to amorphous transformation. A more significant increase of the lattice parameter occurs during the late stage of reaction. In this stage, a small number of crystals having substantially reduced size are dispersed in the transformed amorphous matrix (see both Fig.4.12 and the fourth pattern from the bottom in Fig. 4.8). Apparently the remaining crystallites have a larger solubility for hydrogen just prior to their complete disappearance to form the final amorphous single phase. Such an effect of enhanced solubility for hydrogen is due to the decrease in the size of crystallites at this stage of reaction which can be described by the Thomson-Freulich equation [4.7]:

$$\ln \frac{X_{C(sat,r)}}{X_{C(sat)}} = \frac{2\sigma V_C}{RTr}$$

where $X_{C(sat,r)}$ is the solubility limit when the crystalline phase occurs as a dipersion of spherical particles of radius r, $X_{C(sat)}$ is the solubility limit when the crystalline phase is massive, V_C is the partial molar volume of the crystalline phase and σ is the amorphous–crystal interface tension. This equation says that the limit of hydrogen solubility in the fcc phase is exponentially proportional to the inverse of the size of crystals, therefore a tremendous increase of the solubility is expected near the completion of amorphization, as the size of the untransformed crystals becomes progressively smaller.

A hydriding experiment under identical conditions was performed in order to determine the hydrogen concentration at various stages of the transformation. The hydrogen-to-metal ratio as well as (A(0)–A(t))/A(0) are plotted as functions of the reaction time in Fig. 4.10. It has been observed that the rate of the hydrogen absorption varies from sample to sample, depending on the surface conditions. However, one can obtain a qualitative picture of the relationship between the fraction of the transformation and the hydrogen concentration. The figure shows that the amorphization has been completed after 46 hours while hydriding is still proceeding. The maximum hydrogen-to-metal ratio that can be reached is 1.38.

The mechanisms of this solid state amorphization reaction were further studied using TEM and SAD. The TEM micrograph along with the SAD patterns of partially hydrided $(Zr_{0.80}Rh_{0.20})H_{0.5}$ are reproduced in Fig. 4.11. The comparison between the micrographs of the as-quenched (Fig. 4.2) and partially hydrided samples shows that the individual crystalline grains shrink, while the amorphous phase, seen as a featureless grey region, grows from the grain boundaries of the crystalline phase. This suggests that the interface is the preferred site for the vitrification of the crystals. One further notices that the interface between the crystalline and amorphous phase remains sharp throughout the reaction; this can clearly be seen from the dark field image of partially amorphized $Zr_{0.85}Rh_{0.15}$ alloy (Fig. 4.12). Fig. 4.13 shows the TEM micrograph and SAD pattern of fully amorphized $(Zr_{0.80}Rh_{0.20})H_{1.0}$. This sample was almost entirely amorphous as illustrated by the SAD pattern taken from a typical featureless region of the sample. The results of SAD also show a few black patches dispersed in the grey amorphous matrix. These are identified as the untransformed residual crystallites.

The EDS analysis performed on random regions of the $(Zr_{0.80}Rh_{0.20})H_{1.0}$ in-

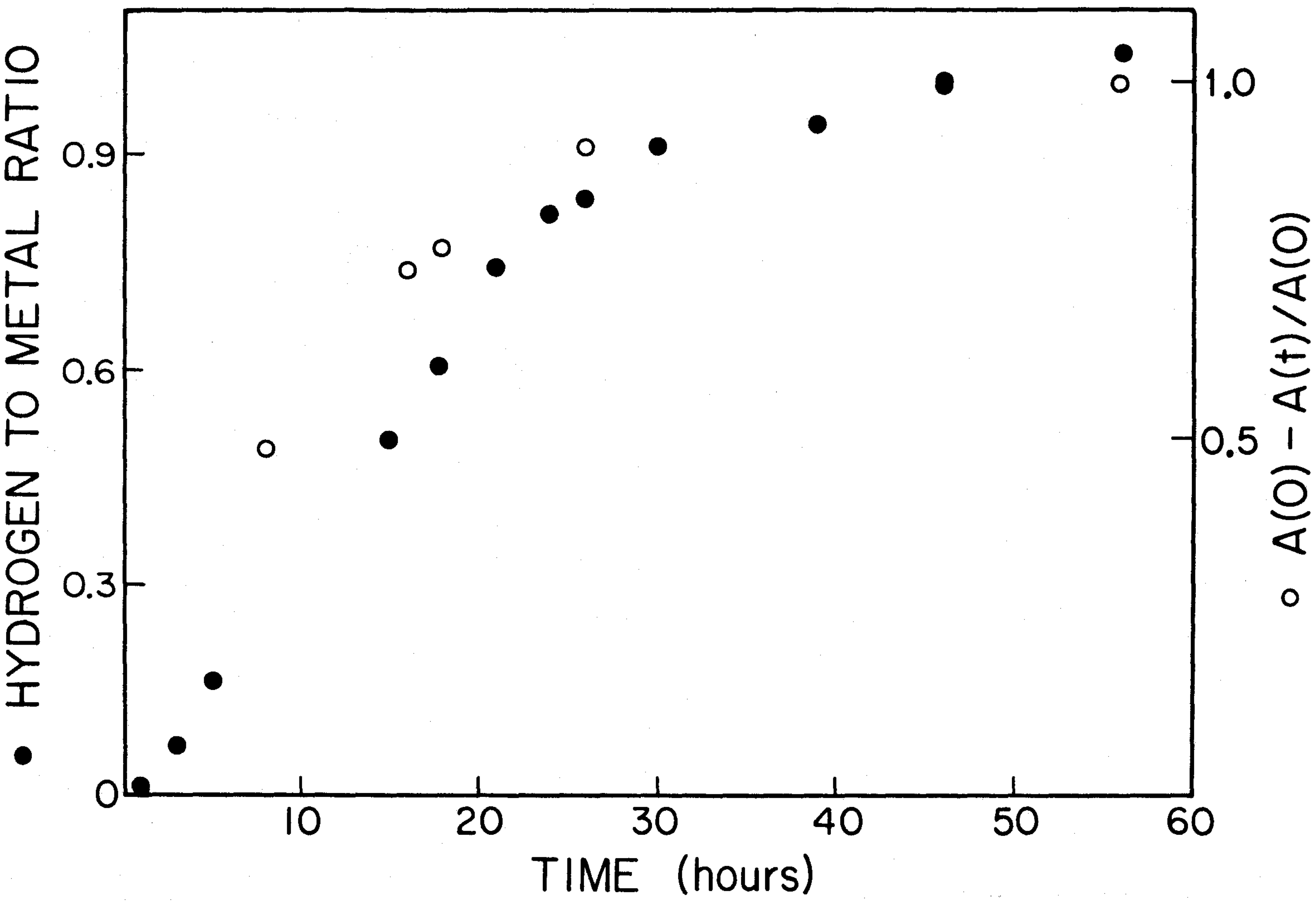

Fig.4.10 Hydrogen to metal ratio (filled circles) and fraction of amorphization (open circles) in $Zr_{0.80}Rh_{0.20}$ plotted as a function of hydriding reaction time.

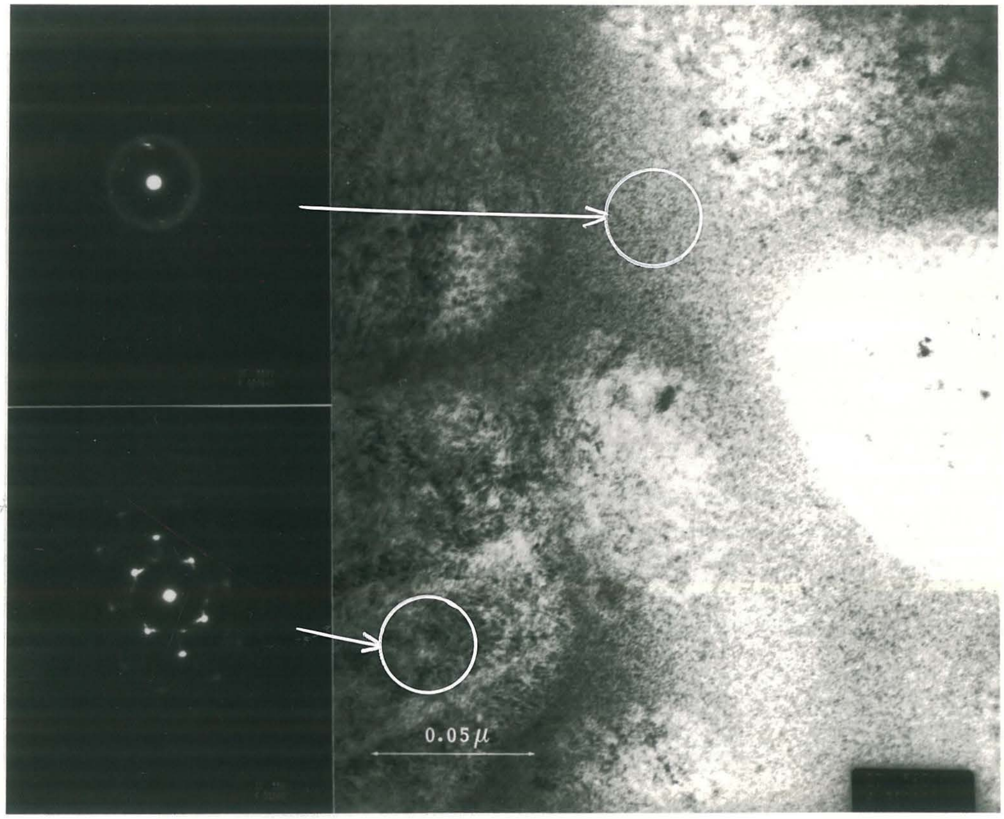

Fig.4.11 TEM micrograph and selected area electron diffraction patterns of partially amorphized $(Zr_{0.80}Rh_{0.20})H_{0.5}$.

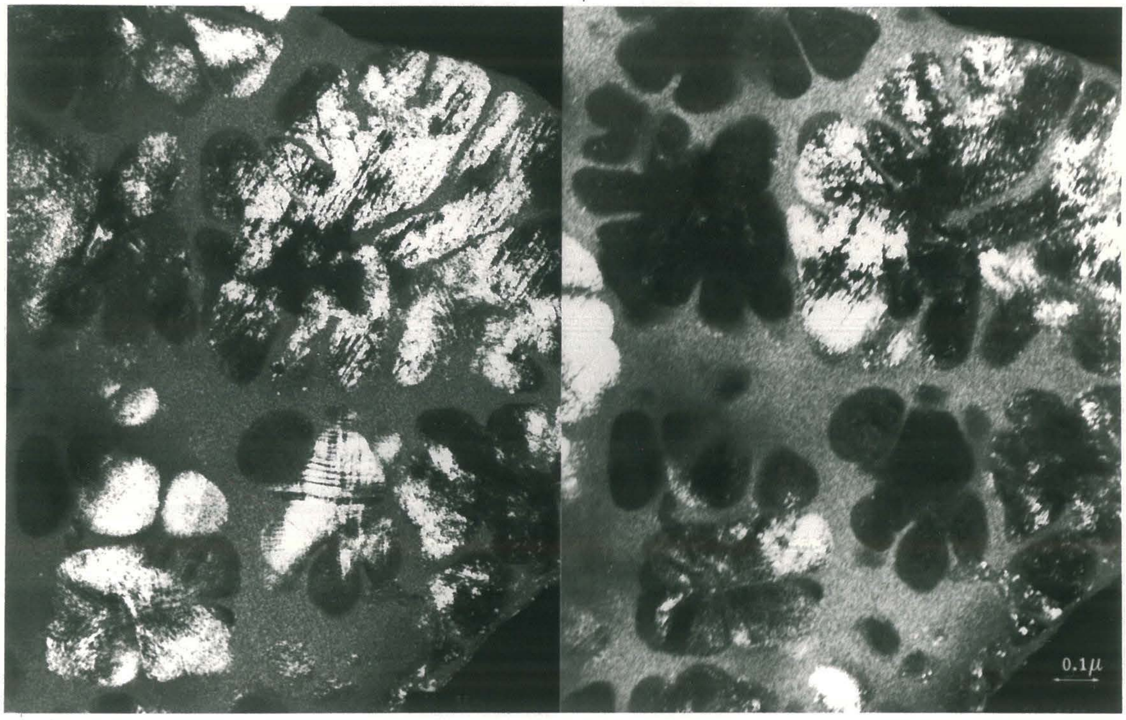

Fig.4.12 Dark field image of partially amorphized $(Zr_{0.85}Rh_{0.15})H_{0.8}$.

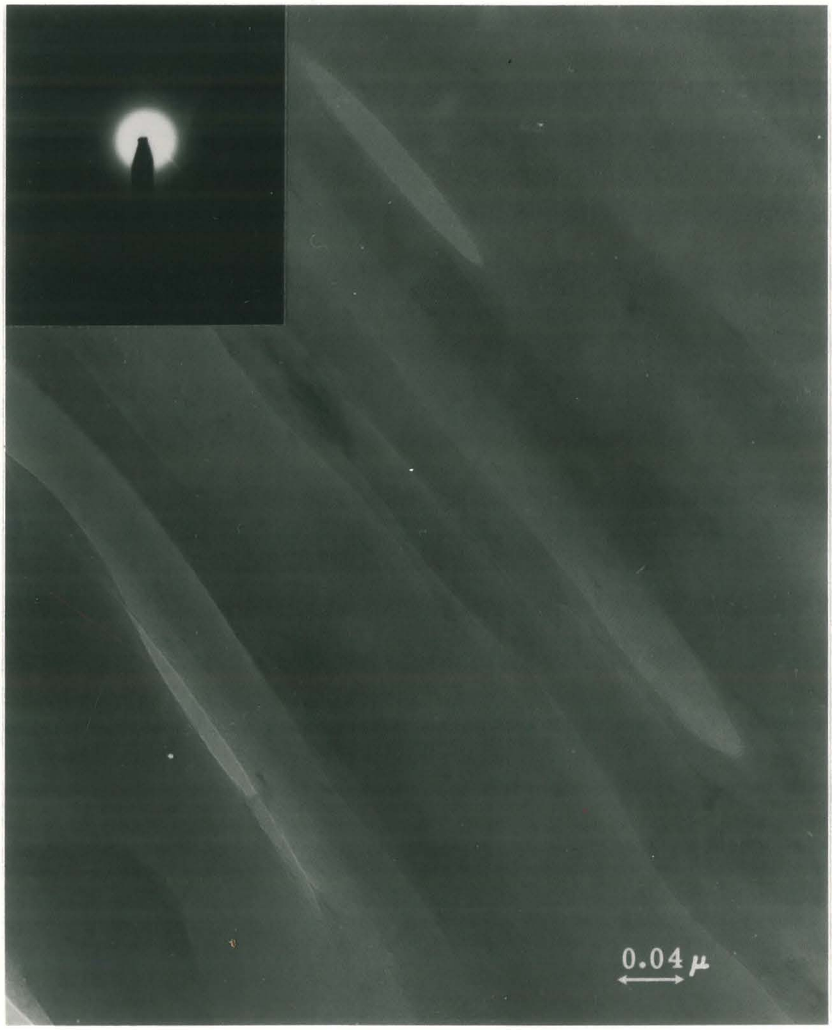

Fig.4.13 TEM micrograph and SAED pattern of fully amorphized $(Zr_{0.80}Rh_{0.20})H_1$

dicated that the local atomic ratio of Zr/Rh was 4.1 ± 0.1 in most regions. A few regions are notable exceptions having a ratio of 3.5. Such regions are apparently associated with the original grain boundary regions before hydriding.

The reduced radial distribution function G(r) was calculated from the X-ray diffraction intensity I(k). The G(r) functions for samples of as-quenched amorphous $\mathrm{Zr_{0.75}Rh_{0.25}}$, hydrided but originally amorphous, and hydrided but originally crystalline $\mathrm{(Zr_{0.75}Rh_{0.25})H_{1.38}}$ are compared in Fig. 4.14. The G(r) function of the two hydrided samples are found to be almost identical. The averaged first neighbor distance of a given atom is represented by the position of the first maximum of G(r) and the coordination number η for the first neighbor shell is the integrated area under the first peak.

A detailed comparison of the positions of various peaks, the atomic coordination numbers η, and the mass densities ρ is given in Table 4.1. All the data for the hydrided samples agree very well within experimental uncertainties. The mass density changes from $7.581 g/cm^3$ for amorphous $\mathrm{Zr_{0.75}Rh_{0.25}}$ to 6.541 g/cm^3 for amorphous $\mathrm{(Zr_{0.75}Rh_{0.25})H_{1.38}}$, a decrease of 13%. This implies that the matrix of transition metal atoms is expanded by $\sim$ 13% upon hydrogen absorption. We also note that the first peak in G(r) for both $\mathrm{(Zr_{0.75}Rh_{0.25})H_{1.38}}$ samples, which is a result of the contribution from the Zr–Rh and Zr–Zr nearest neighbor pairs, shows a resolved splitting, indicating that the originally unresolved Zr–Zr and Zr–Rh distances are now separated. These two corresponding distances are referred to as r_1' and r_1 in Table 4.1. The distances r_1' are nearly the same as the sum of the Goldschmidt radii of Zr and Rh (2.94 Å). On the other hand, the distance r_1 is nearly the same as the nearest neighbor Zr–Zr distance in fcc ZrH (3.37Å) and/or tetrag-

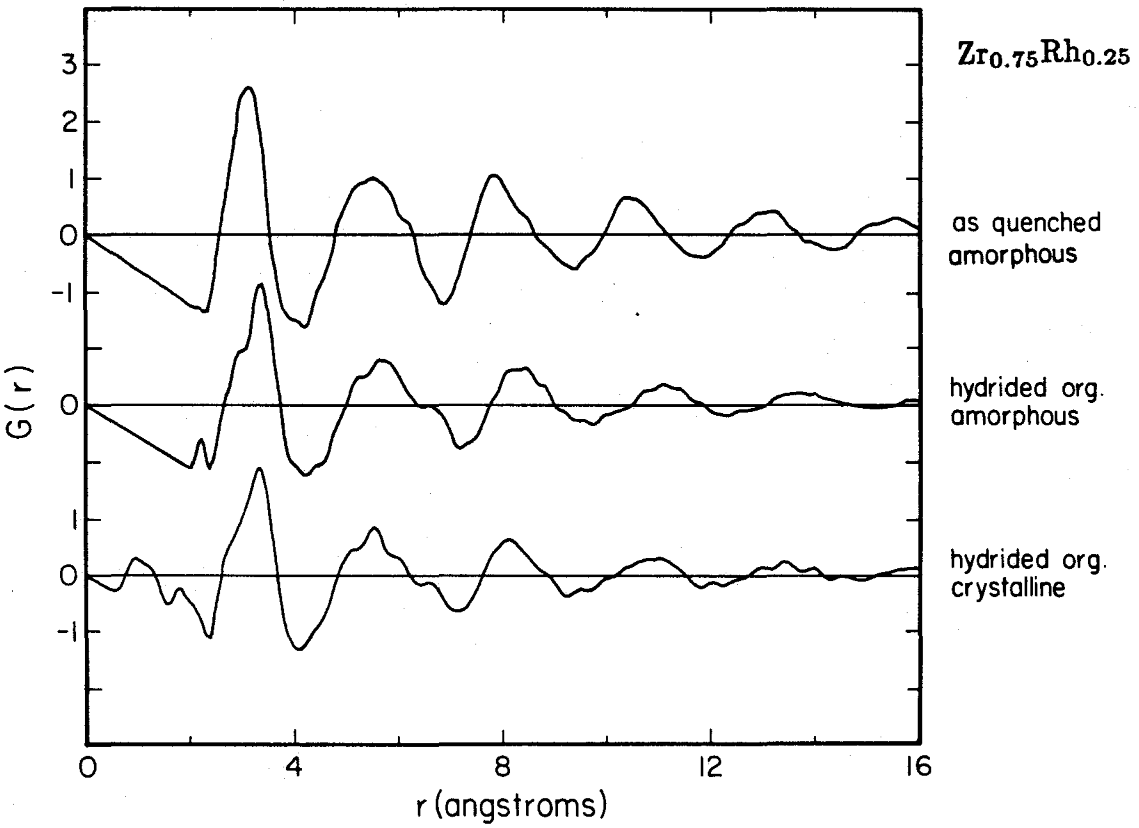

Fig.4.14 The reduced radial distribution functions $G(r) = 4\pi r(\rho(r) - \rho_o)$ for as-quenched amorphous $Zr_{0.75}Rh_{0.25}$, hydrided originally amorphous $(Zr_{0.75}Rh_{0.25})H_{1.38}$ and hydrided originally crystalline $(Zr_{0.75}Rh_{0.25})H_{1.38}$.

	r_1' [Å]	r_1 [Å]	$\frac{r_2'}{r_1}$	$\frac{r_2}{r_1}$	r_3/r_1	r_4/r_1	η	ρ [g/cm^3]	T_c [K]	ΔT_c [$^*10^{-3}$K]	c^* [$\frac{H}{M}$]
as quenched amorphous	—	3.14	—	1.75	1.98	2.51	13.57	7.58	4.40	23	—
hydrided org. amorphous	2.93	3.35	1.78	1.68	1.96	2.47	12.72	6.54	1.16-1.26	~100	1.38
hydrided org. crystal.	2.90	3.33	1.79	1.66	1.98	2.44	12.89	6.53	1.03	75	~1.5

* equilibrium H content at pressure of 1 atmosphere (H_2) and T = 180C

Table 4.1 Experimental data of the as quenched, hydrided originally amorphous and hydrided originally crystalline $Zr_{0.75}Rh_{0.25}$ samples.

onally distorted δ-ZrH_2 (3.3–3.49Å) [4.8]. Evidently, the Zr–Rh distance remains constant while the Zr–Zr distance increases upon hydriding. In crystalline ZrH and ZrH_2, hydrogen occupies tetrahedral interstitial sites. The present evidence and results of other studies of Zr-based glassy metal hydrides suggest that hydrogen preferentially occupies tetrahedral sites defined by four neighboring Zr atoms [4.9, 4.10]. The increase of Zr–Zr distance is responsible for the expansion of the metal matrix in amorphous Zr–Rh hydrides as hydrogen occupies these sites.

The superconducting transition temperatures (T_c) of as-quenched fcc and amorphous $Zr_{0.75}Rh_{0.25}$ and the hydrided samples were measured using a standard AC bridge technique. Samples used for this measurement were placed in a small copper coil which forms one arm of the AC induction bridge. When the temperature is lowered, an increase of the inductance can be detected if the sample becomes superconducting (the Meissner effect). The T_c was taken to be the temperature at which half of total change in the inductance occurs. The width of the transition was usually several hundredths of a degree.

The results of the T_c measurements are also summarized in Table 4.1. The superconducting transition temperature T_c drops from 4.7 K (not shown in Table 4.1) to 1.03 K for the initially fcc $Zr_{0.75}Rh_{0.25}$ upon hydriding and from 4.4 K to 1.16–1.26 K for the initially amorphous sample. The two amorphous hydrides have nearly the same T_c. From these observations, we conclude that hydrogen substantially lowers the T_c in these alloys. This observation is consistent with the results of the measurement of the electronic density of states at the Fermi level $D(E_f)$ obtained by K. Samwer et al.. By measuring low temperature specific heat, they found that $D(E_f)$ is reduced from 2.43 states/eV-atom for as- quenched glassy $Zr_{0.75}Rh_{0.25}$

to 0.54 states/eV-atom for the corresponding hydride $Zr_{0.75}Rh_{0.25}H_{1.38}$. They also obtained $D(E_f)$ =0.58 states/eV-atom for amorphous $Zr_{0.75}Rh_{0.25}H_{1.38}$ which was initially crystalline [4.11].

An attempt was made to reversibly desorb hydrogen from the amorphous $Zr_{0.75}Rh_{0.25}H_{1.38}$ (which has an fcc structure initially) by placing the hydrided samples in high vacuum ($\sim 10^{-6}$ torr) and reheating to $180°C$. A fraction of the hydrogen was desorbed by this treatment. More interestingly, a partial crystallization of the sample was observed resulting in the formation of an fcc $ZrH_{\sim 2}$ phase with lattice parameter a=4.77Å. The X-ray diffraction pattern of the sample shows both an amorphous band and a series of broad Bragg peaks arising from the crystalline $ZrH_{\sim 2}$ fcc phase. Using the observed widths of the Bragg peaks and the Scherrer formula [4.12], we estimate the grain size of the $ZrH_{\sim 2}$ crystallites to be 45$\AA$. The X-ray pattern of this sample is compared with that of an as-quenched amorphous $Zr_{0.75}Rh_{0.25}$ in Fig. 4.15a. The X-ray pattern from the as- quenched amorphous sample agrees very well with that from the amorphous phase of the dehydrided sample.

4.1.4 Interpretation

It is not the intent of this section to give a detailed discussion of the thermodynamic and kinetic aspects of the crystal to amorphous transformation, a topic which is reserved for Chapter V. However, we will provide some phenomenological explanation of the present results of X-ray diffraction and TEM in this section.

The crystal-to-amorphous transformation through hydriding can be compared to a melting process. In fact, it can be thought of as melting in the solid state.

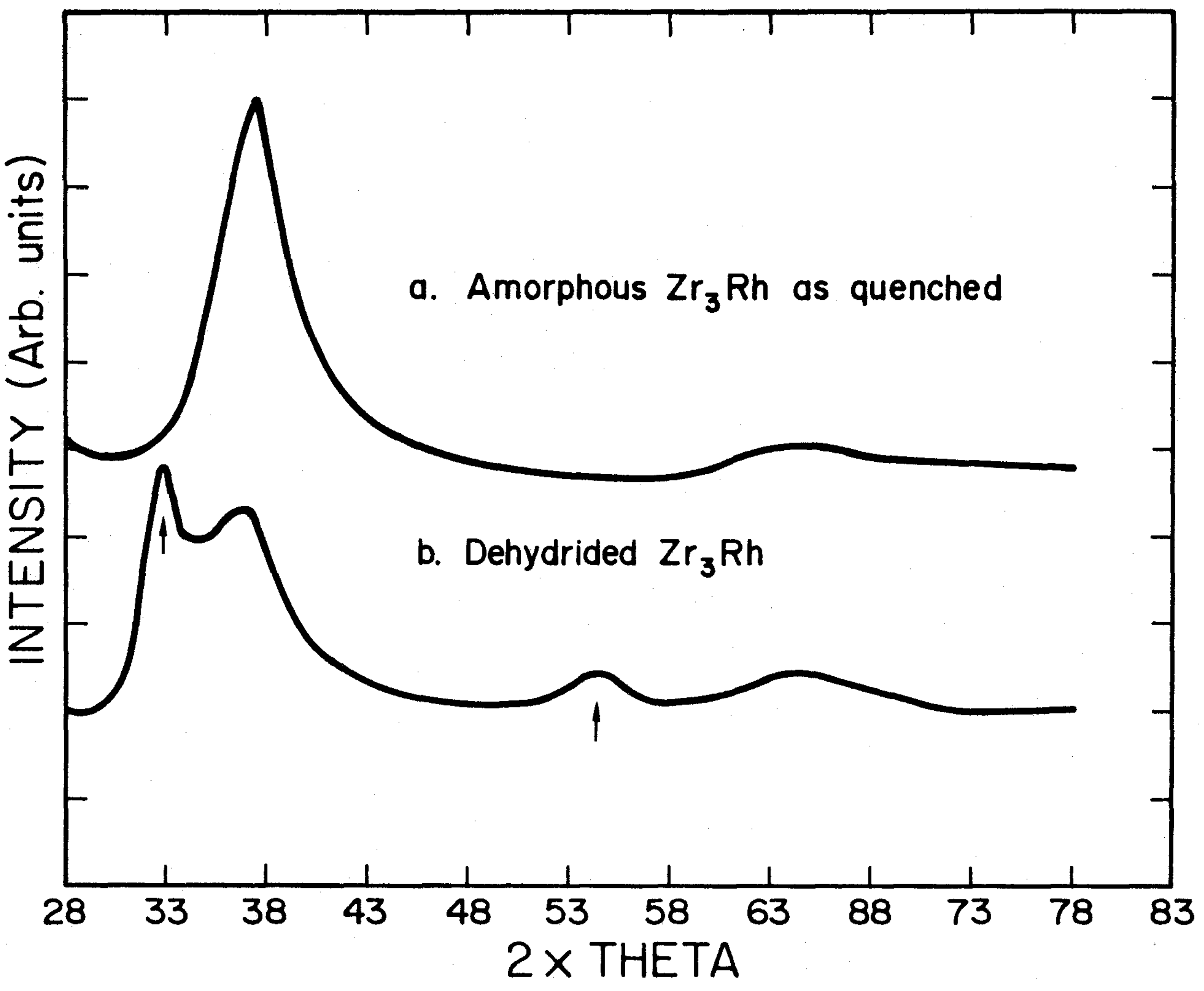

Fig.4.15 X-ray diffraction patterns of (a) as-quenched glassy $Zr_{0.75}Rh_{0.25}$ and (b) dehydrided $Zr_{0.75}Rh_{0.25}$. The arrows indicate the fcc-ZrH_2 phase.

The experiments have shown that the metastable fcc phase does not form a coherent hydride above a critical hydogen concentration, but rather transforms into an amorphous phase or a two phase mixture of $ZrH+Zr_2RhH_y$ if the temperature is high enough. In other words, the fcc crystal becomes superheated with respect to the amorphous phase (the free energy of the fcc phase exceeds that of the amorphous phase) upon hydriding, thus inducing solid state amorphization. The amorphous phase forms and grows, beginning at grain boundaries of the crystalline phase, and proceeding by advance of the amorphous front to the crystal interior. This is exactly what one would expect to see in a melting process. It has generally been accepted that free surfaces and grain boundaries are catalytic sites for heterogeneous nucleation of melting. In fact, a crystal must be slightly superheated for melting to occur. It is interesting to note that phase transformations which involve the conversion of crystalline phases into more disordered forms all tend to have the same morphology as melting [4.13]. The other known examples in this category are disordering of surperlattices [4.14] and irradiation induced amorphization [4.15].

It is well known that once a hydrogen atom occupies a given interstitial site, then this site expands. The strain field affects the nearby interstitial sites such that other hydrogen atoms are (energetically) more likely to stay in the nearby sites. It is also known that hydrogen atoms prefer to reside near macroscopic voids and dislocations. We thus speculate that the grain boundaries can accommodate more hydrogen atoms than other regions, since there are more macroscopic voids and dislocations near grain boundaries. Therefore, there will tend to be larger local strains near the grain boundaries where hydrogen causes lattice expansion. The heterogeneous amorphization is possibly triggered by this strain energy.

§4.2 THERMAL ANALYSIS

The present section describes an attempt to study the thermodynamics and kinetics of the crystal-to-amorphous transformation in metastable fcc Zr–Rh and Zr–Pd solid solutions during the hydriding process using differential scanning calorimetry (DSC). The crystallization behavior of amorphous hydrides produced by hydriding as-quenched amorphous alloys was compared to that of amorphous hydrides by hydriding metastable fcc solid solutions of similar compositions. The thermal stability of these alloys as a function of hydrogen-to-metal ratio was also investigated [4.16].

4.2.1 Differential Scanning Calorimetry Measurements

The relative thermal stability of as-quenched amorphous $Zr_{0.8}Rh_{0.2}$, metastable fcc $Zr_{0.81}Rh_{0.19}$ and their respective hydrides was examined utilizing DSC. The samples were heated at a constant rate (generally 20 K/min.) from 350 K to 870 K. The resultant rate of heat flow into each sample is displayed as a function of temperature in Fig. 4.16 . As verified by X-ray diffraction, amorphous $Zr_{0.80}Rh_{0.20}$ crystallizes into a metastable phase near 690 K (as indicated by the first exothermic peak), and then transforms into the equilibrium phase mixture Zr+Zr_2Rh around 780 K (the second exothermic peak). This crystallization behavior is similar to that of some amorphous $Zr_{0.75}Rh_{0.25}$ samples as reported by Wagner et al. [4.17]. The as-quenched fcc $Zr_{0.81}Rh_{0.19}$ displays greater thermal stability, transforming into the same equilibrium phase mixture of Zr and Zr_2Rh at $T \approx 800K$. (The wheel side of this sample has a trace amount of amorphous phase in coexistence with the crystalline phase, as indicated by X-ray diffraction. The small exothermic peak near 660 K in the DSC scan corresponds to the crystallization of this amorphous

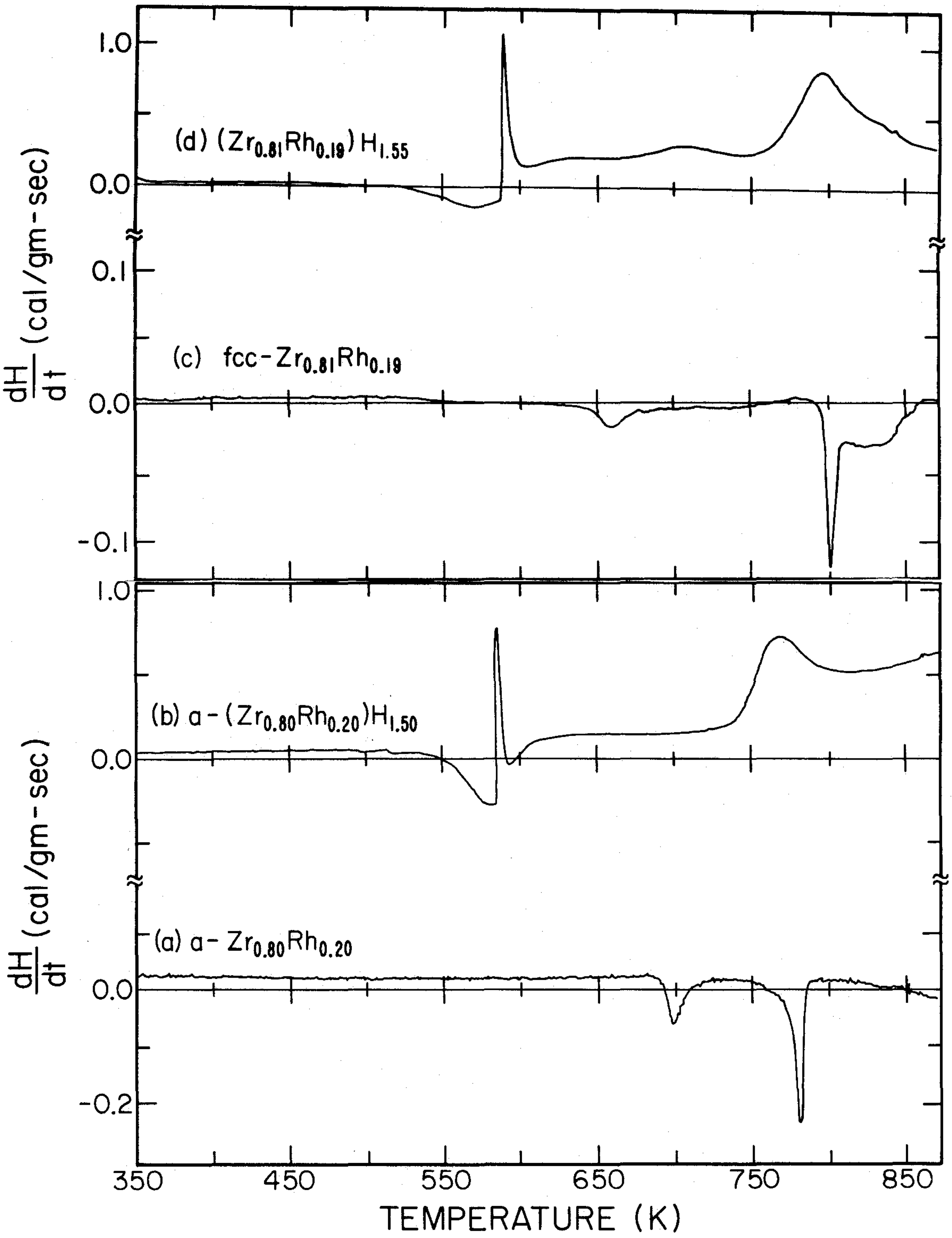

Fig.4.16 DSC scans (with heating rate 20 K/min.) of (a) As-quenched amorphous $Zr_{0.80}Rh_{0.20}$. (b) Amorphous $(Zr_{0.80}Rh_{0.20})H_{1.50}$ produced by hydriding the as-quenched sample at 180°C for 6 days. (c) Polycrystalline fcc $Zr_{0.81}Rh_{0.19}$. (d) Amorphous $(Zr_{0.81}Rh_{0.19})H_{1.55}$ produced by hydriding the as-quenched fcc sample at 180°C for 6 days.

material into the metastable fcc phase.)

The DSC scans of $Zr_{0.80}Rh_{0.20}H_{1.5}$ and $Zr_{0.81}Rh_{0.19}H_{1.55}$ obtained by hydriding originally amorphous and originally fcc samples respectively (as shown in Figs. 4.16 b and d) are essentially identical. Both samples crystallize into $ZrH_x+Zr_2RhH_y$ near $T \approx 575K$. This indicates that the amorphous hydride produced from an originally crystalline sample has similar thermal stability as the sample which was amorphous before hydriding. This is consistent with the X-ray diffraction results, which have shown that the amorphous hydride produced through the solid state reaction with crystalline material is indistinguishable from that produced by hydriding an intially glassy sample of the same composition (see §4.1). The DSC scans of these hydrided samples show that the crystallization peak appears at a temperature of 590 K. This is much lower than that of the unhydrided amorphous sample. This implies that the thermal stability of the amorphous phase against crystallization decreases upon increasing hydrogen content.

The formation of an amorphous phase during hydriding of the Zr–Pd alloy system has also been studied utilizing DSC. Fig. 4.17 shows the DSC scans of the as-quenched metastable fcc $Zr_{0.82}Pd_{0.18}$ and its amorphous hydride $(Zr_{0.82}Pd_{0.18})H_{1.58}$ produced by hydriding the as-quenched sample at $190°C$ for 6 days. (As the aluminum pans are not suitable for heating above 870 K, the heating rate for the as-quenched sample is chosen to be 5 K-sec^{-1} in order to better resolve the exothermic peak.) The crystallization peak for amorphous $Zr_{0.82}Pd_{0.18}H_{1.58}$ appears to be very broad, suggesting that the amorphous hydride phase is inhomogeneous. Since the information which can be obtained from the Zr–Pd and Zr–Rh systems is essentially the same, we have focussed attention on the latter system.

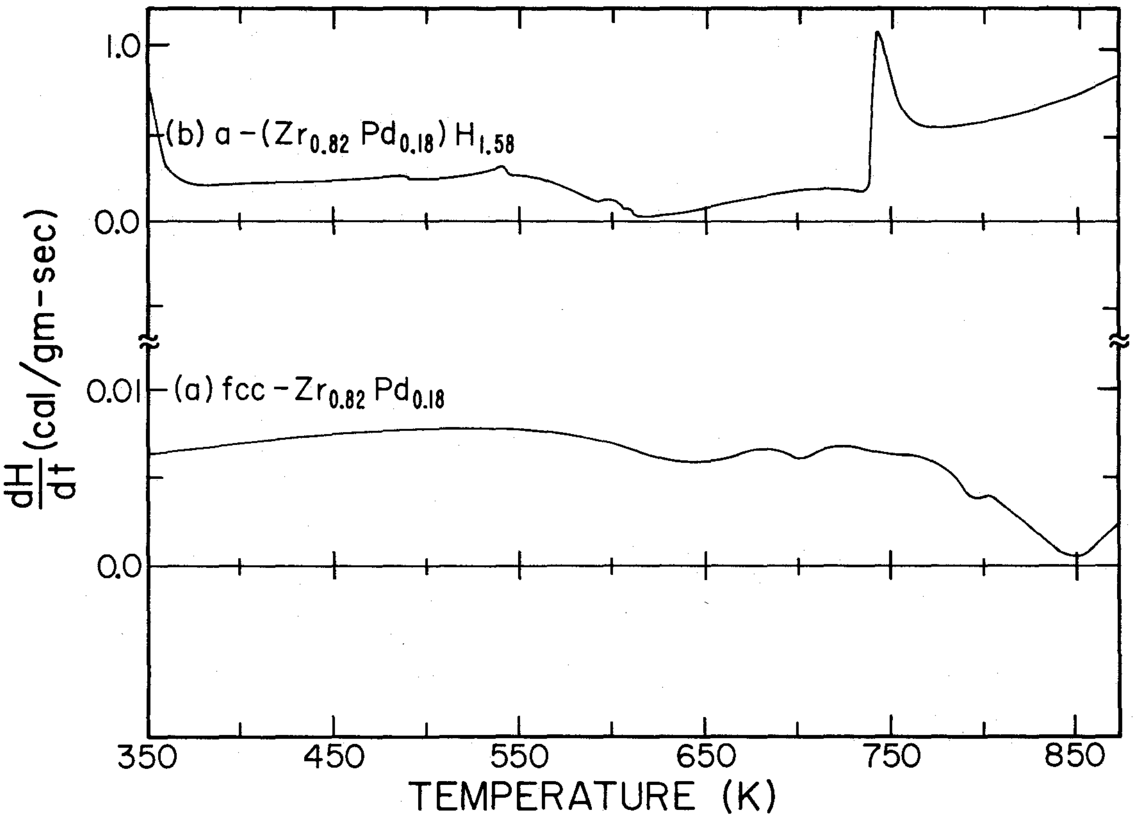

Fig.4.17 DSC scans of (a) polycrystalline fcc $Zr_{0.82}Pd_{0.18}$ and (b) its amorphous hydride $(Zr_{0.82}Pd_{0.18})H_{1.50}$.

The thermal stability of the original single phase fcc $Zr_{0.82}Rh_{0.18}$ and fcc $Zr_{0.81}Rh_{0.19}$ was studied at various stages of the hydriding reaction; the corresponding DSC traces for samples with various hydrogen to metal ratios are shown in Fig. 4.18a–c and in Fig.4.19. The exothermic peak for the as-quenched fcc $Zr_{0.82}Rh_{0.18}$ occurred at a higher temperature ($\sim 840K$) than that for the as-quenched fcc $Zr_{0.81}Rh_{0.19}$ ($\sim 800K$). This suggests that the fcc solid solution with a higher Zr concentration is thermally more stable (cf. Fig. 4.18a and 4.19a). This exothermic peak shifted to lower temperatures as the samples were partially hydrided (see Fig. 4.18b, 4.19b and c). The results of X-ray diffraction measurement show that the fcc phase absorbs hydrogen and transforms into an amorphous phase as the hydrogen concentration increases. Thus, the observation of a decrease of the transformation temperature for the fcc phase to the equilibrium phase mixture upon hydriding indicates that the stability of the hydrided fcc phase against the phase separation decreases with increasing hydrogen concentration in the fcc phase.

The progressive growth of the amorphous phase during hydriding was also detected by the DSC measurements, as indicated by the increase of the area of the crystallization peak in both Fig. 4.18 and Fig. 4.19. The area, which is proportional to the total enthalpy of transformation, is a direct measure of the total fraction of amorphous material in the sample. We also observe a substantial decrease of the crystallization temperature of the amorphous phase with increasing hydrogen concentration: the crystallization occurred near 600 K for $Zr_{0.82}Rh_{0.18}H_{0.8}$ (Fig. 4.18b) and decreased to 550 K for $Zr_{0.82}Rh_{0.18}H_{1.5}$ (Fig. 4.18c).

The enthalpies of observed transformations (equal to the enthalpy difference between the initial phase and the equilibrium phase) were calculated via integration.

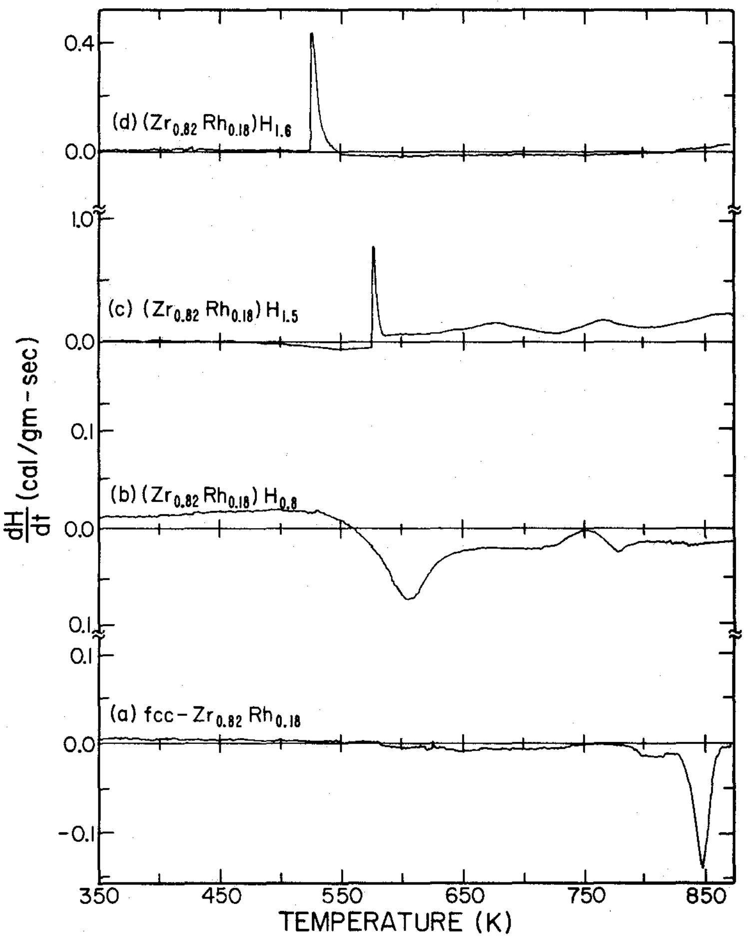

Fig.4.18 DSC scans of $(Zr_{0.82}Rh_{0.18})H_y$ as a function of hydrogen to metal ratio y. (a) Polycrystalline fcc $Zr_{0.82}Rh_{0.18}$. (2) partially amorphous $(Zr_{0.82}Rh_{0.18})H_{0.8}$. (c) amorphous $(Zr_{0.82}Rh_{0.18})H_{1.50}$. (d) Phase mixture of (amorphous+ crystalline ZrH_2) of composition $(Zr_{0.82}Rh_{0.18})H_{1.6}$ (this sample was etched in HF solution and then hydrided at $22°C$).

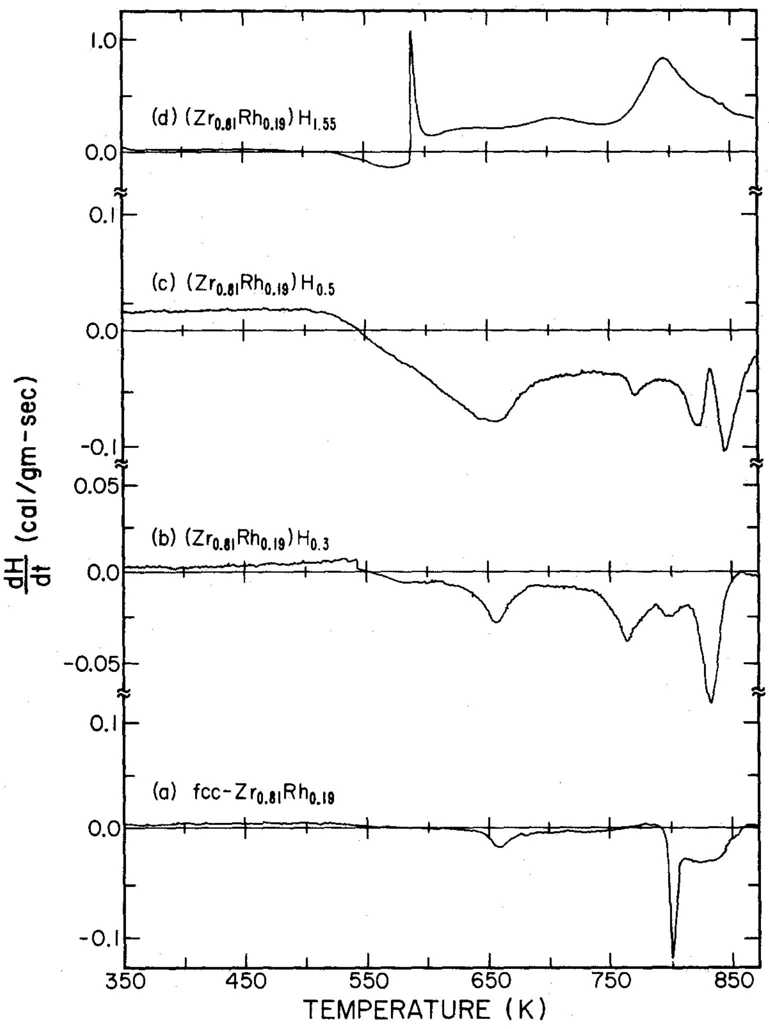

Fig.4.19 DSC scans of $(Zr_{0.81}Rh_{0.19})H_y$ as a function of hydrogen to metal ratio y. (a) Polycrystalline fcc $Zr_{0.81}Rh_{0.19}$. (b) crystalline $(Zr_{0.81}Rh_{0.19})H_{0.3}$ (with a trace amount of amorphous material). (c) partially amorphized $(Zr_{0.81}Rh_{0.19})H_{0.5}$. (d) amorphous $(Zr_{0.81}Rh_{0.19})H_{1.55}$.

The fcc $Zr_{0.81}Rh_{0.19}$, the fcc $Zr_{0.82}Rh_{0.18}$ and the amorphous $Zr_{0.80}Rh_{0.20}$ phases all transform into the same phase mixture (Zr and Zr_2Rh) upon heating. Therefore the enthalpy difference between the fcc and amorphous phases of $Zr_{0.81}Rh_{0.19}$ can be determined. (It is assumed that the amorphous $Zr_{0.80}Rh_{0.20}$ phase has approximately the same enthalpy as the amorphous $Zr_{0.81}Rh_{0.19}$ or the amorphous $Zr_{0.82}Rh_{0.18}$ phase). The enthalpy of transformation for fcc $Zr_{0.81}Rh_{0.19}$ and fcc $Zr_{0.82}Rh_{0.18}$ are the same with experimental accuracy; $\Delta H = 0.7 \pm 0.05$Kcal/mole. The enthalpy of transformation of the fcc $Zr_{0.81}Rh_{0.19}$ phase (0.7±0.05Kcal/mole.) is subtracted from the enthalpy of transformation of the amorphous $Zr_{0.80}Rh_{0.20}$ phase (1.3±0.04Kcal/mole). An enthalpy difference between the fcc and amorphous phases of as-quenched $Zr_{0.81}Rh_{0.19}$ is thus estimated to be 0.6±0.06Kcal/mole.

Zr and Zr-oxide on the sample surfaces can be removed by etching the sample in dilute HF solution. This treatment reduces the surface barrier for hydrogen absorption so that a sample etched in dilute HF solution prior to hydriding reacts completely with hydrogen at room temperature in less than one hour [4.18]. The resulting hydride has a very high hydrogen-to-metal ratio (≥ 1.6). A decrease of sample weight as a function of time was observed as soon as the sample is taken out of the reaction tube, indicating a fraction of hydrogen is evolved from the sample. A precise determination of the actual hydrogen-to-metal ratio is thus very difficult. X-ray diffraction shows the product is a mixture of the amorphous hydride phase and α-ZrH_2 phase. The DSC scan shows that such a hydrided sample has a strong endothermic peak at 525 K, a lower temperature than that observed for the samples hydrided without prior surface etching treatment (see Fig. 4.18d). The details of such surface effects will be discussed in section §4.3.

4.2.2 Interpretation

As mentioned in section §4.1.3, hydrogen atoms in a Zr-based hydride prefer to occupy tightly bonded tetrahedral sites surrounded by four Zr atoms. At the limit of high hydrogen concentration, hydrogen atoms are also found to reside in weakly bonded tetrahedral sites surrounded by three Zr and one Rh (or Pd) atom [4.9, 4.10, 4.19]. The latter configuration is less stable and hydrogen can escape from the 3Zr+Rh sites at a lower temperature than from the 4Zr sites. An endothermic peak is expected in the DSC trace as desorption of hydrogen occurs due to the large increase of configurational entropy that is involved in this process (31 Cal/K-mole as given by ref.4.20). We thus speculate that the low temperature endothermic peak in the DSC scan of hydrides is associated with the escape of hydrogen from the weakly bonded interstitial sites, whereas the high temperature endothermic peak corresponds to the tightly bonded sites. In order to escape from the sample, hydrogen atoms must overcome the sample surface barrier as well as the bonding of the interstitial sites. According to Boltzmann's distribution, the probability of hydrogen atoms having enough energy to jump across the surface barrier is proportional to Nexp$(-E_a/k_BT)$, where N is the number concentration of hydrogen atoms in the sample and E_a is the activation energy which includes the contribution from both the surface barrier and the bonding of interstitial sites. Therefore, the bonding of hydrogen in 3Zr+Rh sites is smaller than that in 4Zr sites, assuming the surface barrier does not vary considerably. Although the probability or jump rate increases with temperature, the total number of hydrogen atoms in the interstitial sites decreases as hydrogen leaves the sample. Therefore an endothermic peak with a maximum at a given temperature is expected. We surmise that the steep leading edge of the low temperature endothermic peak is due to the surface oxide barrier.

As the first hydrogen atoms jump across the surface, the surface barrier is likely to be lowered as the evolving hydrogen causes dilation and cracking of the surface oxide. This creates a path for easier escape of further hydrogen atoms, resulting in the catastrophic evolution of hydrogen and the rather sudden absorption of heat as observed.

Since the probability for hydrogen to jump across the surface at a given temperature increases as the hydrogen concentration N increases and/or as the surface barrier (and E_a) decreases, we observe a decrease of the temperature of the low temperature endothermic peak for both hydrides with greater hydrogen to metal ratio and for those with chemically etched surfaces before hydriding. A plot displayed in Fig. 4.20 shows that the temperature of the first endothermic peak varies in an inverse relation with the hydrogen to metal ratio. We speculate that the following simple explanation may apply. One assumes that the surface barrier can withstand a certain "maximum effective pressure" P_{MAX} of the hydrogen "lattice gas" contained within the sample. On the other hand, using the ideal gas formula P=nRT, one can find an equivalent temperature $T_{endo} = P_{MAX}/(nR)$, where n is the hydrogen concentration. Now P_{MAX} depends on the surface condition and bonding of interstitial sites. One thus expects breakdown of the surface barrier and evolution of hydrogen when this temperature is reached.

Utilizing differential scanning calorimetry we have shown that we can produce amorphous hydrides of relatively good thermal stability by hydriding polycrystalline materials. DSC scans support the contention that amorphous hydrides produced by hydriding polycrystalline samples (fcc $Zr_{1-x}Rh_x$ and fcc $Zr_{1-x}Pd_x$) and by hydriding metallic glasses are similar. The enthalpy difference between fcc Zr–Rh and

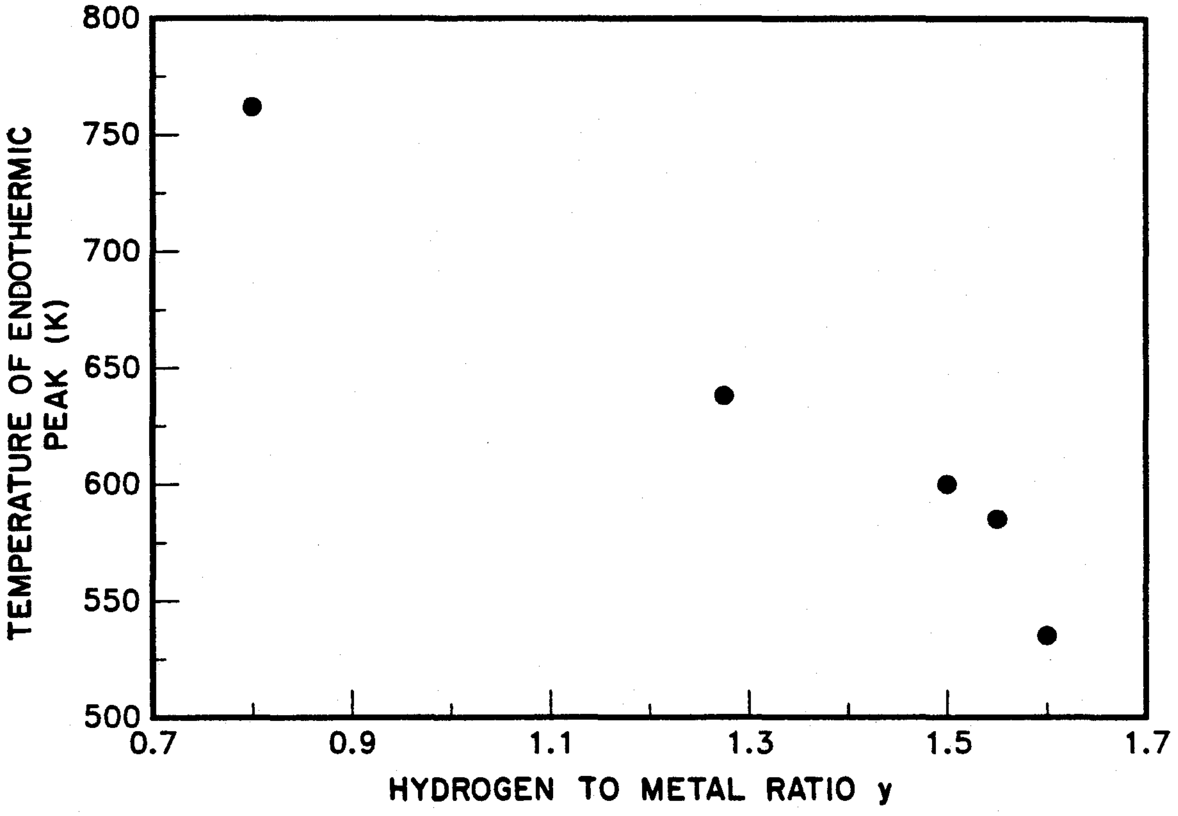

Fig.4.20 The temperature of the first endothermic peak versus hydrogen to metal ratio H/M in amorphous Zr–Rh hydrides.

amorphous Zr– Rh is determined to be 0.6 Kcal/mole. The thermal stability of both the fcc and amorphous phases decreases as the hydrogen to metal ratio increases, upon hydriding. This hydriding process also causes the fcc phase to become unstable with respect to the amorphous phase, whereby the crystal to amorphous transformation occurs.

§4.3 SURFACE EFFECTS AND HYDROGEN DISTRIBUTION

The surface of a sample plays an important role in the hydriding process. If no oxide layer or other surface barriers are present, hydrogen molecules are adsorbed on the sample surface and dissociate into hydrogen atoms. These hydrogen atoms are subsequently absorbed into the outer layers of the bulk sample and finally diffuse into the bulk of the material [4.18]. Each of these processes can potentially be a rate-limiting step for the absorption of hydrogen. In most practical cases, however, the presence of surface oxide layers and/or metal phase separation at the surface makes the situation even more complicated. Various studies have shown [4.18, 4.22] that surface oxide layers passivate the sample surface and act as a barrier against the permeation of hydrogen into the sample. Consequently, the rate of the hydriding reaction is limited by this barrier in most cases.

The present section discusses results of a study of the surface morphology of the glassy $Zr_{0.75}Rh_{0.25}$ after different surface treatments and investigation of the effects of sample surface on the hydriding process in various rapidly quenched Zr–Rh alloys. The surface of as-quenched and hydrided samples is characterized utilizing SEM and Rutherford backscattering. Hydrogen depth profiles at various hydrogen concentrations and with different surface treatments prior to hydriding are measured utilizing resonant nuclear reactions in order to understand the kinetics of the hydrogen absorption process [4.21].

4.3.1 Surface Analysis

The preliminary results of hydriding experiments have provided the following observations: (1) the rapidly quenched $Zr_{1-x}Rh_x$ ($0.15 < x < 0.25$) samples with smaller values of x absorb hydrogen with greater difficulty than the samples with greater values of x. The as-quenched samples with atomic percentage of Zr higher than 80% do not absorb hydrogen unless the samples are mechanically abraded, chemically etched or activated by heating the samples at high temperatures ($350°C$ or higher) under hydrogen atmosphere. (2) At any composition, an increase of hydrogen absorption rate following mechanical abrading is observed. An even more dramatic increase of absorption rate is observed when the sample is etched in 1% HF solution prior to hydriding (to fully hydride a mechanically abraded sample takes at least four days at $180°C$, while it takes less than one hour to fully hydride a chemically etched sample). An observable rise of sample temperature during hydriding can be detected for the chemically etched sample prior to reaction. This indicates that the reaction is so rapid that the large amount of heat generated can no longer be dissapated by thermal contact with the atmosphere and surrounding container. (3) The lowest temperature at which the hydriding reaction can take place is $\sim 150°C$ for mechanically polished samples, whereas the samples chemically etched can react with hydrogen at temperatures as low as $0°C$. All of these prominent features confirm the existence of surface barrier that can be partially removed by surface treatment.

The morphology of the surface of the rapidly quenched $Zr_{0.75}Rh_{0.25}$ samples and their hydrides was investigated utilizing scanning electron microscopy (SEM). The surface of the as-quenched $Zr_{0.75}Rh_{0.25}$ is uniform, smooth and featureless as shown by the SEM mocrograph in Fig. 4.21. This sample was then polished by sanding it with a No.600 Emery paper and is subsequently hydrided at 180°C for four days. Fig. 4.22 shows the SEM micrographs of this sample before and after hydriding. There is no significant change of surface morphology upon hydriding. Both samples show channels of mechanically exposed surface. It is very probable that surface Zr oxide layer formed during rapid quenching is removed by this treatment. This explains why a mechanically abraded sample is easier to hydride.

The surface of a sample etched in dilute HF solution shows mesa-like patterns as shown in Fig. 4.23a. The mesas have an average size about few microns. The lines appearing on the next layer of the sample indicate that etching of the suceeding layers is initiated immediately after disintergration of the original surface layer. The HF solution could preferentially etch away surface Zr and Zr-oxide and thus leave excess Rh on the surface. This would be an advantage for hydriding, because Rh is well-known to be an excellent catalyst for hydriding [4.18]. The sample surface could be further opened by the absorption of a small amount of hydrogen during etching. A SEM micrograph of the etched sample which was hydrided at room temperature for three hours is shown in Fig. 4.23b. One may immediately see that a large fraction of the mesas has disappeared after hydriding. One also notes that the original lines on the surface of the unhydrided sample have developed into microcracks upon hydriding. One may speculate that when the hydriding reaction proceeds very rapidly, the local hydrogen concentration near the surface may be higher than that in the bulk, inducing a large strain near surface. Since the time scale of hydriding is very short, stresses do not have sufficient time to relax. This

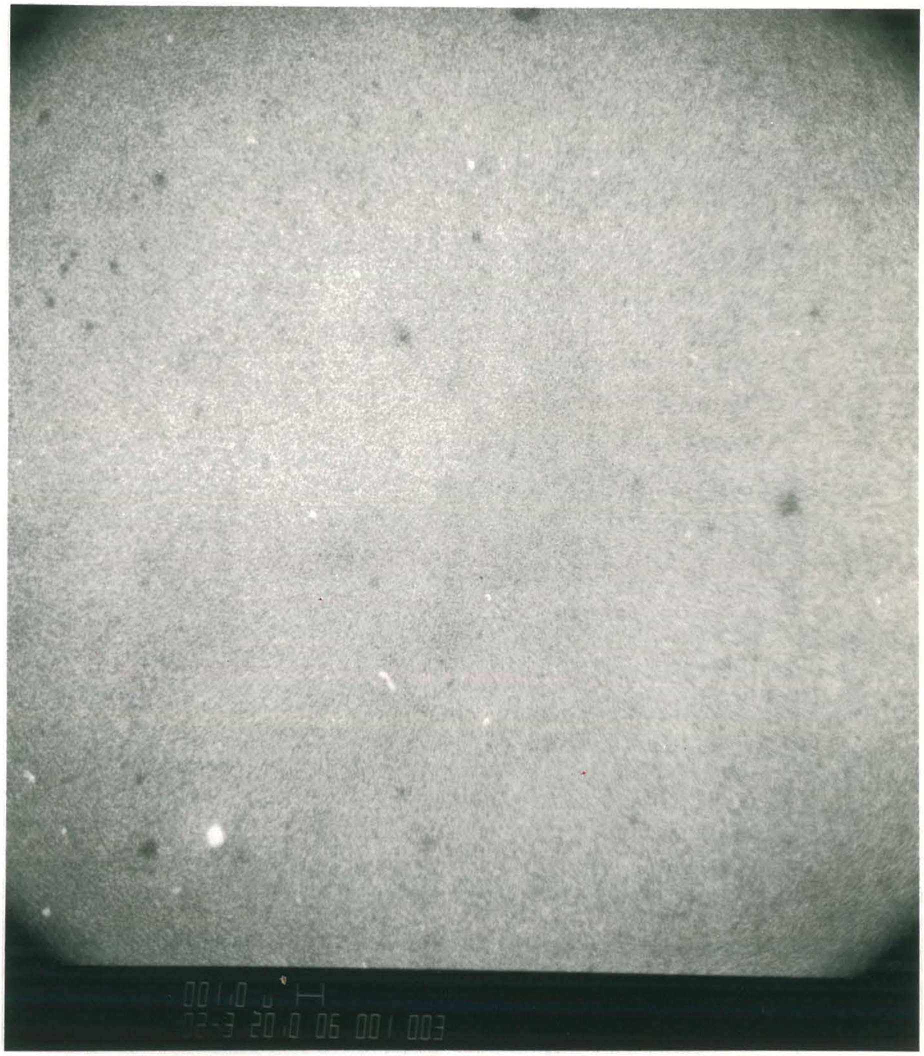

Fig.4.21 SEM micrograph of as-quenched glassy $Zr_{0.75}Rh_{0.25}$ foil.

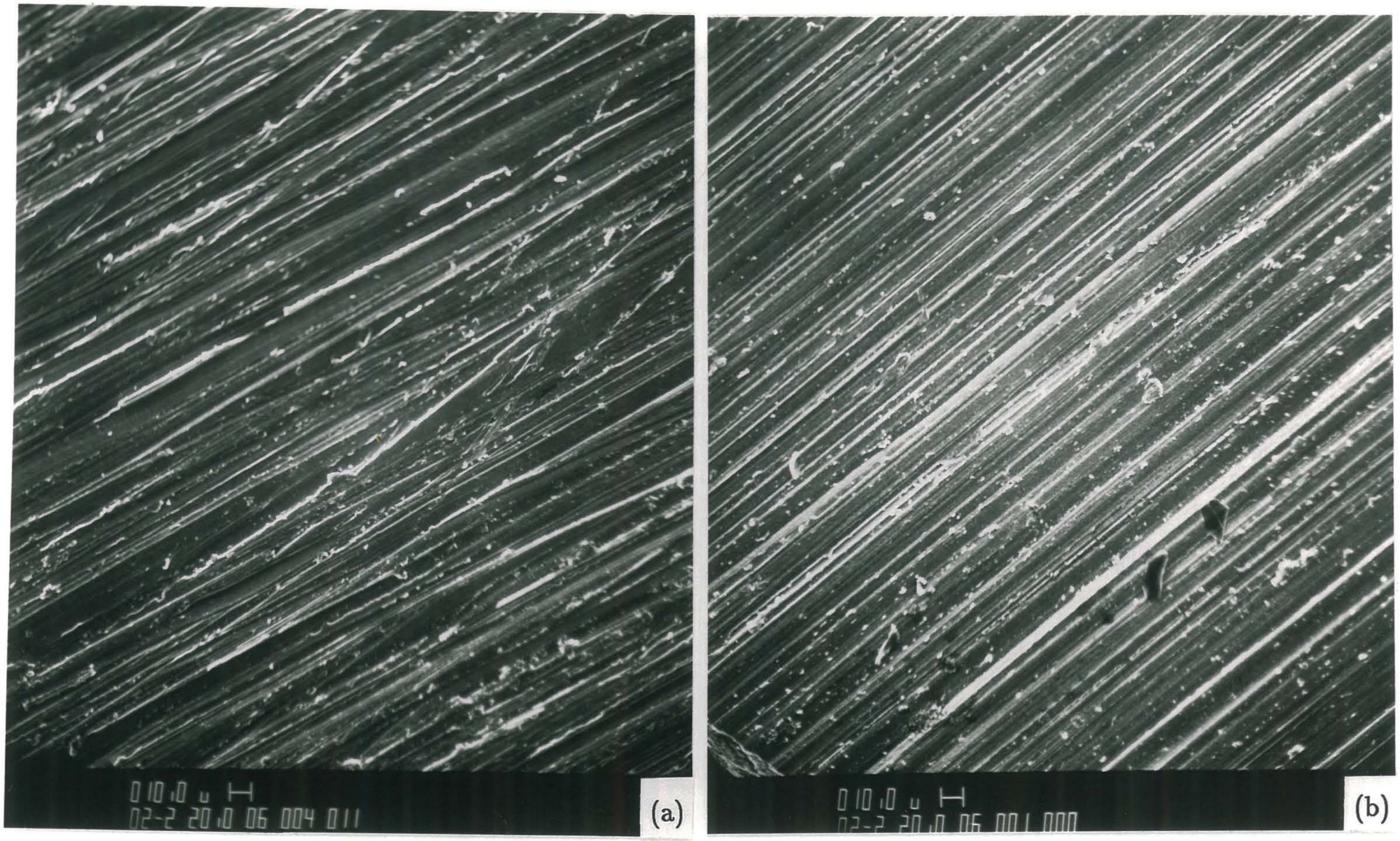

Fig.4.22 SEM micrographs of mechanically abraded glassy $\mathrm{Zr}_{0.75}\mathrm{Rh}_{0.25}$ before (a) and after (b) hydriding at 180°C.

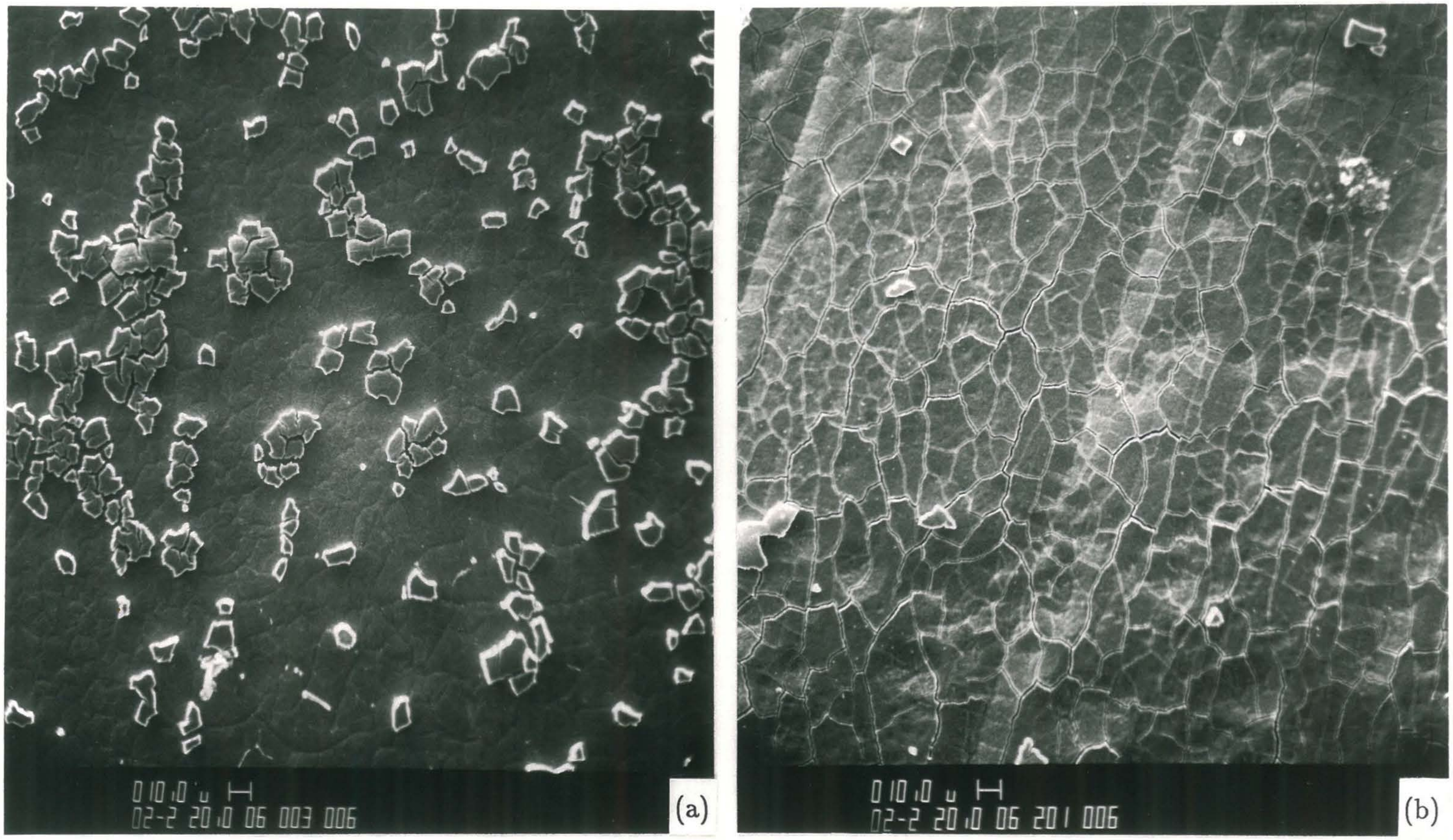

Fig.4.23 SEM micrographs of dilute HF etched glassy $Zr_{0.75}Rh_{0.25}$ before (a) and after (b) hydriding at 23°C for 3 hours.

may result in the microcracks on the surface.

The surface composition of amorphous samples (as-quenched, mechanically abraded and chemically etched) with nominal composition $\mathrm{Zr_{0.77}Rh_{0.23}}$ was studied utilizing Rutherford backscattering spectrometry. In this experiment, a beam of 2 MeV $^4He^+$ ions impinges on the sample in a vacuum chamber of $\sim 10^{-6}$ Torr. The backscattered $^4He^+$ particles are analyzed by plotting the yields of backscattered particles as a function of their energies. The surface composition is determined by the relative intensities of the $^4He^+$ backscattered from Zr and Rh atoms. The atomic ratio of Zr and Rh is given by:

$$\frac{\mathrm{C_{Zr}}}{\mathrm{C_{Rh}}} = \frac{\mathrm{H_{Zr}}/\sigma_{\mathrm{Zr}}}{\mathrm{H_{Rh}}/\sigma_{\mathrm{Rh}}}$$

where H_{Zr} and H_{Rh} are the backscattered $^4He^+$ intensities from surface Zr and Rh, and σ_{Zr} and σ_{Rh} are the scattering cross sections of Zr and Rh, respectively. Thus, the backscattering spectrum provides a direct measure of the surface concentration of individual species (Zr and Rh). The backscattering spectra taken of the as-quenched amorphous $\mathrm{Zr_{0.77}Rh_{0.23}}$ (the crosses) and the same sample etched in dilute HF solution (the open circles) are shown in Fig. 4.24. One can see a relative increase of Rh signal upon chemical etching, indicating a decrease of Zr signal near the surface. This suggests that there is a significant decrease of Zr content at the surface after chemical etching. We found that the surface composition of the as-quenched sample is approximately $Zr_{0.77}Rh_{0.23}$, which is the same as the nominal bulk composition. However, the surface composition of the chemically etched sample is approximately $Zr_{0.24}Rh_{0.86}$. This result supports the assertion that Zr is preferentially etched away by HF solution. One notes that such a Rh-rich surface layer formed during etching is rather weakly bonded, since it can be wiped away with a soft tissue. It must be that a rather porous Rh-rich layer forms

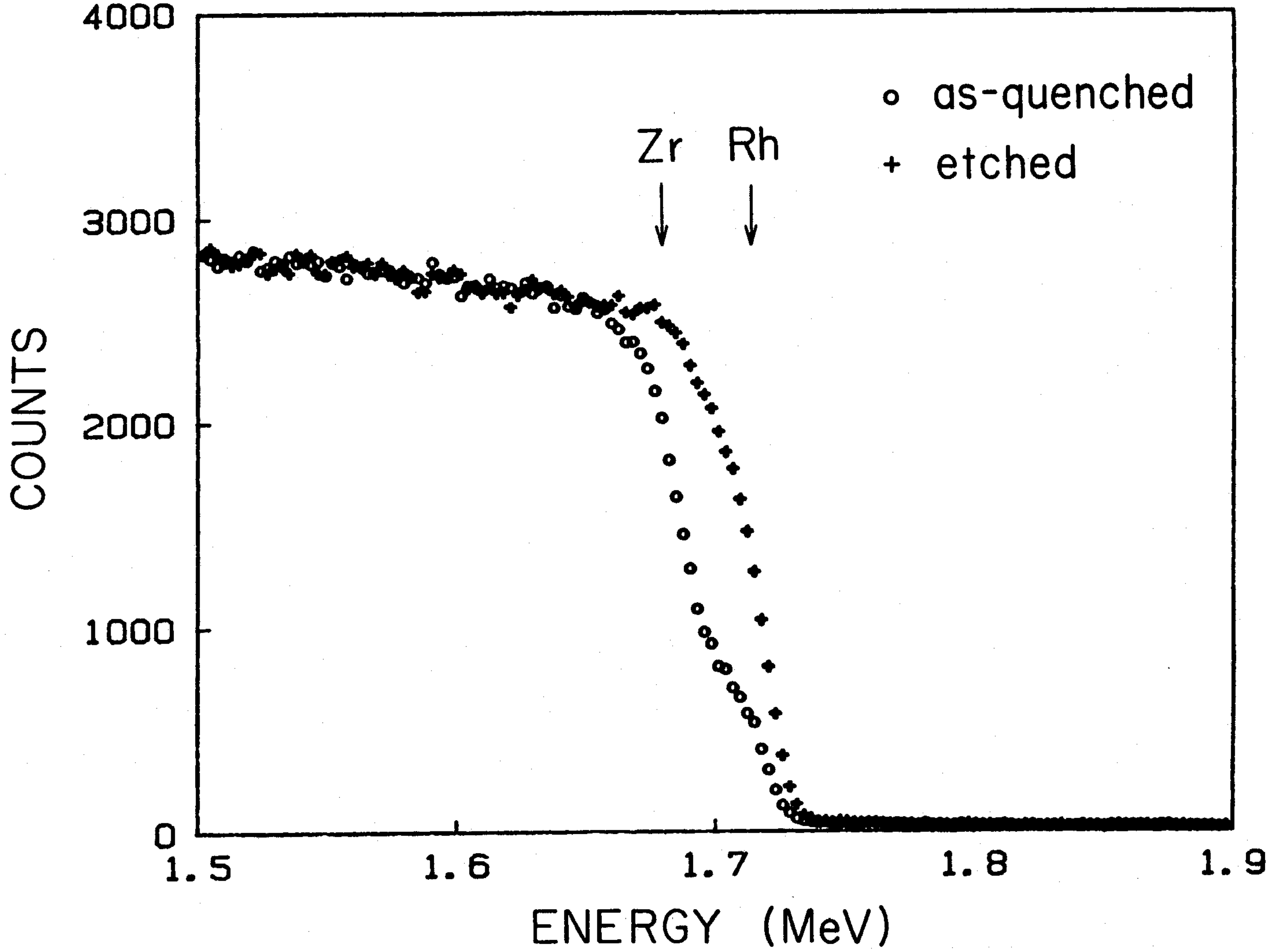

Fig.4.24 Backscattering spectra of a glassy $Zr_{0.77}Rh_{0.23}$ foil. Open circles: the as-quenched sample. Crosses: the HF etched sample.

during etching when a large amount of Zr atoms is removed by the acid. No such compositional change was detected after mechanically abrading the surface.

4.3.2 Hydrogen Depth Profiling

The resonant nulear reaction $^{19}F(^{1}H,\alpha\gamma)^{16}O$ experiment was performed to further study the hydrogen depth profile in the samples. As-quenched amorphous $\mathrm{Zr_{0.75}Rh_{0.25}}$ foils were mechanically abraded and then reacted with hydrogen gas at $180°C$ for various periods of time. Fig. 4.25 shows hydrogen depth profiles in hydrided amorphous $Zr_{0.75}Rh_{0.25}$ at various stages of reaction. The surface peak (which is a result by contamination of H_2 and H_2O on the sample surface) and the background counts were subtracted from these plots. The intensity of the γ-ray signal is proportional to the local hydrogen concentration in the sample. The actual hydrogen-to-metal ratio is determined by comparing the data with that obtained from a tourmaline standard of known hydrogen concentration. We observe that the overall hydrogen concentration in the sample determined with this method agrees very well with the number obtained by measuring the change of hydrogen pressure in situ, indicating that the amount of hydrogen evolving from the sample after it is taken out from the reaction tube is insignificant, unlike the chemically etched sample. The flat plateau in the signal as seen in the figure indicates that the hydrogen has a uniform distribution in the sample during each progressive hydriding step. These observations are consistent with the argument that the time scale for hydrogen redistribution within the sample is much shorter than that for hydrogen permeation through the sample surface. In other words, this observation implies that a surface barrier against hydrogen permeation limits the overall reaction rate.

The same as-quenched $\mathrm{Zr_{0.75}Rh_{0.25}}$ was etched in dilute HF solution and then

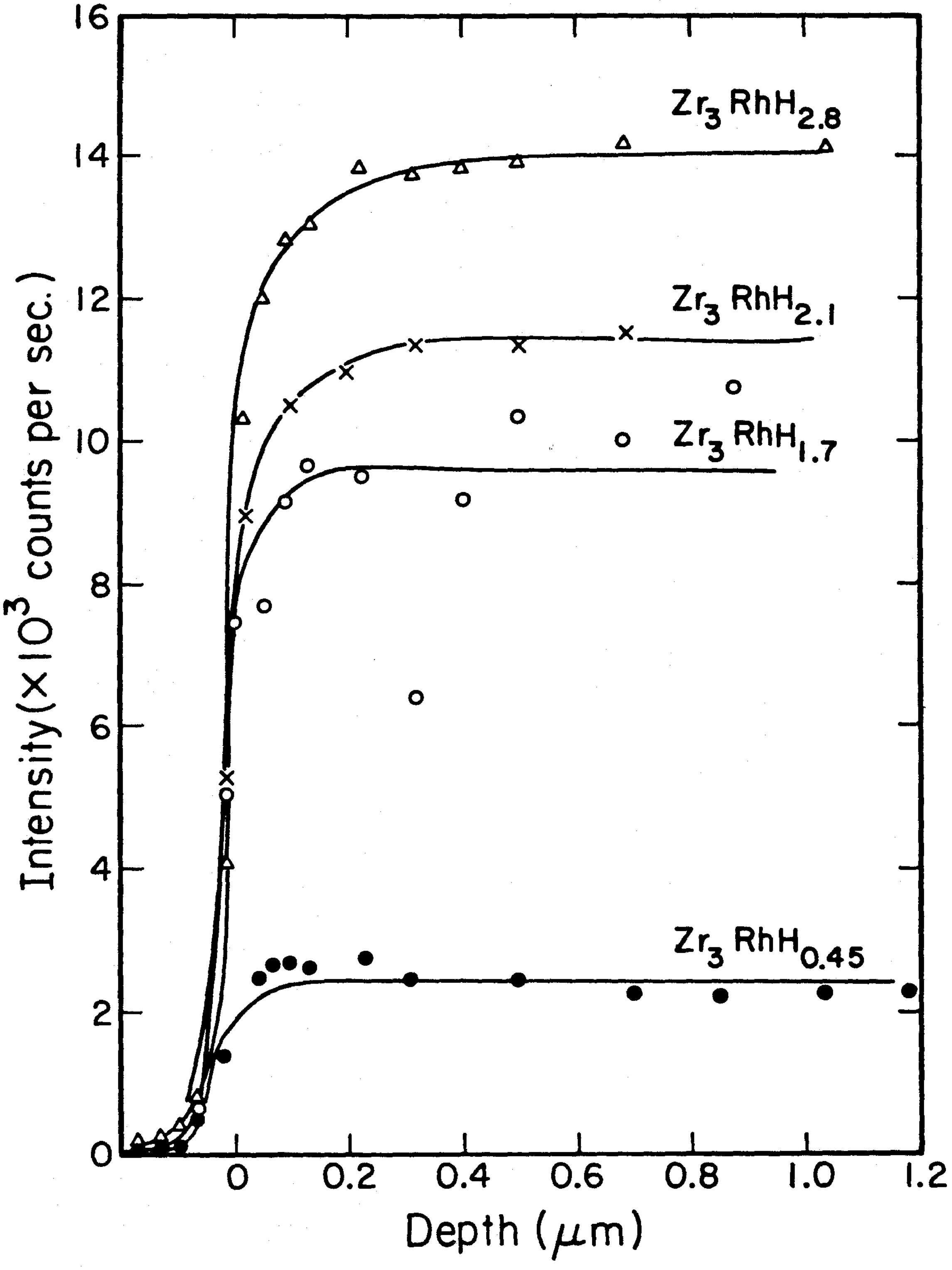

Fig.4.25 Hydrogen concentration profiles in glassy $Zr_{0.75}Rh_{0.25}H_y$ during hydriding at 180°C. The sample was mechanically abraded before hydriding.

reacted with hydrogen gas at 23°C for 1 minute. The hydrgen depth profile of this hydrided sample was measured using the resonant nuclear reaction $^{15}N(^1H, \alpha\gamma)^{12}C$. The measurements of the profile have been repeated several times both at room temperature and at liquid nitrogen temperature (by cooling the sample through a "cold finger"). The results obtained at both temperatures are identical and no time dependence of the profile has been observed. As shown in Fig. 4.26, the hydrogen concentration increases with increasing depth from the sample surface and reaches a plateau near a depth of ~0.7μm. This suggests that the number of available interstitial sites for hydrogen decreases near the surface. This is consistent with the backscattering result that the atomic ratio of Zr/Rh near the surface is lower than in the bulk.

4.3.3 Interpretation

As mentioned earlier, the molecular H_2 gas must dissociate at the surface into 2 H atoms and then remain adsorbed on the surface as a first step of the hydrogen absorption process. (This process is known as dissociative chemisorption). It has been found that hydrogen can easily be dissociatively chemisorbed on Rh [4.23] and Pd atoms [4.24]. Therefore, the hydriding process can be expected to proceed more easily in the presence of excess Rh or Pd on the surface. On the other hand, surface oxide layers suppress the dissociative chemisorption process whereby molecular hydrogen must be activated (i.e., gain enough kinetic energy) in order to both penetrate the surface barrier and dissociate on the metallic surface in an absorption process.

Both mechanical abrading and chemical etching can remove the surface oxide, while in addition the chemical etching also results in a Rh enriched and Zr deficient

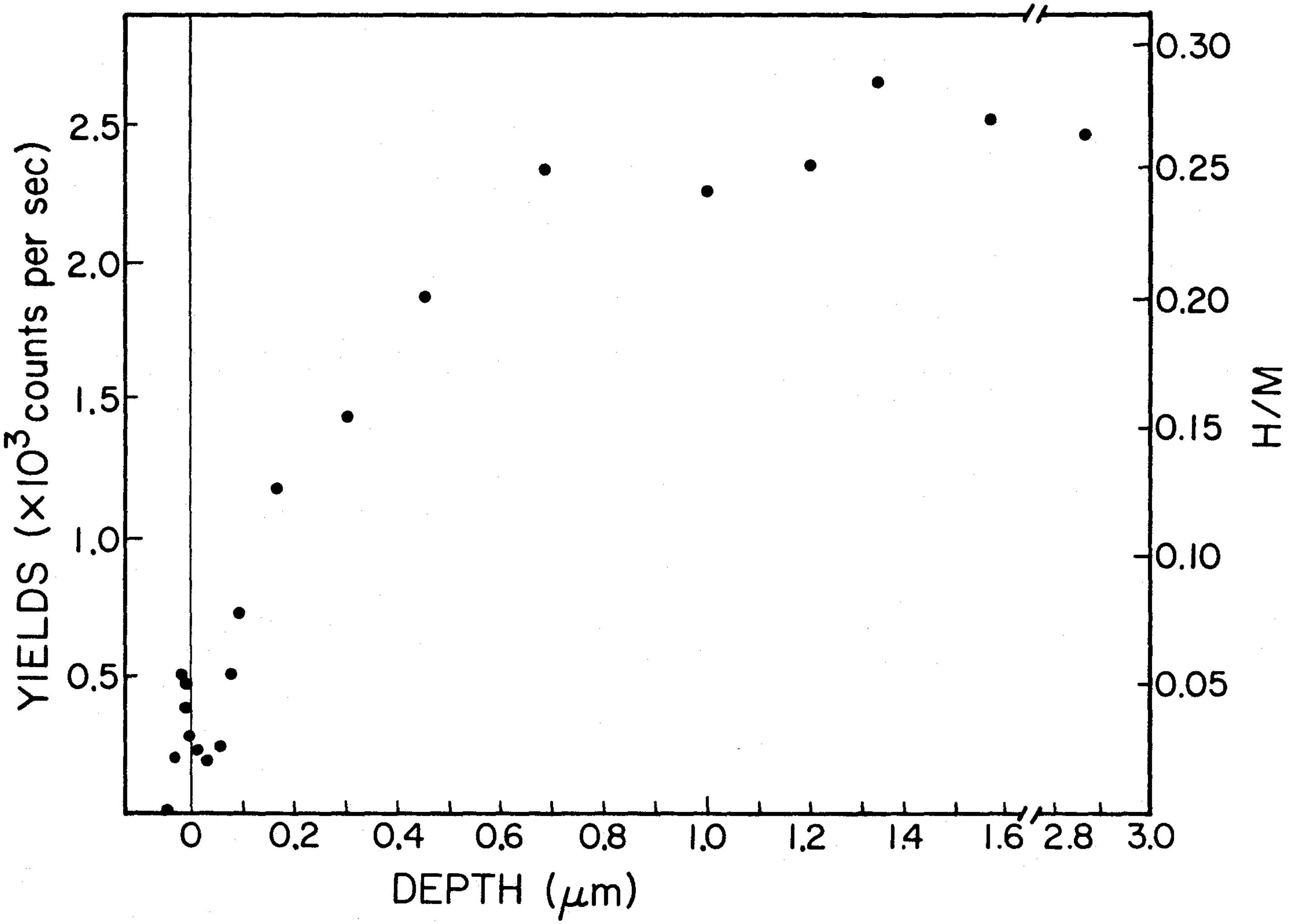

Fig.4.26 Hydrogen concentration profile in a glassy $Zr_{0.75}Rh_{0.25}H_{0.27}$ after it was hydrided at 23°C for 1 minute. This sample was etched in dilute HF before hydriding.

surface region. This apparently explains the drastic increase of absorption rate observed after etching.

As a consequence of chemical etching, the density of the material near the surface is lowered and the number of the Zr-rich tetrahedral sites (4Zr and 3Zr+Rh sites) is reduced near the surface owing to the enhanced Rh concentration. Both of these effects tend to reduce the total available interstitial sites for hydrogen to occupy. This can also explain why the hydrogen concentration decreases near the surface for the hydride which was chemically etched before hydriding.

V. DISCUSSION

The mechanisms of the solid state amorphization reaction upon hydriding in Zr–based metastable fcc systems will be discussed based on the experimental data. The first section addresses the question of why the crystal-to-amorphous transformation is thermodynamically possible, and the second section addresses why a transformation to a crystalline phase or phase mixture with even lower free energy is kinetically forbidden.

§5.1 THERMODYNAMIC ASPECTS

We have already mentioned in chapter 2 and 4 that hydrogen atoms prefer to occupy tetrahedral interstitial sites with as many Zr neighbors as possible in the Zr–late transition metal alloys, owing to the fact that Zr–H has a large negative heat of formation, whereas late transition metal hydrides have positive heats of formation. It is obvious that an alloy with more Zr tetrahedral sites should accomodate more hydrogen than an allotropic structure with less 4Zr tetrahedral sites. Let us call the structure with more 4Zr sites phase I and one with less 4Zr sites phase II. If the following inequality holds, a phase transformation from phase II to phase I may occur in the light of the 2nd law of thermodynamics:

$$\text{Free Energy}(IH_x) < \text{Free energy}(IIH_x)$$

Obviously, this inequality becomes true when the hydrogen to metal ratio x becomes greater. Let us start from an alloy with phase II. If the free energy of the hydrogen free phase II is lower than that of phase I initially, one can increase the hydrogen concentration in the alloy by increasing the chemical potential of the H_2 gas outside the sample to reverse the relative free energy relation of the two phases, thus causing the transformation from phase II to phase I. This is exactly what happens in the crystalline-to-amorphous phase transformation upon hydriding, as we have already demonstrated. We will show next the amorphous phase of a Zr–Rh alloy does indeed have more 4Zr tetrahedral sites than the fcc phase of the same alloy.

According to the DRPHS model, there are 2.9 tetrahedral sites per atom in an ideal metallic glass without counting the distorted tetrahedra obtained by decomposing the more complex Bernal polyhedra. This number exceeds the number of tetrahedral sites of an fcc phase, which has only 2 tetrahedral sites per atom. Since the Zr–Rh (or Zr–Pd) alloy itself has a large negative heat of formation, these alloys will be characterized by an excess of unlike pairs of neighboring atoms (generally known as chemical short-range ordering). On the other hand, we know that the metastable fcc phase forms only if the quenching rate is slow enough that the atoms in the melt have time to arrange themselves on a lattice; thus, the fcc phase would be expected to have a higher chemical short range order than the amorphous phase of the same composition. We speculate that the fcc phase may be partially ordered with the Cu_3Au-type ordering. Consequently, an even greater difference between the number of 4Zr tetrahedral sites in the amorphous phase and that of the fcc phase of same composition might be expected.

Based on the DRPHS model and the Swintendick criterion, Samwer and Johnson proposed a statistical model to predict the maximum hydrogen concentration in an amorphous Zr_xX_{1-x} alloy [33]. In this model they assumed that hydrogen atoms occupy predominantly the 4Zr tetrahedral sites with a minimum separation between hydrogen atoms of 2.1Å (the Switendick criterion). Since larger polyhedra (shown in Fig.2.3b–e) can be broken down into distorted tetrahedra, they obtained the total number of tetrahedra is approximately 5 per atom. Thus, the number of 4Zr sites in a Zr-based amorphous alloy is approximately given by $5x^4$. The calculated number of 4Zr sites per atom as a function of composition along with the experimentally obtained maximum H/M ratios for various hydrided are shown in Fig. 5.1. The agreement between the calculated and experimental values is quite remarkable. Based on the same concept, we may calculate the maximum hydrogen concentration in fcc $\mathrm{Zr_xX_{1-x}}$. Based on the fact that the number of tetrahedra per atom is 2 in the fcc phase (see Fig. 2.6), and assuming there is no chemical short range order in the fcc phase (for the purpose of calculation), we find that the number of 4Zr sites per atom in the $\mathrm{Zr_xX_{1-x}}$ is given by $2x^4$. As an example, we compare the numbers of 4Zr terahedral sites in an ordered Cu_3Au phase, a chemically disordered fcc phase and an amorphous phase with composition $\mathrm{Zr_{0.75}Rh_{0.25}}$. The following inequality is obtained:

$$\mathrm{N(amorphous){=}1.58{>}N(disordered\ fcc){=}0.63{>}N(}Cu_3Au\mathrm{){=}0}$$

where N stands for the number of 4Zr tetrahedral sites per atom in each structure of $\mathrm{Zr_{0.75}Rh_{0.25}}$. The number for the amorphous phase is calculated from 5×0.75^4 and that for chemically disordered fcc is from 2×0.75^4. A partially ordered as-quenched fcc solid solution should have N between 0 and 0.63 which is less than what an amorphous phase has. Therefore, a transformation from the fcc phase to the amorphous phase upon hydrogen uptake should be thermodynamically favored. This argument is in agreement with the observation that concentrated coherent fcc hydrides with compositions $\mathrm{Zr_{1-x}Rh_x}$ $(0.15 \leq x \leq 0.25)$ have not been observed in our experiments.

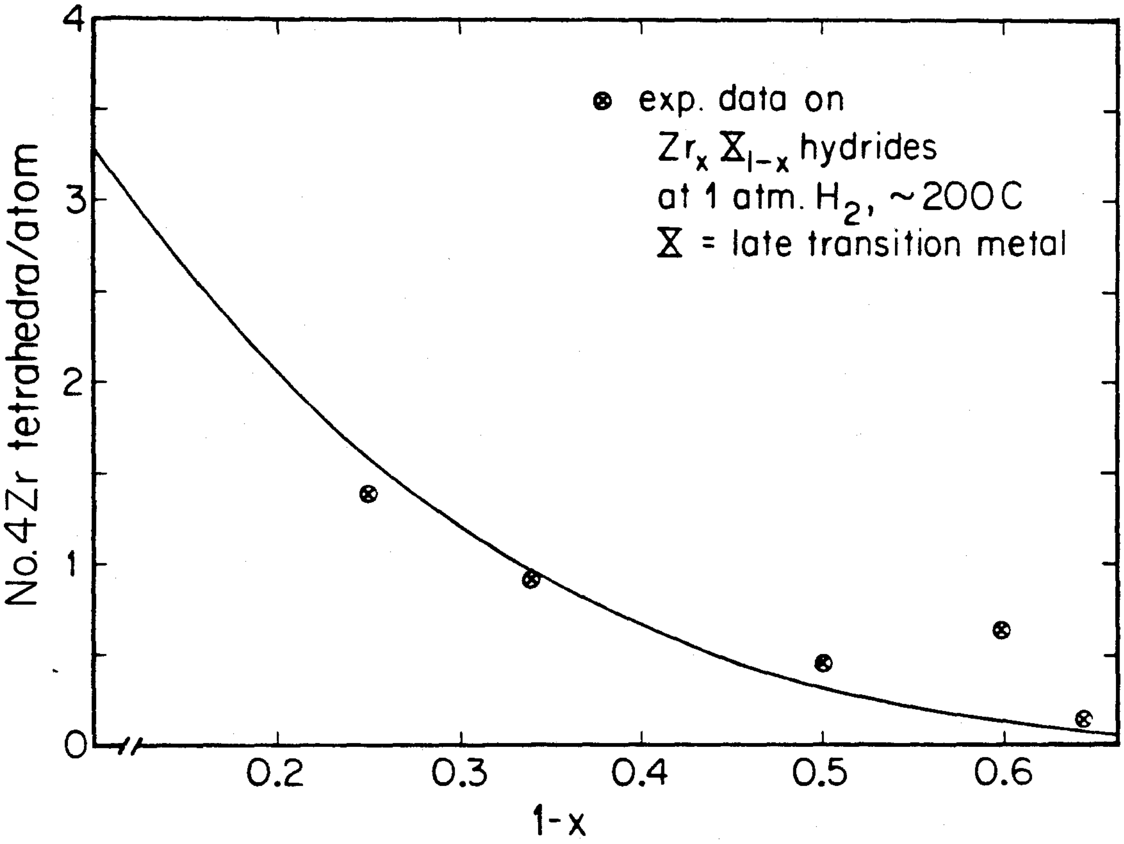

Fig.5.1 Number of 4Zr tetrahedra per atom as a function of Zr concentration x for a topologically close packed structure with 5 tetrahedra per atom. Experimental data are shown for the amount of hydrogen taken at one hydrogen atmosphere ~ 200°C for five different Zr-based glasses: Zr_3Rh, Zr_2Pd, $Zr_{0.40}Cu_{0.60}$, $Zr_{0.36}Ni_{0.64}$ and ZrNi. (Taken from ref. 4.10.)

The free energy relationship of the fcc phase and the amorphous phase at various hydrogen concentrations can best be represented by a free energy- hydrogen concentration diagram shown in Fig. 5.2. This schematic free energy diagram of fcc and amorphous $Zr_{0.80}Rh_{0.20}H_y$ near $180°C$ incorporates the results of X-ray diffraction and thermal analysis. The free energy of the hydrogen free fcc phase is roughly 0.6 kcal/mole lower than that of the corresponding amorphous phase as indicated by thermal analysis (the entropy difference of the fcc and the amorphous phase was not taken into account for simplicity, because the entropy contribution to the free energy is small compared to the enthalpy contribution). As the hydrogen concentration increases, the relative stability of the fcc phase and the amorphous phase gradually reverses, and the amorphous phase becomes more stable than the fcc phase at some critical hydrogen concentration y_o. The fractions of amorphous phase and fcc phase at each hydrogen concentration obtained from X-ray analysis (ref. Fig. 4.10) were used to determine the shape and the relative position of the free energy curves graphically. According to the Lever rule, any point on the common tangent line of the free energy curves of the fcc phase and the amorphous phase must satisfy the condition [5.1]:

$$A_a = \frac{y}{y_a}$$

where A_a is the fraction of amorphous phase in the material, y is the overall hydrogen to metal ratio H/M, and y_a is the H/M at which the common tangent line touches the free energy curve of the amorphous phase. In the present case, y_a is equal to 1. This free energy diagram indicates that even though free energy of the fcc phase becomes higher than that of the amorphous phase beyond a crossover point y_o, the fcc phase can coexist with amorphous phase until y reaches 1. The fcc phase becomes unstable with respect to the amorphous phase as H/M is greater

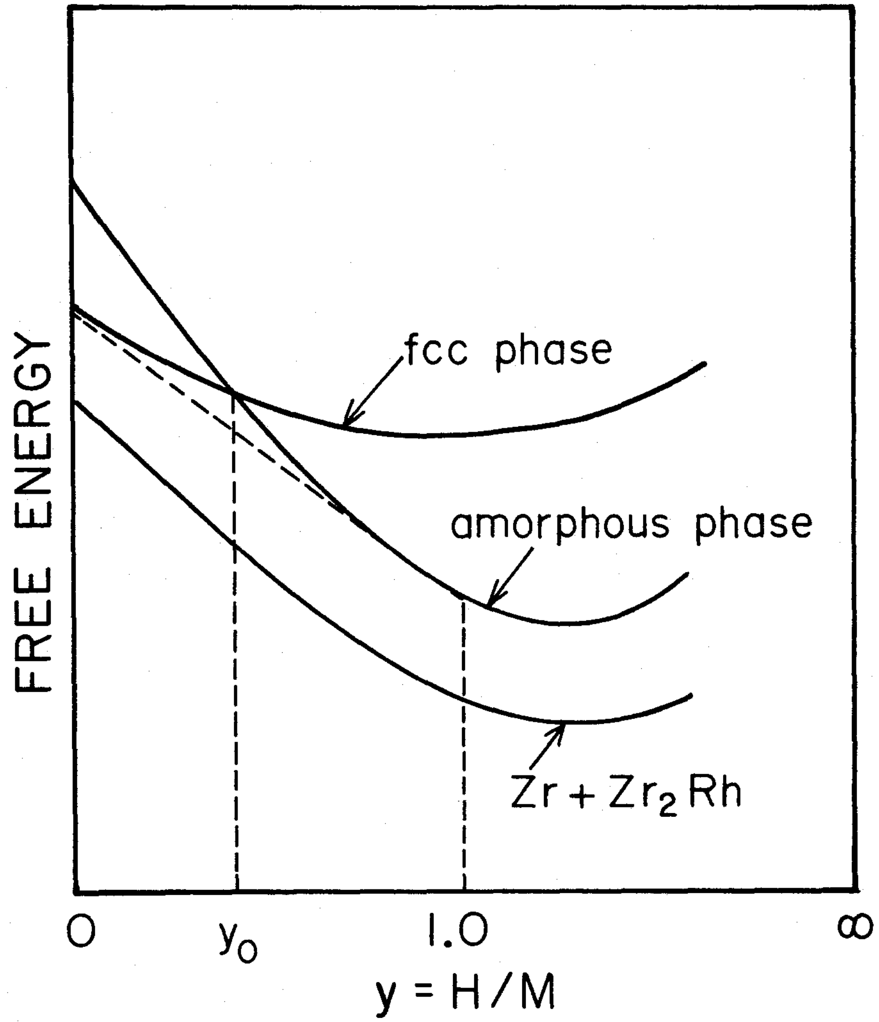

Fig.5.2 A schematic free energy diagram showing the variation of the free enrgy of crystalline $Zr_{0.80}Rh_{0.20}$, amorphous $Zr_{0.80}Rh_{0.20}$, and two phase mixture Zr_2Rh+Zr alloys with hydrogen content.

than 1 and further hydrogen can be accomodated only by the amorphous phase. The equilibrium hydrogen concentration is attained when the chemical potential of the hydrogen in the sample is equal to that of the hydrogen in H_2 gas. Since the ratio of H atoms and H_2 molecules is a constant in the hydrogen gas, the chemical potential of the hydrogen in H_2 gas is actually proportional to the logarithm of the hydrogen pressure.

Computer calculated free energy curves for the fcc and liquid phases of Zr–Rh system at $180°C$ based on the regular solution approximation are shown in Fig. 5.3. The difference in free energy between the fcc and liquid phases decreases with increasing rhodium concentration. This explains why an fcc phase forms more easily in alloys with higher Zr concentration upon rapid quenching.

Fig. 5.2 and Fig. 5.3 are the projections of free energy surfaces onto the temperature–hydrogen concentration and the temperature–alloy composition planes respectively. A qualitative ternary free energy diagram can be constructed by combining the free energy curves in Fig. 5.2 and Fig. 5.3. A portion of such a free energy diagram is shown in Fig. 5.4. The intersection of the free energy surfaces of fcc phase and amorphous phase with ZrH_2 axis is determined based on the fact that the (tetragonally distorted) fcc–ZrH_2 is a thermodynamically stable phase while amorphous–ZrH_2 is unstable and has never been observed in reality. The curvature of the free energy surfaces $\partial^2G/\partial C^2 > 0$ (where C is the composition variable) ensures that every points on the free energy surface satisfy the Gibbs criterion for each phase to be at least metastable against a spinnodal decomposition [5.2].

Note that the free energy surfaces of the fcc and amorphous phases intersect on a three dimensional curve which represents polymorphic melting at the given

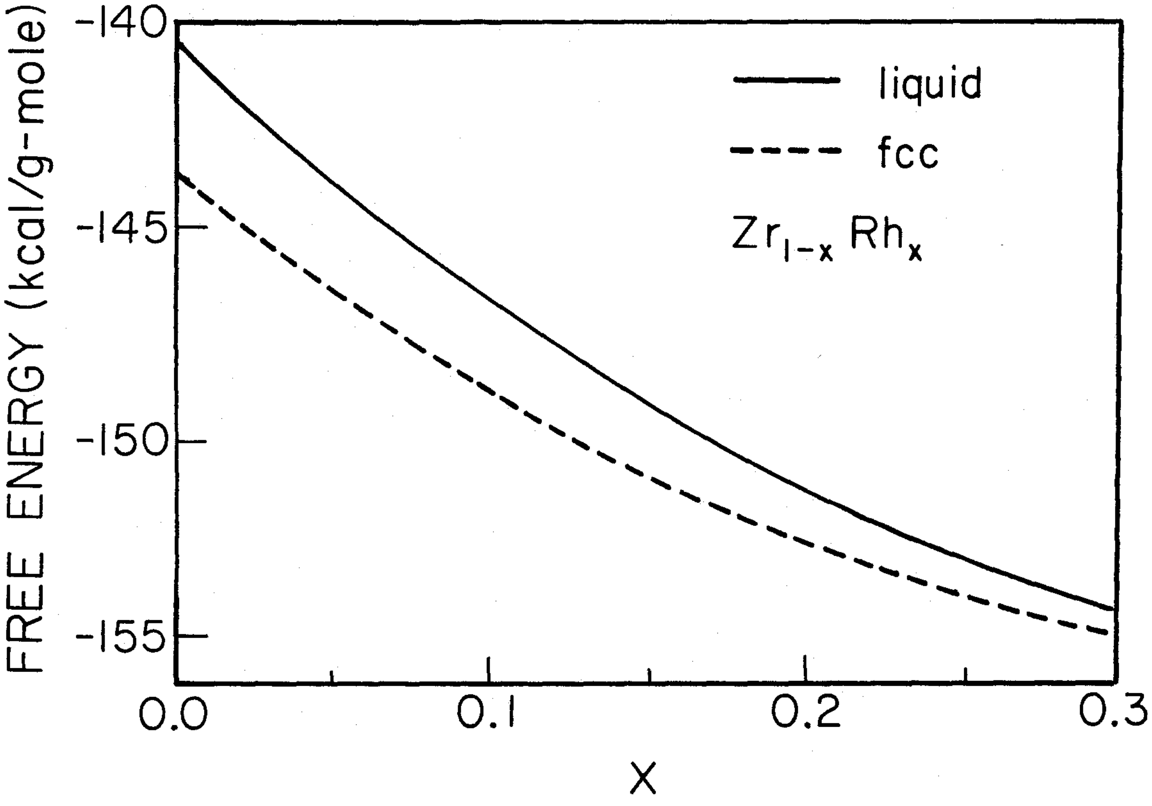

Fig.5.3 Computer calculated free energy curves of liquid and metastable fcc of Zr–Rh system.

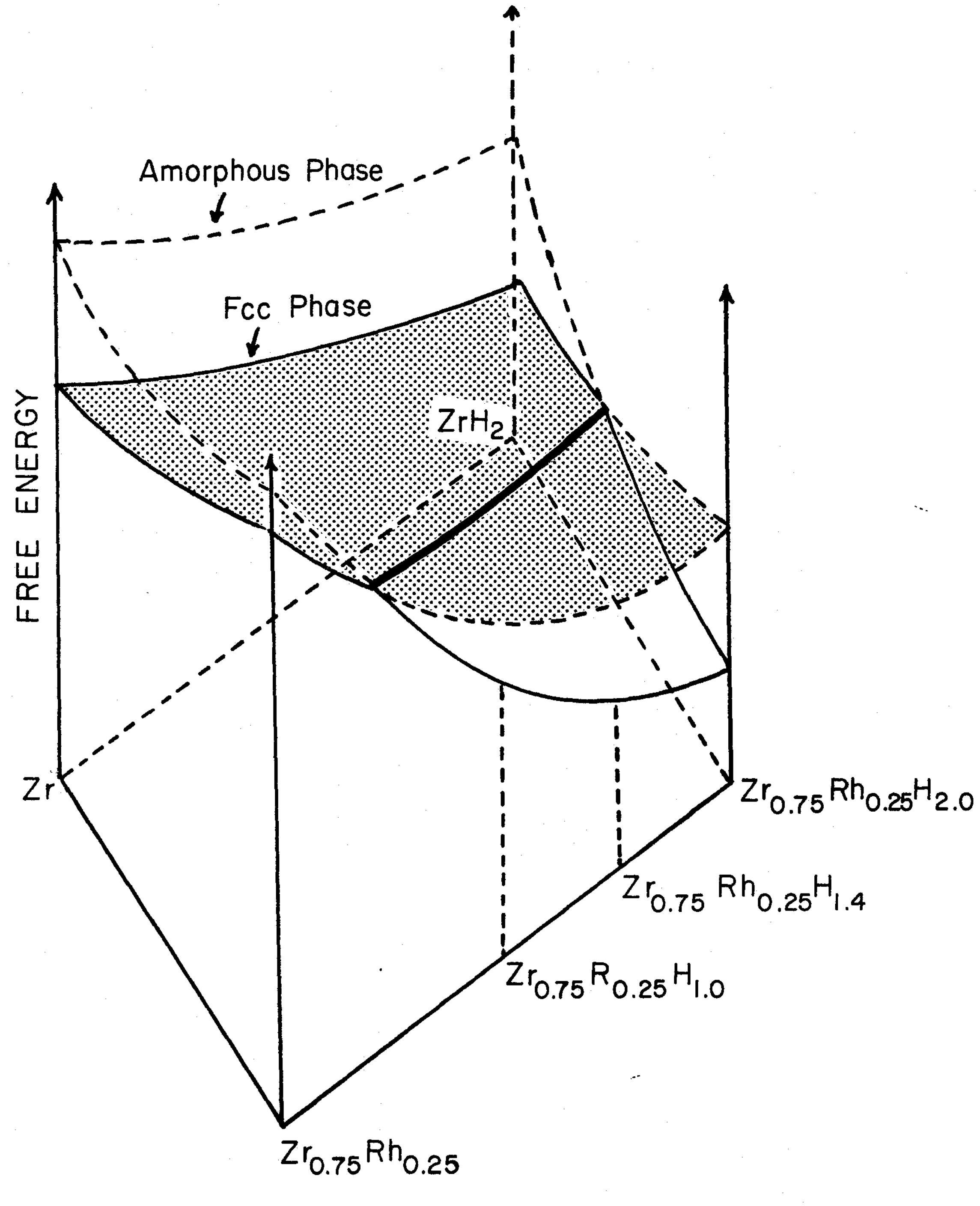

Fig.5.4 A schematic free energy surfaces of liquid (unshaded) and fcc (shaded) phases for the ternary Zr–Rh–H system at ~ 180°*C*. The thick line represents the composition at which the free energies of liquid and fcc phases are equal. The solid curves represent the thermodynamically stable phases.

temperature (180°C in present case) as a function of composition. In analogy to the definition of the T_o curve, we shall call it a C_o curve. In fact, T_o is the projection of the polymorphic melting surface onto the temperature–composition plane, and the C_o curve is the projection of that surface onto the free energy–composition space. This C_o curve separates the composition region where the amorphous phase has lower free energy from the region where fcc phase has lower free energy. It is obvious from this figure that a higher hydrogen concentration is required to amorphize an fcc solution with higher Zr concentration than one with lower Zr concentration. This explains why we can only partially amorphize the $Zr_{0.85}Rh_{0.15}$ sample by hydriding at one atmosphere of H_2 gas. It is, however, expected that this alloy could be completely amorphized if one could perform the hydriding experiment at very high pressure (>100 atm.).

§5.2 KINETIC ASPECTS

Throughout the discussion in the last section, we have tacitly assumed that only a polymorphic (without composition change or phase separation) transformation of the metal alloys can take place. One must inquire as to why formation of Zr_2RhH_y+ ZrH_2 does not occur upon hydriding. Such a product phase is definitely more stable than the amorphous phase. In order to emphasize this point, we have drawn the schematic free energy diagram of Zr–Rh system before and after hydriding once more on Fig. 5.5, but with the free energies of the equilibrium phases included. It is clear from Fig. 5.5a that the phase mixture of Zr_2Rh+Zr is the equilibrium state; however it does not form during rapid quenching due to the fact that the characteristic time for metal compositional segregation is much longer than the cooling time. It is also true (see Fig. 5.5b) that Zr_2RhH_y + ZrH_2 is more stable

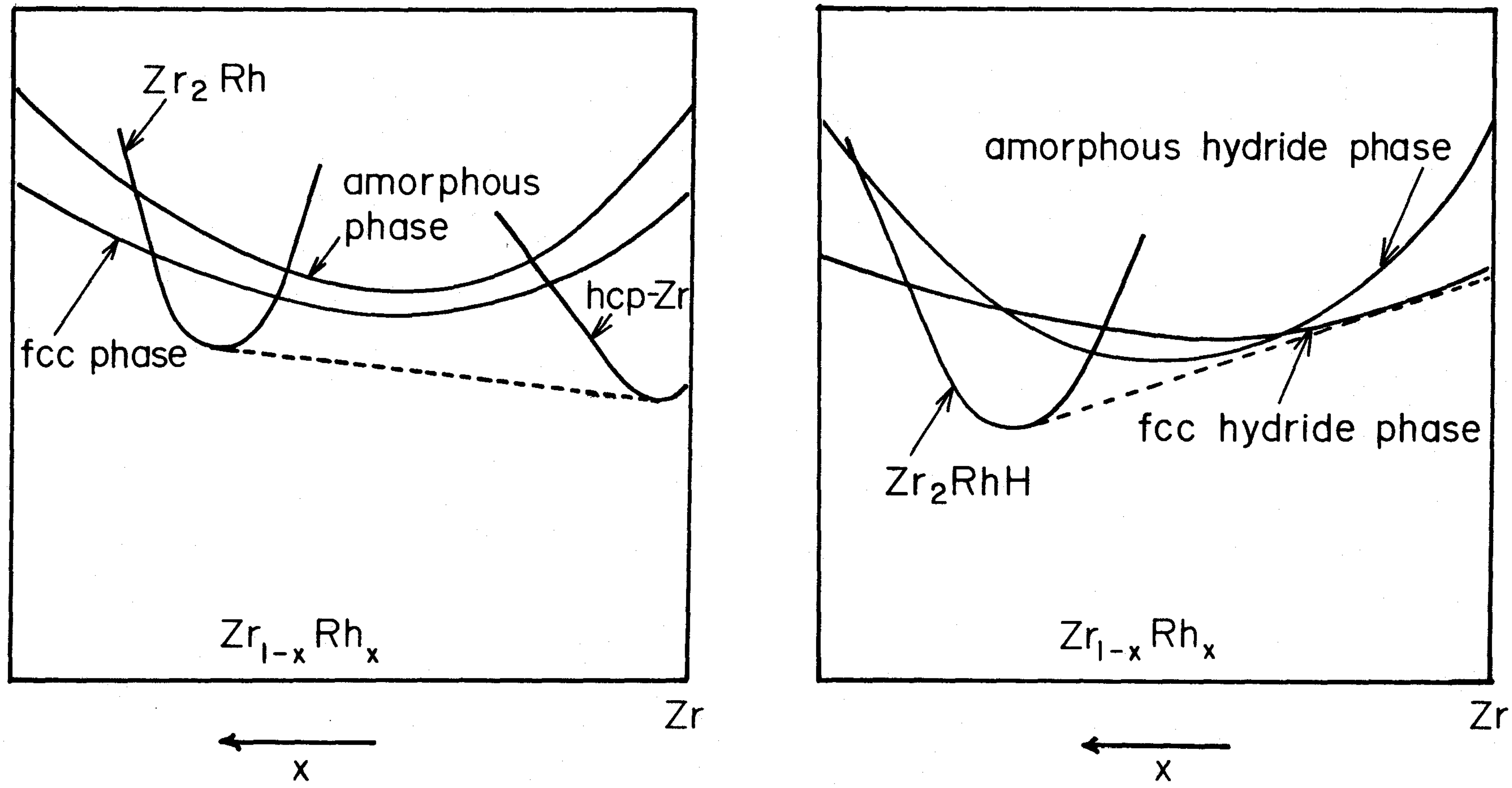

Fig.5.5 Hypothetical free energy diagram for $Zr_{1-x}Rh_x$ and $Zr_{1-x}Rh_xH_y$.

than the amorphous hydride phase (the common tangent line of the free energy of these phases lies below that of the amorphous hydride phase). Then why doesn't $Zr_2RhH_y + ZrH_2$ form during hydriding at temperatures below $230°C$?

A simple steady-state reaction model allows one to understand this phenomenon [5.3]. Let's suppose that the hydriding reaction of single phase fcc $Zr_{1-x}Rh_x$ is taking place at relatively high temperatures ($\geq 230°C$, say) such that both hydrogen and metal atoms have enough mobility to move over appreciable distances. Then there are two reactions which will occur simultaneously: the hydrogen absorption by the fcc phase and the phase separation of the fcc hydride into a two phase mixture ($ZrH_y + Zr_2RhH_z$) as verified by the experiment. As illustrated in Fig. 5.6, the planar reaction front (A) moves at a velocity v to form $ZrH_2 + Zr_2RhH_y$ from the single phase fcc $Zr_{1-x}Rh_x$ during hydrogen absorption. J_{Rh-Zr} and J_H denotes the flux of metal and hydrogen atoms respectively. And (B) represents the hydrogen gas–solid interface.

At first the dissolution of H into fcc $Zr_{1-x}Rh_x$ occurs at the gas-solid boundary (B) to form dilute $Zr_{1-x}Rh_xH_y$ ($y << 1$). The fact that a small amount of hydrogen is absorbed by the fcc phase before any phase transformation takes place has been confirmed experimentally by the small change in the lattice parameter of the fcc phase observed by X- ray diffraction during the reaction. A two-phase product forms at a second interface (A) with characteristic domain sizes d_1 (c-ZrH_y) and d_2 (c-Zr_2RhH_z). As pointed out by the classical nucleation and growth theory, the reduction of interfacial energy $\sigma_{1,2}$ requires that (d_1 and d_2) exceed a critical value d_{min}, where d_{min} is the larger of the critical thicknesses of ZrH_y and Zr_2RhH_z layers. Thus Rh must move a characteristic distance at least d_{min} in order to

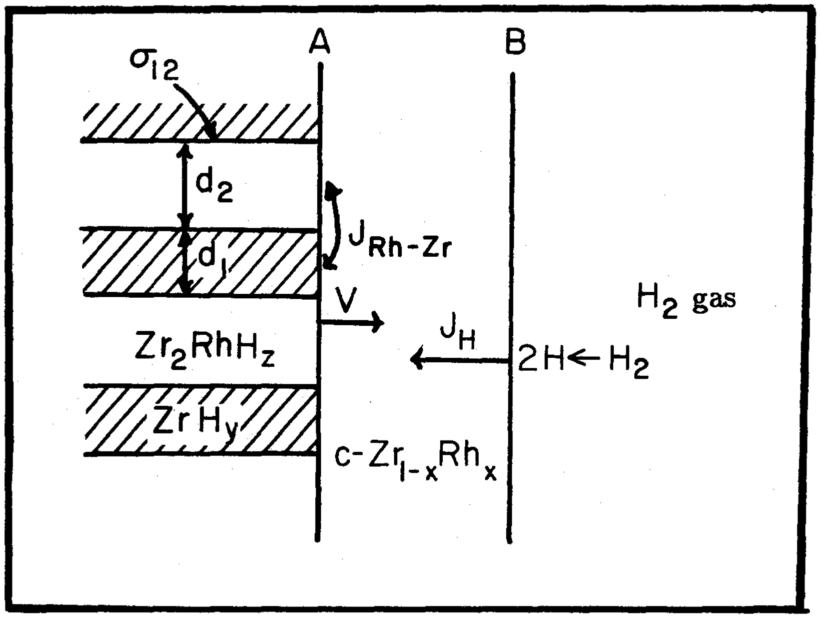

Fig.5.6 Schematic illustration of steady-state reaction front (A) moving at velocity V to form c-ZrH_2+Zr_2RhH_y from fcc-$Zr_{0.80}Rh_{0.20}$ containing dilute hydrogen in solution. τ_H and τ_{Zr-Rh} represent diffusion fluxes. B is the boundary with the hydrogen gas.

form the two-phase mixture, assuming Rh is the species that diffuses out of the $Zr_{1-x}Rh_xH_y$ matrix. (This is likely, since late transition metal atoms have been found to be fast diffusion species in early transition metal-late transition metal alloys [5.2, 5.4].) A time scale of order $\tau_1 = d_{min}^2/D$ is required for interdiffusion of Zr and Rh in the direction parallel to the interface where D is the *interdiffusion constant* of Zr and Rh in fcc-$Zr_{1-x}Rh_xH_y$. One can take $D \sim D_o e^{-Q/k_BT}$, where Q is the activation energy for this process. A second time scale $\tau_2 = L^2/D_H$ where L is a typical sample dimension ($\sim 40\mu m$) and D_H is the diffusion constant for hydrogen in fcc-$Zr_{1-x}Rh_x$, characterizes the time required to transport hydrogen from A to B. One can take $D \sim D_H^o e^{-Q'/K_BT}$. NMR studies have shown that $Q' \sim 0.5eV$ while alloy diffusion studies would suggest $Q \sim 1.5 - 2.0eV$ [5.5]. The formation of the two-phase mixture requires the long range diffusion of hydrogen atoms as well as metal atoms, whereas a polymorphic transformation to the amorphous hydride requires only the diffusion of hydrogen. It is clear that the ratio (τ_1/τ_2) varies rapidly with temperature. At low T, the phase separation into phases of differing metal concentrations is rate limited by τ_1. The amorphization reaction (which does not require a long range metal diffusion), in contrast, is rate limited by only τ_2. For sufficiently low T, we have:

$$\tau_1 >> \tau_{reaction} >> \tau_2$$

where $\tau_{reaction}$ is the required time scale of the overall reaction. Thus, the phase separation reaction is "chemically frustrated" and only the amorphization reaction can proceed during hydriding on practical time scale at such low temperatures.

We can estimate the lowest temperature at which the metal compositional segregation can proceed on a realistic time scale. Let us assume the size of the critical nuclei of ZrH_2 to be d_{min}=20Å (which is about five times the length of the unit cell of ZrH_2), and a reasonable reaction time scale to be $\tau_{reaction}$=50 hours. The minimum r.m.s distance that the Rh atoms must diffuse in order to form stable ZrH_2 nuclei is given by $d_{min} = (2D\tau_{reaction})^{1/2}$. Therefore,

$$D = \frac{(20 \times 10^{-10})^2}{2 \times 50 \times 3600}(m^2/sec) \sim 10^{-23}(m^2/sec)$$

is the minimum required Rh diffusion constant to have metal segregation during the reaction time. Lacking Rh diffusion data in Zr-Rh alloys, we compare this number with that of Pt (Pt is very similar to Rh) in Zr_2Ni given by Cantor and Cahn [5.5]. We find that this number matches the Pt diffusion constant at a temperature of ~ 250°C. Thus, the amorphization reaction should occur if the hydriding temperature is below 250°C. This estimate gives good agreement with our experiments which show that the amorphization reaction occurs if the hydriding temperature is below 230°C.

The above situation is formally similar to suppression of crystallization which occurs by solute partitioning during rapid quenching from the liquid state. The role played by the hydrogen diffusion (D_H) is formally analogous to the role played by heat flow, J_Q, driven by a temperature gradient ∇T in rapid quenching. For large $J_Q(\nabla T)$, partitioning reactions become diffusion limited [5.6]. Solute trapping results and glass is formed in the absence of an alternative polymorphic crystallization reaction. The reader should be aware that although long range diffusion of metal atoms is suppressed during a solid state amorphization hydriding reaction, a local rearrangement of metal atoms is nevertheless required for the amorphization.

VI. CONCLUSIONS

Amorphous phase formation during hydriding has been observed in several as-quenched polycrystalline fcc phases of early transition metal–late transition metal alloys. All of the experimental evidence indicates that the properties of amorphous hydrides obtained through a solid state amorphization reaction are identical to those obtained by hydriding initially amorphous alloys of the same composition. This solid state amorphization upon hydriding can be described as a "solid state melting" process. The amorphous phase grows beginning at crystalline grain boundaries, and proceeds by advancing the amorphous front into the interior of cystalline grains.

The amorphous phase in the Zr–based alloys has more 4Zr tetrahedral interstitial sites than the corresponding fcc phase of the same composition. Therefore the amorphous hydride has a lower free energy than the fcc hydride. This free energy difference is the driving force of the amorphization reaction. The formation of the equilibrium phase mixture is kinetically forbidden, because the long range diffusion of metal atoms is suppressed when the reaction is carried at sufficiently low temperatures.

This effect suggests that amorphous phases can be formed by using a completely different kinetic approach than those used in conventional rapid quenching techniques. The solid state amorphization does not require one of the sample dimensions to be small as does the rapid quenching techniques, and therefore it is a potentially useful technique for producing bulk amorphous alloys.

REFERENCES

Chapter One

1.1. W. Klement, R.H. Willens, P. Duwez, Nature, **187**, 869 (1960).

1.2. J.J. Gilman, Phys. Today, 46 (May, 1975).

1.3. P. Duwez, *Prog. in Solid. State Chem.* (Pergaman, Oxford, 1966), **Vol. 3**, p.377.

1.4. W. Buckel and R. Hilsch, Z. Physik, **138**, 109 (1954).

1.5. F. Spaepen and D. Turnbull, *Rapidly Quenched Met.* II, (MIT, Cambridge, 1975), **Vol. 1**, p.205.

1.6. H.B. Callen, *Thermodynamics*, (John Wiley, New York, 1960).

1.7. M.F. Thorpe, J. Non-Cryst. Sol., 5,365 (1983).

1.8. M.F. Thorpe, Proc. New York Acad. Sci. Sym. on *Dynamic Processes in Glasse*, eds. C. -A Angele and M. Goldstein, (New York Acad. Sci., New York, 1985) in press.

1.9. T. Egami and Y. Waseda, J. Non-Cryst. Sol., **64**, 113 (1984).

1.10. W.L. Johnson, Prog. in Mat. Sci., (1986) in press.

1.11. J. Bloch, J. Nucl. Mat. **6**, 203 (1962).

1.12. K.C. Russell, Prog. Mat. Sci., **28**, 229 (1965).

1.13. X.L. Yeh, K. Samwer and W.L. Johnson, Appl. Phys. Lett. **42** (3), 242 (1983).

1.14. R.B. Schwarz and W.L. Johnson, Phys. Rev. Lett. **51**, 415 (1983).

1.15. R.B Schwarz, R.R Petrich and C.K. Saw, J. Non–Cryst. Sol., **76**, 281 (1985).

1.16. M. Atzmon, K.M. Unruh and W.L. Johnson, J. Appl. Phys., (1985).

Chapter Two

2.1. D. Turnbull, Contemp. Phys., **vol. 5**, **No. 5**, 473 (1969) and Metall. Trans.

vol. **12A**, 695 (1981).

2.2. H. Biloni, in *Physical Metallurgy*, **3rd edition**, eds. R.W. Cahn and P. Haasen, (North Holland, 1983), p.478.

2.3. P. Haasen, *Physical Metallurgy*, (Cambridge University Press, 1978), p.218.

2.4. W.L. Johnson, Prog. in Mat. Sci., (1986) in press.

2.5 J. Dages, H. Gleiter, and J. Perepesco, Proc. MRS Sym on Phse Transitions in Condensed Systems, (Boston, 1985), (MRS, Pittsburg, 1986) in press.

2.6. A.R. Williams, Ph.D. Thesis, Caltech, (Pasadena, 1981).

2.7. G.S. Cargill, in *Solid State Physics*, **vol. 30**, eds. H. Ehrenreich, F. Seitz and D. Turnbull, (Academic Press, 1975).

2.8. J.D. Bernal, Nature **185**, 68 (1960).

2.9. D. Turnbull and D. Cohen, J. Chem. Phys. **52**, 3038 (1970).

2.10. K.H.J. Buschow, P.C.P. Bouten and A.R. Miedema, Report on Prog. in Phys. **vol. 45, No. 9**, 937 (1982).

2.11. A.R. Miedema, K.H.J. Buschow and H.H. van Mal, J. Less-Common Met. **49**, 463 (1976).

2.12. A.C. Switendick, in *Hydrogen in Metals* I, eds. G. Alefeld and J. Volkl, (Springer-Verlag, Berlin, 1978), p. 283.

2.13. C.D. Gelatt, H. Ehrenreich and J.A. Weiss, Phys. Rev. **B17, No. 4**, 14 (1967).

2.14. K. Suzuki, N. Hayashi, Y. Tomizuka, T. Fukunaga, K. Kai and N. Watanabe, J. Non-Cryst. Solids **61 & 62**, 637 (1983).

2.15. A.R. Williams, J.Eckert, X.L. Yeh, M. Atzmon and K. Samwer, ibid., p. 643.

2.16. V.A. Somenkov and S.S. Shil'stein, Prog. in Mat. Sci. **vol. 24**, 267 (1980).

2.17. Y. Fukai, J. Less-common Met. **vol. 101**, 1 (1984).

2.18. K. Samwer and W.L. Johnson, Phys. Rev. **B28**,2907 (1983).

2.19. R.C. Bowman, Ph.D thesis, Caltech, Pasadena, 1983.

2.20. M. Tenhover, Private Communications, 1984.

2.21. E. Wicke and H. Brodowsky, in *Hydrogen in Metals* II, eds. G. Alefeld and J. Volkl, (Springer-Verlag, Berlin, 1978), p.73.

2.22. H. Wagner, in ref. 2.12, p.5.

2.23. R.C. Bowman, Jr. , E.L. Venturini, B.D. Craft, A. Attala and D.B. Sallenger, Phys. Rev. **B27**, 1474 (1983).

Chapter Three

3.1. P. Pietrokowsky, Rev. Sci. Instrum. **34**, 445 (1963).

3.2. H.S. Chen and C.E. Miller, Mat. Res. Bull. **11**, 49 (1976).

3.3. J.L. McNaughton and C.T. Mortimer, in IRS; Physical chemistry Series **2, vol. 10**, (Butterworths, London, 1975).

3.4. D.A. Leich and T.A. Tombrello, Nucl. Inst. and Meth. **108**, 67 (1973).

3.5. R.W. Cahn in *Physical Metallurgy*, **3rd edition**, eds., R.W. Cahn and P.A. Haasen, (North Holland, 1983), p. 1781.

Chapter Four

4.1. The results in section have been published in ref. 1.13 and in X.L.Yeh, W.L.Johnson, J.Y.Tang and C.R.Shi, Proc. MRS Sym on Rapidly Solidified Alloys, eds. A.Tauy, et al, (MRS', Boston, 1985) in press.

4.2. M. Atzmon and W.L. Johnson, J. Non-Cryst. Solids **55**, 395 (1983).

4.3. R.W. Cahn, in ref.3.5, p. 1780.

4.4. L. Kaufman, and H. Bernstein, *Computer Calculation of Phase Diagrams*, (Academic Press, 1970).

4.5. T.B. Massalski, in Proc. 5th Int. Cof. on Rapidly Quenched Metals, eds. S.

Steeb and H. Warlimont, (North Holland, Amsterdam, 1985). p. 171.

4.6. P. Haasen, *Physical Metallurgy*, (Cambridge University Press, 1978), p.61.

4.7. D.R. Gaskell, in ref.3.5, p. 272.

4.8. M. Hansen, *Constitution of Binary Alloys*, (McGraw-Hill, New York, 1958), p.808.

4.9. K. Suzuki, N. Hayashi, Y. Tomizuka, T. Fukunaga, K. Kai and N. Watanabe, J. Non-Cryst. Solids **61 & 62**, 637 (1983).

4.10. K. Samwer and W.L. Johnson, Phys.Rev. **b28**, 2907 (1983).

4.11. K. Samwer, in NATO ASI on Amorphous Hydrides, (Rhodes, Gveece, 1985) in press.

4.12. A. Guinier, *X-ray Diffraction.* (Freeman, San Francisco, 1963), chap. 5.

4.13. R.W. Cahn and W.L. Johnson, to be published in J. of Mat. Res., **1**, 1986.

4.14. J.A. Horton, A. Dasyupta and C.T. Liu, in *High Temperature Ordered Intermetallic Alloys*, eds. C.T. Liu and N.S. Stoloff (Mat. Res. Soc. Symp. Proc., vol. 39, 1985), p. 109.

4.15. K.C. Russell, in-Proc. Int. Seminar on Solute-Defect Interaction, Kingston, Ontario, (Pergamon Press, Oxford, 1985) in press.

4.16. The results in this section will be published in X.L. Yeh, E.J. Cotts and W.L. Johnson, J. Mat. Res., 1986.

4.17. J.E. Wagner, R.C. Bowman, Jr. and J.S. Cantrell, J. Appl. Phys. (1985).

4.18. L. Schlapbach, A. Seiler, F. Stucki and H.C. Siegmann, J. Less- comm. Met., **73**, 145 (1980).

4.19. A.R. Williams, J. Eckert, X.L. Yeh, M. Atzmon and K. Samwer, J. Non-Cryst. Sol., **61 & 62**, 643 (1983).

4.20 K.H.J. Buschow, P.C.P. Bouten and A.R. Miedema, Report on Prog. in Phys., **vol. 45, No. 9**, 937 (1982).

4.21. The results in this section will be published in X.L. Yeh, Z.Y. Zhou, C.R. Shi, Y.T. Cheng, W.L. Johnson, T. Tombrello, and M.A. Nicolet, J. Appl. Phys., 1986.

4.22. F.H.M. Spit, J.W. Drijver, W.C. Turkenburg and S. Radelaar, in *Metal Hydrides*, ed. G. Bambakidis, (Plemum, N.Y., 1981), p. 345.

4.23. J.T. Yates, P.A. Thiel and W.H. Weinberg, Surf. Sci., **84**, 427 (1979).

4.24. R.J. Madix, G. Ertl and K. Christmann, Chem. Phys. Lett., **62**, 38 (1979).

5.25 J.J. Hren, J.I. Goldstein and D.C. Joy, *Introduction to Analytical Electron Microscopy*, (Plenem Press, New York, 1979), p. 141.

Chapter Five

5.1. A.G. Guy, *Essentials of Materials Science*, (McGraw-Hill, New York, 1976), chap.2.

5.2. W.L. Johnson, Prog. in Mat. Sci., (1986) in press.

5.3. W.L. Johnson, M. Atzmon, M. Van Rossum, B.P. Dolgin and X.L. Yeh, in *Rapidly Quenched Metals*, eds. S. Steeb and H. Warlimont, (North Holland, 1985), p. 1515.

5.4 W.L. Johnson, B. Dolgin and M. Van Rossum, in *Glass- Current Issues*, eds. A.F. Wright and J. Dupay, Nata ASI series, E-92 (Martinus Nijhoff, Boston, 1985), p.172.

5.5 B. Cantor and R.W. Cahn, in *Amorphous Metallic Alloys*, ed. F.E. Luborsky, (Butterworths, London, 1983), p.487.

5.6. M.J. Aziz, J. Appl. Phys., 53, 1158 (1982).